Kinetic Modeling of Heterogeneous Chemical Reactions with Applications to the Reduction of Environmental Contaminants on Iron Metal

Joel Zachary Bandstra
B.S., Clarkson University, 1998

A dissertation presented to the faculty of the
OGI School of Science & Engineering
at Oregon Health & Science University
in partial fulfillment of the
requirements for the degree
Doctor of Philosophy
in
Environmental and Biomolecular Systems

May 2005

This dissertation "Kinetic Modeling of Heterogeneous Chemical Kinetics with Applications to the Reduction of Environmental Contaminants on Iron Metal" by Joel Z. Bandstra has been examined and approved by the following Examination Committee:

Paul G. Tratnyek, Dissertation Advisor
Professor

Antonio M. Baptista
Professor

Richard L. Johnson
Professor

Reuben H. Simoyi
Professor, Portland State University

ACKNOWLEDGMENTS

I am grateful for the guidance and instruction that I have received from my advisor, Dr. Paul Tratnyek. My co-workers in the Tratnyek lab have also made a substantial footprint on the work that appears in this dissertation; to Dr. Rosemarie Miehr, Dr. James Nurmi, Mr. Clinton Church, Mrs. Thea Reilkoff, Mrs. Rachel Waldemer, Mrs. Vaishnavi Sarathy, and Dr. Bumhan Bae, I am surely indebted. My dissertation committee members have been of great service to me. I extend sincere thanks to Drs. Antonio Baptista, Richard Johnson, and Rueben Simoyi for providing the offense at my dissertation defense.

A number of teachers have made substantial impacts on my academic and personal development. These include Mr. Niles Hershberger, my high school Mathematics teacher, whose patient admonishment has remained in my mind; Mrs. Alice Furda, my high school English teacher, whose lovely encouragement still warms my heart; Dr. Luke Gascho, my high school principal, whose exemplar character has been imprinted upon my soul; Miss Linda Gundlach and Mrs. Kathy Keafer, my instructors in the Discovery Center, who taught me how to manage my many significant intellectual shortcomings; Dr. Gregory Dick and Mr. Gary Johnson, who taught me how to play hard, a lesson that flowed from the river into my school work; Dr. Scott Fulton, whose Freshman Calculus class changed my approach to learning and whose Complex Analysis class opened my eyes to the beauty of higher mathematics; and Dr. Thomas Theis, whose Environmental Chemistry class moved me so, that I chose to pursue a Ph.D. in the topic.

There exists a great cloud of witnesses and they have surrounded me with love during these student days. This cloud cheers me on and I hear them full well. The names need not be listed here, for such a list would be fleeting, but this work would certainly not be what it is, had it not been for them.

DEDICATION

Now unto the King eternal, immortal, invisible, the only true God,

be honour and glory for ever and ever. Amen.

TABLE OF CONTENTS

LIST OF TABLES

LIST OF FIGURES

ABSTRACT

Kinetic Modeling of Heterogeneous Chemical Reactions with Applications to the Reduction of Environmental Contaminants on Iron Metal
Joel Zachary Bandstra, B.S.

Ph.D., OGI School of Science & Engineering
at Oregon Health & Science University

February 2005
Dissertation Advisor: Dr. Paul G. Tratnyek

In the past decade, permeable reactive barriers containing zero-valent iron metal (FePRBs) have emerged as the most significant new technology for the treatment of groundwaters contaminated with chlorinated organic compounds and, more recently, other organic contaminants such as 2,4,6-trinitrotoluene (TNT). Principle issues relating to the design, implementation, and monitoring of FePRBs include the rates of contaminant transformation, the resulting distribution of products, and the potential changes in FePRB performance due to aging of the iron material. Each of these issues is, at its root, a problem of chemical kinetics. In this thesis, commonly observed kinetic expressions for contaminant transformation are derived. Analyses of the simplifications involved in these derivations indicate that the forms of the rate laws are correct (either exactly or approximately) over a wider range of conditions than previously expected and that reaction rates may respond in unexpected fashion to changes in concentrations of reacting species or iron loading. These theoretical developments are applied to experimental investigations of product distribution and FePRB longevity for the treatment of TNT contaminated groundwaters.

CHAPTER 1

Overview

1.1 Introduction and Problem Statement

In the past decade, permeable reactive barriers containing zero-valent iron metal (FePRBs) have emerged as the most significant new technology for the treatment of groundwaters contaminated with chlorinated organic compounds and, more recently, other organic contaminants such as 2,4,6-trinitrotoluene (TNT) [1,2]. Since the strategy of using iron to treat chlorinated solvents was first articulated [3], researchers from a wide variety of academic disciplines have investigated aspects of this technology, including reaction pathways, degradation products, chemical mechanisms, chemical kinetics, and mass transport. Some significant results include (i) the surface area normalization of observed degradation rate constants [4] and the application of kinetic models accounting for sorption and site limitation [5-7], (ii) the correlation of reduction rates to the lowest unoccupied molecular orbital energy (E_{LUMO}) of the contaminant [8], (iii) the identification of intermediate species and end products for a host of initial contaminants, and (iv) the recognition of the role of oxide films in controlling the reduction process [9].

A common theme in all of these research efforts is the kinetics of the iron mediated reduction reactions. Kinetic information for a given contaminant is key to designing FePRBs. These kinetic studies also form a principle means of determining reaction mechanisms and the distribution of reaction products. Many of the kinetic studies with the iron metal system have focused on defining empirical rate equations with batch and column disappearance data. In contrast to these macroscopic studies, recent molecular modeling efforts have focused on reaction kinetics at the atomistic scale.

Integration of these two bodies of work, however, is limited by the significant theoretical gulf that lies between these two scales (see figure 1). A comprehensive theory of scaling has been a long-term goal in theoretical chemical kinetics. In addition to possessing scientific impact, such a construct would be useful in the ongoing research and development of iron metal remediation technologies. This thesis is focused on a piece of the scaling problem that, to date, has received little attention—scaling between mechanistic chemical kinetics, where all stable reactants, products, and intermediates in a reaction are specifically treated, and empirical chemical kinetics, where the number of species considered explicitly is minimized to only those that are important.

1.2 Theory of Chemical Kinetics

The word "kinetic" is derived from the greek word "kinetikos" meaning to move. In physics, the study of motion (mechanics) is divided into kinematics, which deals with the description of motion, and kinetics, which deals with the effects of forces on motion. In chemistry, such a distinction is not made and chemical kinetics refers to the study of the time rate of change of the chemical composition of materials. The chemical composition of a material can be described, macroscopically, in terms of thermodynamic state variables such as temperature, pressure, or chemical potential, but, the most common macroscopic descriptor is chemical concentration (which is related to chemical potential) because, as we will see, reaction rates usually depend directly on the population of reacting species.

From a molecular viewpoint, chemical kinetics involves the study of chemical reactions in which one or more molecules undergo a transformation to form a new molecule or molecules. Of course, at thermodynamic equilibrium, the macroscopic state variables listed above remain unchanged but molecular transformations still occur and the equilibrium values of the state variables are defined by the kinetics of those transformations. The amount of time required for a single molecular transformation is typically on the order of a femto-second while changes in the properties of materials are usually on a much longer time scale (e.g., microseconds for the combustion of explosives to kilo-years for mineral weathering). The kinetics of a chemical reaction are, therefore, determined by the number of molecular transformations that occur per unit time and

chemical kinetics can be thought of as a Markov chain [10-12] with the transition probabilities determined by the mechanics of the underlying molecular transformations.

Theoretical methods for predicting the probabilities of a molecular transformation are based on the conclusion—originally drawn by Arrhenius [13]—that a chemical reaction involves passing over an energy barrier between two (local) minimum energy molecular configurations. The initial energy minimum corresponds to the reactant(s) and the final energy minimum corresponds to the product(s) of the reaction. Additional energy minima may exist between the reactants and products and these minima correspond to stable reaction intermediates.

Calculating the energy for any molecular configuration involves the evaluation of the quantum mechanical Hamiltonian for the bond angles, inter-atomic distances, and electronic configuration that are particular to the given configuration. Predicting a molecular transformation probability, then, involves energy calculations for a range of molecular configurations leading to an energy hyper-surface generally referred to as a potential energy surface [14]. Since the reaction can follow any path across the potential energy surface, even discontinuous paths involving quantum tunneling, many schemes for evaluating chemical kinetics from first-principles simplify the hyper-surface to a one-dimensional energy curve that follows the minimum energy path between reactants and products. This minimum energy path is referred to as the reaction coordinate and reaction coordinate following is the simplification employed transition-state theory [15] and Marcus theory [16,17].

Chemical reactions are often times conceptualized in terms of the reaction mechanism where all important molecular transformations are represented as the molecular species involved in the transformation connected by an arrow which signifies the transformation. The kinetics of the chemical reaction may be specified by determining an equation for the rate of each of the transformations in the reaction mechanism. The equations are known as the rate laws and are usually formed from the product of a constant (known as the rate constant) and the concentrations of the reacting species raised to an integer power which is equal to the molecularity of the given species. The reaction mechanism can be related to the potential energy surface by considering a graph whose nodes represent the local minima in the potential energy surface (i.e., the

reactants, intermediates, and products) and whose edges are then drawn between any two nodes that are connected by a segment of the reaction coordinate that passes through no other potential energy surface minima. The rate laws for the reaction mechanism are, thus, directly related to the transformation probabilities between connected nodes on the graph.

The kinetics of a reaction depend, in principle, on the concentrations of all reactants, intermediates, and products. For many reactions, however, the rate is found to depend primarily on the concentrations of only a few of the stable species (e.g., the reactants). Rate laws that account only for the important species can, therefore, be empirically defined to capture the critical features of laboratory kinetics experiments. Since empirical rate laws need not be constrained by the principles of Markovian dynamics, they may take forms other than the product of concentration terms that apply to mechanistic rate laws. Such products are, however, still found to be broadly applicable with the allowance of non-integer powers on the concentrations [18]. Other common forms for empirical rate laws include the quotient of two finite series of concentration terms [19] and exponential rate equations derived from spectral integration.

1.3 Scaling Chemical Kinetics

Figure 1 shows the theoretical constructs described above organized according to the length scales at which each is most relevant. Quantum mechanics details the structures of the reacting species and, therefore, defines the most basic theory of chemical kinetics but is also the most difficult to apply to kinetics problems in natural and engineered systems. Statistical mechanics does not consider the structure of individual molecules but still treats them each as individual entities. It is, therefore, most relevant to the scale of a small (hundreds or thousands of molecules) collection of molecules. Mechanistic kinetics no longer considers molecules as individual entities but, rather, considers all like molecules as belonging to a class called a chemical species. All possible chemical species are treated in a mechanistic kinetic theory and reaction rates are followed by examining fluxes into and out of each class of molecules. This level of theory is applicable to reactions occurring in a well controlled and characterized environment and, therefore, mechanistic kinetics is most relevant at the scale of a

laboratory experiment. Empirical kinetics does not consider all of the possible chemical species but, rather, only those that are particularly important to the reaction kinetics such as the reactant(s) and product(s). This level of kinetic theory is applicable at the laboratory scale but does not require the full knowledge of conditions needed to apply mechanistic kinetics and is, therefore, relevant to systems found in nature and to engineering applications of chemical kinetics such as the FePRBs considered in this thesis.

Transferring information between these scales of theory is the central problem of scaling chemical kinetics. Information may either be transferred up in length scale or down. In scaling up, the task is to utilize information at some scale to predict behavior at the next higher scale. For scaling from quantum mechanics to statistical mechanics, this predictive scaling consists of calculating the probability of transition from the present molecular configuration to all possible future configurations. Statistical mechanical information can be scaled up to the mechanistic kinetics level by determining the mean field solution for the Pauli master equation.

The task in scaling down is to constrain the possible mechanisms at some scale to those that are consistent with the information about the behavior at the next higher level. In this sense, scaling down is a diagnostic process where the nature of the parts of a system are elucidated from the behavior of the whole. In many respects, this diagnostic scaling represents a greater challenge than predictive scaling. Some promising techniques include micro-environment embedding—where a quantum mechanical problem is coupled with a statistical mechanical representation of the system environment—and maximum entropy methods—where, given the constraint of some known mean field solution, the statistical behavior of a system is assumed to maximize entropy generation.

Many of the issues surrounding scaling between quantum mechanics and mechanistic kinetics, especially scaling up, are technical rather than strategic. Effective scaling strategies have already been identified and the remaining challenge is to implement these strategies efficiently. Scaling between mechanistic and empirical kinetics, on the other hand, is a largely unsolved problem with respect to both strategies for scaling and their implementation. Scaling strategies suggested by this thesis include rate limiting step determination, process lumping, and application of approximate rate

laws for scaling up; and bifurcation parameter variation and analysis of kinetic models that are generic with respect to mechanism for scaling down.

1.4 Summary of Contributions

The chemical kinetics of solute reduction by iron metal is necessary information for the design of FePRBs and is an important tool for determining the details of the reaction mechanism. This thesis—focused on scaling between mechanistic and empirical chemical kinetics—has made the following contributions toward improving our understanding of contaminant transformations on iron metal:

(i)   Kinetic expressions for multi-stage reactions—of which heterogeneous reactions are a prime example—are often simplified by pseudo-steady-state and/or pseudo-equilibrium assumptions. Mistaken application of these assumptions is, however, frequently encountered, and little research has addressed the breadth of their applicability. Chapter 2 of this thesis outlines the derivation of common empirical rate laws for heterogeneous reactions using the pseudo-steady-state and pseudo-equilibrium assumptions and addresses the generality of the empirical rate laws from a dynamical systems viewpoint.

(ii)   The most common rate expressions found for iron mediated reduction reactions are the first-order rate law and the Langmuir-Hinshelwood equation. The first-order rate law is also found to be broadly applicable throughout environmental chemistry and the Langmuir-Hinshelwood equation is foundational to heterogeneous catalysis. A principle theoretical challenge to each of these expressions is that they assume rate control by a single reaction or, in the case of iron metal, a single reactive surface site. In chapters 3 and 4 the first-order rate law and the Langmuir-Hinshelwood equation (respectively) are examined as approximate expressions for the kinds of multi-pathway reactions that are likely occurring in complex systems such as reactions on the surface of iron metal.

(iii)   FePRBs have been employed in the treatment of 2,4,6-trinitrotoluene (TNT), however, in laboratory experiments, the appearance of the primary reduction product, 2,4,6-triaminotoluene (TAT), has been found to vary widely. Other

potential products include a host of polymeric amino compounds which are potentially inhibiting to reduction reactions on the iron surface. The distribution of products for the Fe + TNT reaction is, therefore, of considerable interest for assessment of long-term FePRB performance. In chapter 5 a combination of kinetic experiments and kinetic modeling is performed to elucidate reaction mechanisms and to predict the manner in which iron loading and initial TNT concentration control the appearance of TAT versus other, surface bound, products.

1.5 Literature Cited

(1)   Agrawal, A.; Tratnyek, P. G. Reduction of Nitro Aromatic Compounds by Zero-Valent Iron Metal. *Environ. Sci. Technol.* **1996**, *30*, 153.

(2)   Shoemaker, S. H.; Greiner, J. F.; Gillham, R. W. Permeable Reactive Barriers. In *Barrier Containment Technologies for Environmental Remediation Applications (Final Report of the International Containment Technology Workshop, Baltimore, Md, 29-31 August 1995)*; Bodocsi, A., Ryan, M. E., Rumer, R. R., Eds.; Wiley: New York, 1995; pp 301.

(3)   Gillham, R. W.; O'Hannesin, S. F. Enhanced Degradation of Halogenated Aliphatics by Zero-Valent Iron. *Ground Water* **1994**, *32*, 958.

(4)   Johnson, T. L.; Scherer, M. M.; Tratnyek, P. G. Kinetics of Halogenated Organic Compound Degradation by Iron Metal. *Environ. Sci. Technol.* **1996**, *30*, 2634.

(5)   Johnson, T. L.; Fish, W.; Gorby, Y. A.; Tratnyek, P. G. Degradation of Carbon Tetrachloride by Iron Metal: Complexation Effects on the Oxide Surface. *J. Contam. Hydrol.* **1998**, *29*, 377.

(6)   Gotpagar, J. K.; Grulke, E. A.; Bhattacharayya, D. Reductive Dehalogenation of Trichloroethylene: Kinetic Models and Experimental Verification. *J. Haz. Mat.* **1998**, *62*, 243.

(7)   Wüst, W. F.; Köber, R.; Schlicker, O.; Dahmke, A. Combined Zero- and First-Order Kinetic Model of the Degradation of Tce and Cis-Dce with Commercial Iron. *Environ. Sci. Technol.* **1999**, *33*, 4304.

(8)   Scherer, M. M.; Balko, B. A.; Gallagher, D. A.; Tratnyek, P. G. Correlation Analysis of Rate Constants for Dechlorination by Zero-Valent Iron. *Environ. Sci. Technol.* **1998**, *32*, 3026.

(9)   Scherer, M. M.; Balko, B. A.; Tratnyek, P. G. The Role of Oxides in Reduction Reactions at the Metal-Water Interface. In *Mineral-Water Interfacial Reactions: Kinetics and Mechanisms*; Sparks, D. L., Grundl, T. J., Eds.; American Chemical Society: Washington, DC, 1998; Vol. ACS Symp. Ser. 715; pp 301.

(10)   McQuarrie, D. A. Stochastic Approach to Chemical Kinetics. *Journal of Applied Probability* **1967**, *4*, 413.

(11)   Gillespie, D. T. Exact Stochastic Simulation of Coupled Chemical Reactions. *Journal of Physical Chemistry* **1977**, *81*, 2340.

(12)   Van Kampen, N. G. The Expansion of the Master Equation. In *Advances in Chemical Physics*; Prigogine, I., Rice, S., Eds.; John Wiley & Sons: New York, 1976; Vol. 35.

(13)   Arrhenius, S. *Zeitschrift für Physikalische Chemie* **1889**, *4*, 226.

(14)   May, V.; Kuhn, O. *Charge and Energy Transfer Dynamics in Molecular Systems*; Wiley-VCH: Berlin, 2000.

(15)   Glasstone, S.; Laidler, K. J.; Eyring, H. *The Theory of Rate Processes*; McGraw-Hill: New York, 1941.

(16)   Marcus, R. A. Activated-Complex Theory: Current Status, Extensions, and Applications. In *Investigation of Rates and Mechanisms of Reactions*; 3rd ed.; Lewis, E. S., Ed.; Wiley-Interscience: N.Y., 1974; Vol. VI; pp 13.

(17)   Marcus, R. A. On the Theory of Oxidation-Reduction Reactions Involving Electron Transfer. I. *J. Chem. Phys.* **1956**, *24*, 966.

(18)   Moore, J. W.; Pearson, R. G. *Kinetics and Mechanism*; 3rd ed.; Wiley: New York, 1981.

(19)   Temkin, M. I. The Kinetics of Some Industrial Heterogeneous Catalytic Reactions. *Adv. Catal.* **1979**, *28*, 173.
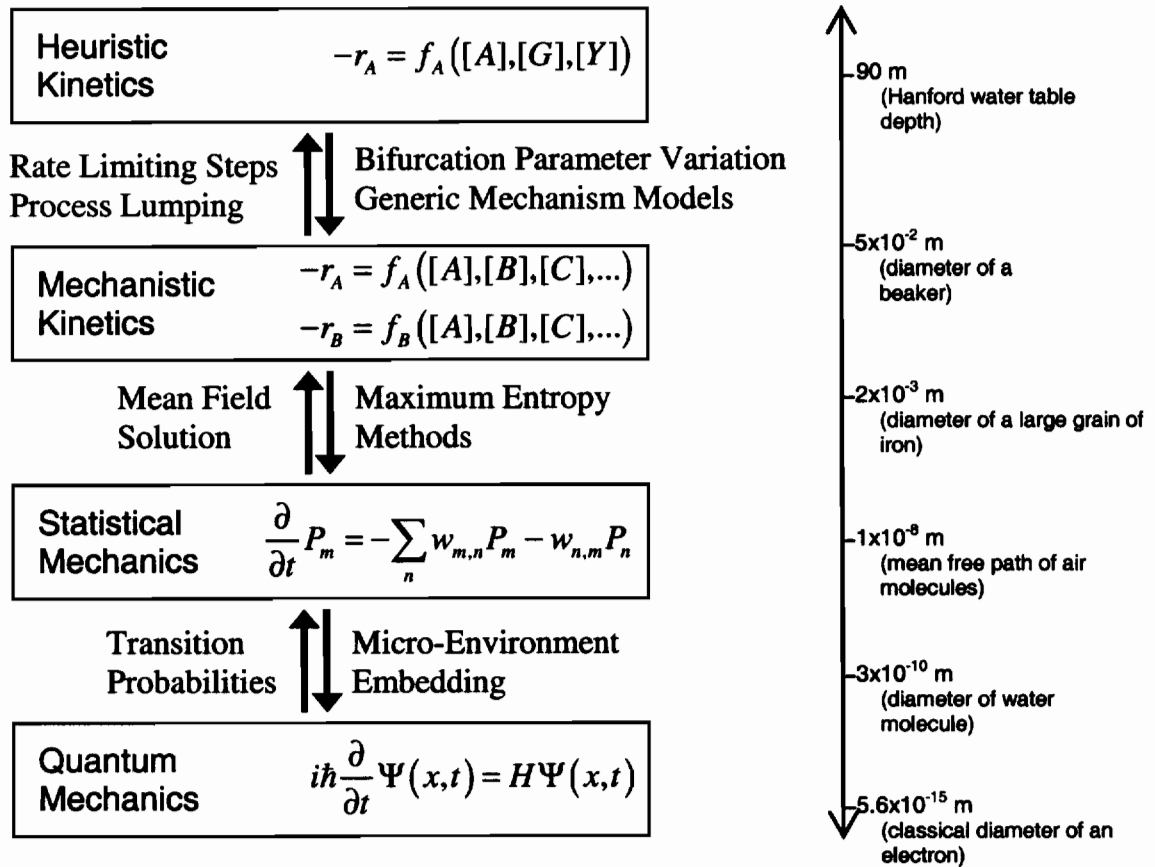
Figure 1.1.   Elements of theoretical chemical kinetics scaled according to the length scale of greatest relevance.

CHAPTER 2

The Theory of Interfacial Chemical Kinetics

2.1 Abstract

Interfacial reactions, such as the transformation of environmental contaminants on Iron metal, involve (*i*) transport of the reactant to the surface, (*ii*) adsorption, (*iii*) transformation of the adsorbed reactant, (*iv*) desorption of products, and (*v*) transport of products away from the surface. The full mathematical statement of the kinetics of interfacial reactions is complex and not usually useful for the analysis of kinetic data or for predicting the fate of contaminants in the environment. In this paper we present the simplifications that lead to commonly applied rate equations including the pseudo-first-order equation, the Langmuir-Hinshelwood equation, and the set of equations for bimodal behavior. The key assumptions in this procedure include pseudo-steady-state assumption—where one or more of the intermediate phases is assumed to have a negligible time derivative—and the pseudo-equilibrium assumption—where one or more of the reversible reactions are assumed to rapidly establish an equilibrium. Analysis of these assumptions indicates that they are rigorously applicable only in certain limiting cases and, further, that the form of the simplified rate equations are correct (either exactly or approximately) over a wider range than that range where pseudo-steady-state or pseudo-equilibrium approximations are applicable.

2.2 Interfacial Kinetics in Environmental Chemistry

2.2.1 Environmental relevance of interfacial redox reactions

A large part of environmental chemistry is concerned with the fate and transport of material within and among compartments, such as surface waters, soil, sediments, groundwater, and air. Increasingly, many researchers are turning their attention to the chemical transformations that occur at the interfaces between compartments. This focus on interfacial chemistry is driven both by the significance of such reactions in fate and transport and by the scientific challenges posed by reactions at interfaces.

The factors that impart environmental significance to interfacial reactions are largely the same as those that have led to the scientific interest in such systems. The asymmetrical nature of the forces at interfaces causes the chemistry in these systems to be quite distinct from that in the bulk phases. These asymmetries present interesting problems for both theoreticians and experimentalists. The same asymmetries can generate highly reactive regions that often determine the lifetimes of chemicals in the environment. Furthermore, interfacial asymmetries may be engineered to mitigate critical contamination problems.

Electron transfer reactions represent an important class of interfacial reactions. Many environmental contaminants are redox active and many remediation schemes rely on manipulating the biogeochemical redox conditions of the media containing the target pollutant. Scientifically, matters of electronic structure form the basis for our understanding of molecules and electron transfer reactions comprise a significant component of our understanding of homogeneous chemical reactions. Furthermore, because electrons are very important to molecular structure, electron transfer reactions offer a prototype for the development of chemical reaction theory. This last point is particularly significant to the study of heterogeneous chemical reactions where the lessons learned from studying heterogeneous electron transfer may be used to develop a coherent view of all surface reactions.

2.2.2 Generalized heterogeneous reaction kinetics.

The general mechanism for a heterogeneous redox reaction is depicted in Figure 2.1. For a reaction to occur, an oxidant molecule in the bulk fluid (Ox) must move to a position near the surface, form a precursor complex with the surface (Ox:S), accept an electron to produce an adsorbed reduced molecule or successor complex, (Red:S), detach from the surface and move back into the bulk fluid (Red).

Concentrations in the bulk—under some velocity field—are given by the advection-diffusion equation (assuming isotropic diffusion in a dilute solution).

$$\frac{\partial[\text{Ox}]}{\partial t} + \vec{v} \cdot \nabla[\text{Ox}] = D_{\text{Ox}} \nabla^2 [\text{Ox}] \tag{1}$$

$$\frac{\partial[\text{Red}]}{\partial t} + \vec{v} \cdot \nabla[\text{Red}] = D_{\text{Red}} \nabla^2 [\text{Red}] \tag{2}$$

Where [Ox] and [Red] are the concentrations of oxidized and reduced molecules at some point, {x, y, z}, in the space of the bulk fluid which is bounded by the reactive surface, $z_{\text{reactive}} = S(x, y)$, and possibly, a non-reactive container wall, $z_{\text{wall}}(x, y)$. $\vec{v}$ denotes the velocity field and D_x denotes the diffusion coefficient of species "x" (Ox or Red). The surface reactions on $S(x, y)$ can be represented as boundary conditions for the system of equations (1 and 2).

$$\frac{\partial[\text{Ox}]_0}{\partial t} = -D_{\text{Ox}} \left(\vec{n} \cdot \nabla[\text{Ox}] \right)_0 - k_{ads}^{\text{Ox}}[\text{S}][\text{Ox}]_0 + k_{des}^{\text{Ox}}[\text{Ox:S}] \tag{3}$$

$$\frac{d[\text{Ox:S}]}{dt} = k_{ads}^{\text{Ox}}[\text{Ox}]_0 - k_{des}^{\text{Ox}}[\text{S}][\text{Ox:S}] - k_{rxn}[\text{Ox:S}] \tag{4}$$

$$\frac{d[\text{Red:S}]}{dt} = k_{rxn}[\text{Ox:S}] + k_{ads}^{\text{Red}}[\text{S}][\text{Red}]_0 - k_{des}^{\text{Red}}[\text{Red:S}] \tag{5}$$

$$\frac{\partial[\text{Red}]_0}{\partial t} = -D_{\text{Red}} \left(\vec{n} \cdot \nabla[\text{Red}] \right)_0 - k_{ads}^{\text{Red}}[\text{S}][\text{Red}]_0 + k_{des}^{\text{Red}}[\text{Red:S}] \tag{6}$$

$$S_{\text{Tot}} = [\text{S}] + [\text{Ox:S}] + [\text{Red:S}] \tag{7}$$

Where $\vec{n}$ is the unit vector normal to the reactive surface, [S] is the concentration of reactive surface sites (per unit volume of solution), [Ox:S] and [Red:S] are concentrations

of molecules adsorbed to the surface (per unit volume of solution), and the k's are rate constants for the chemical reaction specified by the subscripts and superscripts. To complete the set of equations, flux boundary conditions must be specified that are specific to the type of reactor being considered (e.g., no flux across the container walls in a batch reactor or flux in and flux out of a fixed bed reactor).

The full solution to equations (1-6) involves solving the Navier-Stokes equations for $\bar{v}$ as well as exactly specifying the geometry of the reactive surface and accounting for any movement of that surface. The level of detail involved in such a solution is not available for most systems and, therefore, the mass transport equations are simplified by assuming a (locally) well mixed bulk solution with a stagnant boundary layer. The boundary layer is assumed to be of constant thickness between the bulk fluid and the reactive surface across which Ox (and Red) molecules must diffuse before (and after) reacting as shown in Figure 2.2. We then assume that the concentration gradient in the boundary layer instantly attains a steady-state so that equations (1-2) may be set = 0 giving a linear concentration profile in the boundary layer between the bulk concentrations ([Ox] and [Red]) and the surface concentrations ([Ox]$_0$ and [Red]$_0$).

$$[Ox]_\zeta = \frac{[Ox]-[Ox]_0}{\delta_{Ox}}\zeta + [Ox]_0 \tag{8}$$

$$[Red]_\zeta = \frac{[Red]-[Red]_0}{\delta_{Red}}\zeta + [Red]_0 \tag{9}$$

Where ζ is the distance from the reactive surface. The diffusive fluxes of Ox and Red normal to the reactive surface and can be calculated as follows:

$$-D_{Ox}\left(\bar{n}\cdot\nabla[Ox]\right) = -D_{Ox}\left(\hat{\zeta}\cdot\frac{[Ox]-[Ox]_0}{\delta_{Ox}}\hat{\zeta}\right) = -\frac{D_{Ox}}{\delta_{Ox}}\left([Ox]-[Ox]_0\right) \tag{10}$$

$$-D_{Red}\left(\bar{n}\cdot\nabla[Red]\right) = -D_{Red}\left(\hat{\zeta}\cdot\frac{[Red]-[Red]_0}{\delta_{Red}}\hat{\zeta}\right) = -\frac{D_{Red}}{\delta_{Red}}\left([Red]-[Red]_0\right) \tag{11}$$

Differential equations can now be derived for the bulk concentrations by considering advective fluxes in and out of a control volume and a sink term due to diffusion into (or out of) the boundary layer surrounding any reactive surfaces in that control volume.

$$\frac{d[\text{Ox}]}{dt} = -\frac{1}{V_{\text{CV}}} \oiint \bar{J}_{\text{Ox}} \cdot \bar{n} \, ds - k_{MT}^{\text{Ox}} \rho_a \left([\text{Ox}] - [\text{Ox}]_0\right) \tag{12}$$

$$\frac{d[\text{Red}]}{dt} = -\frac{1}{V_{\text{CV}}} \oiint \bar{J}_{\text{Red}} \cdot \bar{n} \, ds - k_{MT}^{\text{Red}} \rho_a \left([\text{Red}] - [\text{Red}]_0\right) \tag{13}$$

Where k_{MT}^{χ} is the mass transfer coefficient for χ and $\bar{J}_{\chi}$ denotes the flux of χ (i.e., moles or χ per unit time per unit area) across the surface of a control volume of size V_{CV} with unit vector, $\bar{n}$, normal to the surface (i.e., pointing outward from the control volume). The surface integrals in equations (12-13) are > 0 for a net flow of X out of the control volume. The selection of the control volume is not arbitrary since the applicability of equations (12-13) requires that the concentration of Ox and Red be constant within the control volume. We discuss the selection of control volumes for common reactor designs in the next section.

The simplified version of equations (3-7) are found by substituting equations (10) and (11) for the diffusive flux terms in equations (3) and (7)

$$\frac{d[\text{Ox}]_0}{dt} = k_{MT}^{\text{Ox}} \rho_a \left([\text{Ox}] - [\text{Ox}]_0\right) - k_{ads}^{\text{Ox}} [\text{S}][\text{Ox}]_0 + k_{des}^{\text{Ox}} [\text{Ox:S}] \tag{14}$$

$$\frac{d[\text{Ox:S}]}{dt} = k_{ads}^{\text{Ox}} [\text{S}][\text{Ox}]_0 - k_{des}^{\text{Ox}} [\text{Ox:S}] - k_{rxn} [\text{Ox:S}] \tag{15}$$

$$\frac{d[\text{Red:S}]}{dt} = k_{rxn} [\text{Ox:S}] + k_{ads}^{\text{Red}} [\text{S}][\text{Red}]_0 - k_{des}^{\text{Red}} [\text{Red:S}] \tag{16}$$

$$\frac{d[\text{Red}]_0}{dt} = k_{MT}^{\text{Red}} \rho_a \left([\text{Red}] - [\text{Red}]_0\right) - k_{ads}^{\text{Red}} [\text{S}][\text{Red}]_0 + k_{des}^{\text{Red}} [\text{Red:S}] \tag{17}$$

$$S_{\text{Tot}} = [\text{S}] + [\text{Ox:S}] + [\text{Red:S}] \tag{18}$$

Equations (12-18) can be viewed as the set of rate laws that apply to the multi-stage reaction depicted in Scheme 1 where mass transport is treated as the first and last reversible steps in the reaction sequence.

$$\text{Ox} \underset{k_{MT}}{\overset{k_{MT}}{\rightleftharpoons}} \text{Ox}_0 + \text{S} \underset{k_{des}}{\overset{k_{ads}}{\rightleftharpoons}} \text{Ox:S} \xrightarrow{k_{rxn}} \text{Red:S} \underset{k_{des}}{\overset{k_{ads}}{\rightleftharpoons}} \text{Red}_0 + \text{S} \underset{k_{MT}}{\overset{k_{MT}}{\rightleftharpoons}} \text{Red} \qquad \text{Scheme 1}$$
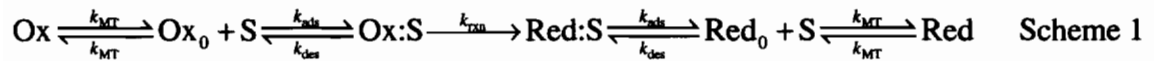
The mass balance equation must, however, be modified from what would be implied by Scheme 1 to account for the fact that a given concentration in the bulk of the control volume may contribute a different number of total molecules than that of the same concentration in the boundary layer. This can be done by considering the total moles of Ox and Red in the control volume:

Total Moles = Bulk Moles + Boundary Layer Moles + Adsorbed Moles

$$(19)$$

$$= \left(\begin{array}{l} [Ox]V_{Bulk} + [Red]V_{Bulk} \\ + \dfrac{[Ox]+[Ox]_0}{2}V_{BL}^{Ox} + \dfrac{[Red]+[Red]_0}{2}V_{BL}^{Red} \\ + [Ox:S]V_{Tot} + [Red:S]V_{Tot} \end{array} \right)$$

Where V_{Bulk} is the volume of the bulk solution, V_{BL}^{x} is the volume of the appropriate boundary layer, and V_{Tot} is the total solution volume in the control volume.

2.3 Types of Kinetic Data for Reduction of Contaminants by Iron Metal

2.3.1 Batch Reactor

The kinetics of reactions on granular iron metal are often investigated by introducing the contaminant of interest into a slurry of water and granular iron in a closed vessel, applying a means of mixing the slurry, and sampling, over time, the mixture for concentrations of the contaminant and/or daughter products. In this type of reactor, known as a batch reactor, the bulk solution should be well mixed so the control volume in equations (12-13) can be taken as the entire vessel. During the course of the reaction there are no fluxes into the vessel and the only flux out of the vessel is through the sampling actions, which are designed to be small relative to the reactor volume. The surface integrals in equations (12-13) can, therefore, be set $= 0$ which gives the following equations in the place of equations (12-13).

$$\frac{d[Ox]}{dt} = -k_{MT}^{Ox}\rho_a\left([Ox]-[Ox]_0\right) \tag{20}$$

$$\frac{d[Red]}{dt} = -k_{MT}^{Red}\rho_a\left([Red]-[Red]_0\right) \tag{21}$$

Equations (14-18) remain the same.

The kinetic data produced in a batch reactor are time series of concentration data such as those shown in Figure 2.3 for 2,4,6-trinitrotoluene (TNT) reacting with granular iron (12.5 g/L Fisher electrolytic). In general, the kinetic model contained in equations (20-21) and (14-18) is over-parameterized for the treatment of such kinetic data and, therefore, simplifications must be made. The necessary simplifications depend on the kinetic regime that is observed in the data. Common kinetic regimes and the associated simplifications are discussed in Section 2.4.

2.3.2 Column Reactor

Under environmental conditions, interfacial reactions typically involve water moving past the (relatively) fixed surfaces of soil, sediment, or aquifer grains. To simulate these conditions in the laboratory, the kinetics of contaminant transformation are studied in columns filled with granular material and have a contaminant containing solution as the influent. The flow in such a column reactor can be treated as one-dimensional along the length of the column and the bulk fluid can be assumed to be well mixed along the plane normal to the direction of the flow. Under these assumptions, the appropriate control volume for a column reactor is a differential slice across the column with area equal to the cross-sectional area of the fluid phase in the reactor (i.e., the cross-sectional area of the column less that area occupied by solids).

$$V_{CV} = \lim_{\Delta x \to 0} \varepsilon A_{x\text{-sec}} \Delta x \tag{22}$$

where ε is the porosity of the column, $A_{x\text{-sec}}$ is the cross-sectional area of the column, and Δx is the thickness of the control volume. The fluxes of χ (Ox or Red) in and out of the control volume are due to advection and diffusion.

$$\bar{J}_{in}^{\chi} = \left(v\,[X]_x - D_{\chi} \frac{\partial[\chi]}{\partial x}\bigg|_x \right) \hat{x} \tag{23}$$

$$\bar{J}_{out}^{\chi} = \left(v\,[\chi]_{x+dx} - D_{\chi} \frac{\partial[\chi]}{\partial x}\bigg|_{x+dx} \right) \hat{x} \tag{24}$$

where v is the magnitude of the velocity and $\hat{x}$ is the unit vector in the direction of the flow. $\bar{n}$ is $-\hat{x}$ for the portion of the control volume corresponding to $\bar{J}_{in}^{\chi}$ and $\hat{x}$ for the

portion corresponding to $\bar{J}_{out}^{\chi}$. The surface integrals in equations (12-13) can then be evaluated as follows:

$$\frac{1}{V_{CV}} \oiint \bar{J}_{\chi} \cdot \bar{n} \, ds V_{CV} = \lim_{\Delta x \to 0} \frac{1}{\varepsilon A_{x\text{-sec}} \Delta x} \left(\begin{array}{c} \varepsilon A_{x\text{-sec}} \left(v \, [\chi]_x - D_{\chi} \left. \frac{\partial [\chi]}{\partial x} \right|_x \right) \hat{x} \cdot (-\hat{x}) \\ + \varepsilon A_{x\text{-sec}} \left(v \, [\chi]_{x+\Delta x} - D_{\chi} \left. \frac{\partial [\chi]}{\partial x} \right|_{x+\Delta x} \right) \hat{x} \cdot (\hat{x}) \end{array} \right) \quad (25)$$

$$= v \frac{\partial [X]}{\partial x} - D_X \frac{\partial^2 [X]}{\partial x^2}$$

Substitution of equation 25 into equations (12-13) gives:

$$\frac{d[Ox]}{dt} = -v \frac{\partial [Ox]}{\partial x} + D_X \frac{\partial^2 [Ox]}{\partial x^2} - k_{MT}^{Ox} \rho_a \left([Ox] - [Ox]_0 \right) \quad (26)$$

$$\frac{d[Red]}{dt} = -v \frac{\partial [Red]}{\partial x} + D_X \frac{\partial^2 [Red]}{\partial x^2} - k_{MT}^{Red} \rho_a \left([Red] - [Red]_0 \right) \quad (27)$$

Equations (14-18) remain the same. Ignoring the diffusion terms (i.e., plug flow) and the time derivatives (i.e., steady-state operation) gives a more familiar form of equations (26-27):

$$v \frac{d[Ox]}{dx} = -k_{MT}^{Ox} \rho_a \left([Ox] - [Ox]_0 \right) \quad (28)$$

$$v \frac{d[Red]}{dx} = -k_{MT}^{Red} \rho_a \left([Red] - [Red]_0 \right) \quad (29)$$

As implied by equations (28-29), kinetics in a column reactor are usually examined by sampling steady-state concentrations along the length of the column. An example of concentration vs. distance data collected in a column reactor is shown in Figure 2.4.

2.4 Kinetic Models for Interpretation of Heterogeneous Kinetic Data

2.4.1 Pseudo-First-Order Kinetics

Numerous studies on the kinetics of contaminant reduction by iron metal have produced disappearance data that are sufficiently described by a first-order rate law [1-5].

$$r_{Ox} = -k_{obs}[Ox] \quad (30)$$

where r_{Ox} is the rate of Ox disappearance and k_{obs} is the first-order rate constant. In a batch reactor, $r_{Ox} = d[Ox] / dt$ and [Ox] disappears geometrically with time. In a steady-

state column reactor $r_{Ox} = v\, d[Ox]\,/\,dx$. In a column operated at steady state, $[Ox]$ disappears geometrically with distance.

First-order reaction kinetics can arise from a variety of kinetic scenarios (ref FOC). In heterogeneous systems, these include mechanisms where one of the stages in scheme 1 is rate limiting, such as mass transfer control, adsorption control, and surface reaction control (with abundant surface sites). First-order disappearance kinetics can also arise when the rate of reaction is controlled by multiple first-order processes in series such as mass transfer and surface reaction (with abundant surface sites).

A first-order rate equation that is appropriate for any of the possible rate limiting steps or cases of mixed control can be derived by assuming that active sites are present in an abundance (i.e., $d[S]/dt = 0$) and that the time derivatives of $[Ox]_0$ and $[Ox:S]$ can be neglected in equations (14-15). This last assumption is known as pseudo-steady-state [6] because the intermediate species are treated as being in steady-state though their concentrations change in response to changes in the concentrations of the parent compound. The pseudo-steady-state assumption can be written formally as:

$$0 = k_{MT}^{Ox} \rho_a \left([Ox] - [Ox]_0\right) - k_{ads}^{Ox}[S][Ox]_0 + k_{des}^{Ox}[Ox:S] \tag{31}$$

$$0 = k_{ads}^{Ox}[S][Ox]_0 - k_{des}^{Ox}[Ox:S] - k_{rxn}[Ox:S] \tag{32}$$

Equations (31-32) can be rearranged to give expressions for $[Ox]_0$ and $[Ox:S]$ in terms of $[Ox]$.

$$[Ox]_0 = \frac{k_{MT}^{Ox}\rho_a k_{des}^{Ox} + k_{MT}^{Ox}\rho_a k_{rxn}}{k_{MT}^{Ox}\rho_a k_{des}^{Ox} + k_{MT}^{Ox}\rho_a k_{rxn} + k_{ads}^{Ox}[S]k_{rxn}}[Ox] \tag{33}$$

$$[Ox:S] = \frac{k_{MT}^{Ox}\rho_a k_{ads}^{Ox}[S]}{k_{MT}^{Ox}\rho_a k_{des}^{Ox} + k_{MT}^{Ox}\rho_a k_{rxn} + k_{ads}^{Ox}[S]k_{rxn}}[Ox] \tag{34}$$

Substituting equation (33) into equation (12) gives:

$$\frac{d[Ox]}{dt} = -\frac{1}{V_{CV}}\oiint \vec{J}_{Ox}\cdot\vec{n}\ ds - k_{MT}^{Ox}\rho_a\left(\frac{k_{ads}^{Ox}[S]k_{rxn}}{k_{MT}^{Ox}\rho_a k_{des}^{Ox} + k_{MT}^{Ox}\rho_a k_{rxn} + k_{ads}^{Ox}[S]k_{rxn}}\right)[Ox] \tag{35}$$

Equation (35) is a first-order rate law only if $[S]$ is constant. We consider the case where $[S]$ is variable in the next section but here we assume

$$[S] = \Gamma_{\text{Tot}} \rho_a \tag{36}$$

Where Γ_{Tot} denotes the surface concentration of reactive sites. This allows us to express equation (35) as a first-order rate expression:

$$\frac{d[Ox]}{dt} = -\frac{1}{V_{CV}} \oiint \vec{J}_{Ox} \cdot \vec{n} \, ds - k_{SA} \rho_a [Ox] \tag{37}$$

$$k_{SA} = \frac{1}{\dfrac{k_{des}^{Ox}}{k_{ads}^{Ox} \Gamma_{\text{Tot}} k_{rxn}} + \dfrac{1}{k_{ads}^{Ox} \Gamma_{\text{Tot}}} + \dfrac{1}{k_{MT}^{Ox}}} \tag{38}$$

Where k_{SA} is the surface area normalized first-order rate constant.

If a single stage in scheme 1 is rate limiting, the appropriate rate-constant can be obtained by finding the limit of equation (38) as the non-rate limiting terms approach ∞. For mass transport limited reactions, letting k_{ads}^{Ox}, k_{des}^{Ox}, and $k_{rxn} \to \infty$ gives:

$$k_{SA} = k_{MT}^{Ox} \tag{39}$$

For adsorption limited reactions, letting k_{MT}^{Ox}, $k_{rxn} \to \infty$ gives:

$$k_{SA} = k_{ads}^{Ox} \Gamma_{\text{Tot}} \tag{40}$$

For surface reaction limited reactions, letting k_{MT}^{Ox}, k_{ads}^{Ox}, $k_{des}^{Ox} \to \infty$ gives:

$$k_{SA} = \frac{k_{ads}^{Ox} \Gamma_{\text{Tot}}}{k_{des}^{Ox}} k_{rxn} \tag{41}$$

Where the ratio of k_{ads}^{Ox} to k_{des}^{Ox} is finite even though the individual rate constants are taken to be infinite.

2.4.2 Site-Limited Kinetics

A number of studies have demonstrated mixed order kinetics [7-13] where the disappearance rate is constant (i.e., zero-order) at high concentrations and proportional to [Ox] (i.e., first-order) at low concentrations. An example of mixed order disappearance data collected in a batch reactor is shown in Figure 2.5.

A rate law that captures the observed mixed order behavior can be derived by relaxing the abundant site assumption in the derivation of equation (37) and including only intra-species competition for reactive sites (i.e., ignoring [Red:S] in equation 18).

Assuming a steady-state for [Ox:S] (i.e., setting equation 11 to zero) and substituting equation (18) with [Red:S] = 0 gives the following expressions for [S] and [Ox:S].

$$[S] = S_{Tot} \frac{1}{1 + \frac{k_{ads}^{Ox}}{k_{des}^{Ox} + k_{rxn}}[Ox]_0} \tag{42}$$

$$[Ox:S] = S_{Tot} \frac{\frac{k_{ads}^{Ox}}{k_{des}^{Ox} + k_{rxn}}[Ox]_0}{1 + \frac{k_{ads}^{Ox}}{k_{des}^{Ox} + k_{rxn}}[Ox]_0} \tag{43}$$

Substituting equation (42-43) into equation (14) and defining $K_{LH}^{Ox} = k_{ads}^{Ox}/(k_{des}^{Ox} + k_{rxn})$ yields a simplified form of equation (14).

$$\frac{d[Ox]_0}{dt} = k_{MT}^{Ox}\rho_a \left([Ox] - [Ox]_0\right) - \frac{S_{Tot}k_{rxn}K_{LH}^{Ox}[Ox]_0}{1 + K_{LH}^{Ox}[Ox]_0} \tag{44}$$

Equation (44) taken with equation (12) gives a complete system of equations for Ox disappearance with intra-species competition for reactive sites and potential mass transfer effects. If mass transfer is relatively fast, equations (12) and (44) simplify to the Langmuir-Hinshelwood equation for surface mediated reactions.

$$\frac{d[Ox]}{dt} = -\frac{S_{Tot}k_{rxn}K_{LH}^{Ox}[Ox]}{1 + K_{LH}^{Ox}[Ox]} \tag{45}$$

Equation (45) is analogous to the Mechalis-Menton equation for enzyme kinetics and is also referred to as the Hougen-Watson equation. In the limit of large [Ox], equation (45) approaches a zero-order rate-law.

$$\lim_{Ox \to \infty} \frac{d[Ox]}{dt} = \lim_{Ox \to \infty} -\frac{S_{Tot}k_{rxn}K_{LH}^{Ox}[Ox]}{1 + K_{LH}^{Ox}[Ox]} = -S_{Tot}k_{rxn} \tag{46}$$

In the limit of small [Ox], equation (45) approaches a first-order rate law.

$$\lim_{Ox \to 0} \frac{d[Ox]}{dt} = \lim_{Ox \to 0} -\frac{S_{Tot}k_{rxn}K_{LH}^{Ox}[Ox]}{1 + K_{LH}^{Ox}[Ox]} = \lim_{Ox \to 0} -S_{Tot}k_{rxn}K_{LH}^{Ox}[Ox] \tag{47}$$

A rate equation that is similar in form to equation (45) can also be derived by assuming a rapidly established equilibrium of the Ox adsorption reaction. We compare these two approaches, pseudo-steady-state analysis and pseudo-equilibrium analysis, in section 2.5.

The approach used in deriving the Langmuir-Hinshelwood equation can also be used to derive a rate-law that includes inter-species competition for reactive sites. Here we address product inhibition due to accumulation of Red on the surface but the approach may also be used for inhibitory species that do not participate in the reaction sequence depicted in scheme 1.

As with the derivation of the Langmuir-Hinshelwood equation we assume a steady-state for [Ox:S] by setting equation (15) to zero. Product inhibition is included by relaxing the [Red:S] = 0 condition and, instead, assuming a steady-state for [Red:S] by setting equation (16) to zero. These two steady-state conditions, along with equation (18) give the following equations for [S], [Ox:S], and [Red:S]:

$$[S] = \frac{S_{Tot}}{1 + \frac{k_{ads}^{Ox}\left(k_{des}^{Red} + k_{rxn}\right)}{k_{des}^{Red}\left(k_{des}^{Ox} + k_{rxn}\right)}[Ox]_0 + \frac{k_{ads}^{Red}}{k_{des}^{Red}}[Red]_0} \tag{48}$$

$$[Ox:S] = \frac{S_{Tot}\dfrac{k_{ads}^{Ox}}{k_{des}^{Ox} + k_{rxn}}[Ox]_0}{1 + \dfrac{k_{ads}^{Ox}\left(k_{des}^{Red} + k_{rxn}\right)}{k_{des}^{Red}\left(k_{des}^{Ox} + k_{rxn}\right)}[Ox]_0 + \dfrac{k_{ads}^{Red}}{k_{des}^{Red}}[Red]_0} \tag{49}$$

$$[Red:S] = \frac{S_{Tot}\left(\dfrac{k_{rxn}k_{ads}^{Ox}}{k_{des}^{Red}\left(k_{des}^{Ox} + k_{rxn}\right)}[Ox]_0 + \dfrac{k_{ads}^{Red}}{k_{des}^{Red}}[Red]_0\right)}{1 + \dfrac{k_{ads}^{Ox}\left(k_{des}^{Red} + k_{rxn}\right)}{k_{des}^{Red}\left(k_{des}^{Ox} + k_{rxn}\right)}[Ox]_0 + \dfrac{k_{ads}^{Red}}{k_{des}^{Red}}[Red]_0} \tag{50}$$

Substituting equation (49) into equation (14) and equation (50) into equation (17) gives simplified rate equations for [Ox]$_0$ and [Red]$_0$ that, when taken together with equations (12-13), form a complete set of differential equations.

$$\frac{d[Ox]_0}{dt} = k_{MT}^{Ox}\rho_a\left([Ox] - [Ox]_0\right) - \frac{k\rho_a K_{Ox}[Ox]_0}{1 + K_{Ox}[Ox]_0 + K_{Red}[Red]_0} \tag{51}$$

$$\frac{d[Red]_0}{dt} = k_{MT}^{Red}\rho_a\left([Red] - [Red]_0\right) + \frac{k\rho_a K_{Ox}[Ox]_0}{1 + K_{Ox}[Ox]_0 + K_{Red}[Red]_0} \tag{52}$$

Where k, K_{Ox}, and K_{Red} are defined as follows:

$$k\rho_a = S_{Tot}k_{rxn}\frac{k_{des}^{Red}}{k_{des}^{Red} + k_{rxn}} \tag{53}$$

$$K_{Ox} = \frac{k_{ads}^{Ox}\left(k_{des}^{Red} + k_{rxn}\right)}{k_{des}^{Red}\left(k_{des}^{Ox} + k_{rxn}\right)}$$

(54)

$$K_{Red} = \frac{k_{ads}^{Red}}{k_{des}^{Red}}$$

(55)

When mass transfer is relatively fast, equations (12-13) and (51-52) simplify to the form commonly employed when examining product inhibition effects.

$$\frac{d[Ox]}{dt} = -\frac{k\rho_a K_{Ox}[Ox]}{1 + K_{Ox}[Ox] + K_{Red}[Red]}$$

(56)

$$\frac{d[Red]}{dt} = \frac{k\rho_a K_{Ox}[Ox]}{1 + K_{Ox}[Ox] + K_{Red}[Red]}$$

(57)

2.4.3 Bimodal Kinetics

Before establishing the steady-state kinetic regimes described above, many reactor designs must pass through a transient induction period. In the batch reactor this transient region usually takes the form of an initial drop in [Ox] that is substantially steeper than the remainder of the disappearance curve (ref TNT paper). In most cases where an initial drop is observed, it consists of only a few points which are ignored in the analysis of the data. In other cases, the initial drop is so large that it fully dominates the observable kinetics. These two endpoints are the surface controlled and mass transport/adsorption controlled kinetics discussed above. In some cases, however, both the initial drop and steady-state kinetics are sufficiently well resolved so that the reaction kinetics must be treated as having two distinct regions. An example of such data is depicted in Figure 2.6 where TNT is being reduced by iron metal.

The fitted curve shown in Figure 2.6 is the sum of two decreasing exponentials.

$$[Ox] = \alpha_+ \exp\left(r_+ t\right) + \alpha_- \exp\left(r_- t\right)$$

(58)

A triple exponential expression for [Ox] vs. t in a batch reactor can be obtained from equations (12-18) by assuming abundant sites and treating [S] as a constant (= S_{Tot}). A triple exponential is, however, over-parameterized for most data displaying an initial drop and, therefore, the mass transport and adsorption stages in Scheme 1 must be lumped as depicted in Scheme 2.

$$Ox + S \underset{k_{MT/des}^{Ox}}{\overset{k_{MT/ads}^{Ox}}{\rightleftharpoons}} Ox{:}S \xrightarrow{k_{rxn}} Red + S \qquad \text{Scheme 2}$$

This can be accomplished by applying a steady-state assumption to either $[Ox]_0$ (i.e., setting equation 14 to zero) or $[Ox{:}S]$ (i.e., setting equation 15 to zero).

We can determine which of the two steady-state conditions is appropriate by examining mass balance equations based on equation (19). In a typical batch experiment, mass is introduced as Ox and into the bulk solution. The total moles is, therefore, given as:

$$\text{Total Moles} = [Ox]\big|_{t=0} V_{\text{Bulk}} \qquad (59)$$

Since the initial concentrations of $[Ox]_0$ and $[Ox{:}S]$ are zero, the reaction is not in the pseudo-steady-state defined by equations (33-34). We can, however, calculate the amount of material that would have to be transferred from the bulk to the boundary layer and surface in order to achieve steady-state by equating equation (59) to the mass balance equation for this virtual transition giving

$$[Ox]\big|_{t=0} V_{\text{Bulk}} = [Ox]^{SS} V_{\text{Bulk}} + \frac{[Ox]^{SS} + [Ox]_0^{SS}}{2} V_{\text{BL}}^{Ox} + [Ox{:}S]^{SS}\left(V_{\text{Bulk}} + V_{\text{BL}}^{Ox}\right) \qquad (60)$$

Where the "SS" superscripts denote the virtual steady-state concentrations. Equations (33-34) give relationships between the steady-state concentrations and substituting these relationships into (60) along with the abundant site assumption gives:

$$[Ox]\big|_{t=0} V_{\text{Bulk}} = [Ox]^{SS}\left(\begin{array}{l} V_{\text{Bulk}} + \dfrac{1}{2}\left(1 + \dfrac{k_{MT}^{Ox} k_{des}^{Ox} + k_{MT}^{Ox} k_{rxn}}{k_{MT}^{Ox} k_{des}^{Ox} + k_{MT}^{Ox} k_{rxn} + k_{ads}^{Ox}\Gamma_{Tot} k_{rxn}}\right) V_{\text{BL}}^{Ox} \\[2em] + \dfrac{k_{MT}^{Ox} k_{ads}^{Ox}\Gamma_{Tot}\rho_a}{k_{MT}^{Ox} k_{des}^{Ox} + k_{MT}^{Ox} k_{rxn} + k_{ads}^{Ox}\Gamma_{Tot} k_{rxn}}\left(V_{\text{Bulk}} + V_{\text{BL}}^{Ox}\right) \end{array}\right) \qquad (61)$$

The second term inside the parentheses is ≤ 1 and, therefore, since the volume of the boundary layer, V_{BL}^{Ox}, is much smaller than the volume of the bulk, V_{Bulk}, we can ignore contributions from the boundary layer to the total mass and the total volume giving the following relationships between the initial concentration, $[Ox]\big|_{t=0}$, and the initial concentrations for the virtual steady-state.

$$[Ox]^{SS} = \frac{k_{MT}^{Ox} k_{des}^{Ox} + k_{MT}^{Ox} k_{rxn} + k_{ads}^{Ox}\Gamma_{Tot} k_{rxn}}{k_{MT}^{Ox} k_{des}^{Ox} + k_{MT}^{Ox} k_{rxn} + k_{ads}^{Ox}\Gamma_{Tot} k_{rxn} + k_{MT}^{Ox} k_{ads}^{Ox}\Gamma_{Tot}\rho_a}[Ox]\big|_{t=0} \qquad (62)$$

$$[Ox]_0^{SS} = \frac{k_{MT}^{Ox}k_{des}^{Ox} + k_{MT}^{Ox}k_{rxn}}{k_{MT}^{Ox}k_{des}^{Ox} + k_{MT}^{Ox}k_{rxn} + k_{ads}^{Ox}\Gamma_{Tot}k_{rxn} + k_{MT}^{Ox}k_{ads}^{Ox}\Gamma_{Tot}\rho_a}[Ox]|_{t=0}$$ (63)

$$[Ox{:}S]^{SS} = \frac{k_{MT}^{Ox}k_{ads}^{Ox}\Gamma_{Tot}\rho_a}{k_{MT}^{Ox}k_{des}^{Ox} + k_{MT}^{Ox}k_{rxn} + k_{ads}^{Ox}\Gamma_{Tot}k_{rxn} + k_{MT}^{Ox}k_{ads}^{Ox}\Gamma_{Tot}\rho_a}[Ox]|_{t=0}$$ (64)

Little of the transferred mass in establishing a steady-state resides in the boundary layere indicating that the kinetics of the initial drop in the double exponential are predominately controlled by the kinetics of reaching a steady-state in [Ox:S]. We can, therefore, lump the mass transport and adsorption processes by assuming a pseudo-steady-state in $[Ox]_0$. Setting equation (14) = 0, along with the abundant site assumption, gives an expression for $[Ox]_0$.

$$[Ox]_0 = \frac{k_{MT}^{Ox}\rho_a[Ox] + k_{des}^{Ox}[Ox{:}S]}{k_{MT}^{Ox}\rho_a + k_{ads}^{Ox}S_{Tot}}$$ (65)

Substitution of equation (65) into equations (12) and (15) gives a set of differential equations that apply to Scheme 2 and lead to a double exponential expression for [Ox] disappearance in batch (equation 58).

$$\frac{d[Ox]}{dt} = -\frac{1}{V_{CV}}\oiint \bar{J}_{Ox}\cdot\bar{n}\,ds - \frac{k_{MT}^{Ox}\rho_a k_{ads}^{Ox}S_{Tot}}{k_{MT}^{Ox}\rho_a + k_{ads}^{Ox}S_{Tot}}[Ox] + \frac{k_{MT}^{Ox}\rho_a k_{des}^{Ox}}{k_{MT}^{Ox}\rho_a + k_{ads}^{Ox}S_{Tot}}[Ox{:}S]$$ (66)

$$\frac{d[Ox{:}S]}{dt} = \frac{k_{MT}^{Ox}\rho_a k_{ads}^{Ox}S_{Tot}}{k_{MT}^{Ox}\rho_a + k_{ads}^{Ox}S_{Tot}}[Ox] - \frac{k_{MT}^{Ox}\rho_a k_{des}^{Ox}}{k_{MT}^{Ox}\rho_a + k_{ads}^{Ox}S_{Tot}}[Ox{:}S] - k_{rxn}[Ox{:}S]$$ (67)

Equations (66-67) imply definitions for the rate constants on the lumped mass transfer/adsorption stage in scheme 1.

$$k_{MT/ads}^{Ox}\rho_a = \frac{k_{MT}^{Ox}\rho_a k_{ads}^{Ox}S_{Tot}}{k_{MT}^{Ox}\rho_a + k_{ads}^{Ox}S_{Tot}}$$ (68)

$$k_{MT/des}^{Ox} = \frac{k_{MT}^{Ox}\rho_a k_{des}^{Ox}}{k_{MT}^{Ox}\rho_a + k_{ads}^{Ox}S_{Tot}}$$ (69)

Note that equation (68) has a linear dependence on ρ_a and equation (69) does not depend on ρ_a. Equations (66-67) can be applied to a batch reactor by setting the surface integral in equation (66) to zero. The solution to this system of equations in terms of [Ox] is given by equation (58) with eigenvalues, $r_{+/-}$, and pre-exponentials, $\alpha_{+/-}$, given as follows:

$$r_{+/-} = \frac{-\left(k_{MT/ads}^{Ox}\rho_a + k_{MT/des}^{Ox} + k_{rxn}\right) \pm \sqrt{\left(k_{MT/ads}^{Ox}\rho_a + k_{MT/des}^{Ox} + k_{rxn}\right)^2 - 4k_{MT/ads}^{Ox}\rho_a k_{rxn}}}{2} \qquad (70)$$

$$\alpha_{+/-} = [Ox]|_{t=0}\frac{r_{-/+} + k_{MT/ads}^{Ox}\rho_a}{r_{-/+} - r_{+/-}} \qquad (71)$$

Figure 2.7 shows $|r_{+/-}|$ (Figure 2.7A) and $\alpha_{+/-}$ (Figure 2.7B) as functions of ρ_m (the mass concentration of iron) using rate constants derived from fitting equation (58) to the data shown in Figure 2.6. From equation (70) we can see that both r_+ and r_- are < 0 and that the magnitude of r_+ is less than the magnitude of r_- (i.e., $|r_+| < |r_-|$). This implies that the initial drop is dominated by r_- while the slower portion of the bimodal kinetics is controlled by r_+. Since the initial drop can be interpreted as mass transfer/adsorption controlled kinetics and the slower portion can be interpreted as pseudo-steady-state reaction controlled kinetics we can compare r_- to $k_{MT/ads}^{Ox}\rho_a$ and r_+ to the first-order rate constant derived in Section 2.4.1 (see equations 37-38).

2.5 Critique of Steady State and Equilibrium Assumptions

The kinetic equations for multi-stage reactions (such as the reaction depicted in scheme 1 above) are often simplified by assuming the reaction to be in a steady state [6]. In reactors comprised of one or more flow through cells (such as a CSTR or PFR), this procedure, performed by setting all time derivatives to zero, finds, exactly, the fixed point attractor of equations (8-14). The steady-state equations describe the total amount of conversion that occurs within the reactor and the kinetics of the reaction can be ascertained by examining the response of conversion rates to changes in input flow rates and concentrations or spatial concentration gradients in the case of a fixed bed reactor.

In reactors that do not have continuous input of Ox (such as a batch reactor), the fixed point attractor is the state where all species are in the reduced form and, therefore, kinetic information is contained only in the time series concentration data where the concentrations progress toward the steady-state. The kinetics equations for such a reactor design are often times simplified by assuming that some, but not all, of the species are in a pseudo-steady-state. The procedure for deriving these equations involve setting some of the time derivatives to zero and using these equations to derive algebraic relationships

between the concentrations of certain species which are then substituted into the remaining rate laws (whose derivatives were not set to zero). In some instances, some of the species in a reaction sequence are assumed to rapidly equilibrate with each other and that kinetics in one of the species induce proportional kinetics in the other species. This equilibrium assumption is a special case of the pseudo-steady-state assumption and we will denote it as the pseudo-equilibrium assumption.

We may explain the details of steady-state and pseudo-steady-state derivations and bring to light ideas to keep in mind when using thus derived by considering a simplified version of scheme 3 in both a plug flow reactor and a batch reactor.

$$Ox + S \underset{k_{des}}{\overset{k_{ads}}{\rightleftharpoons}} Ox{:}S \xrightarrow{k_{rxn}} Red + S \qquad \qquad \text{Scheme 3}$$

Where we have lumped the mass transport and sorption processes for Ox:S formation and neglected Red adsorption. In a plug flow reactor of cross-sectional area, A, and flow rate, Q, the kinetic equations for scheme 3 are as follows:

$$\frac{\partial[Ox]}{\partial t} = -\frac{Q}{A}\frac{\partial[Ox]}{\partial x} - k_{ads}[S][Ox] + k_{des}[Ox{:}S] \tag{72}$$

$$\frac{\partial[Ox{:}S]}{\partial t} = k_{ads}[S][Ox] - k_{des}[Ox{:}S] - k_{rxn}[Ox{:}S] \tag{73}$$

$$S_{Tot} = [S] + [Ox{:}S] \tag{74}$$

Setting all time derivatives to zero gives

$$\frac{d[Ox]}{dx} = \frac{A}{Q}\left(k_{ads}[S][Ox] - k_{des}[Ox{:}S]\right) \tag{75}$$

$$[Ox{:}S] = \frac{k_{ads}}{k_{des} + k_{rxn}}[S][Ox] \tag{76}$$

Substituting equation (76) into equation (75) and applying equation (74) gives

$$\frac{d[Ox]}{dx} = \frac{A}{Q}\left(k_{ads}[S][Ox] - k_{des}\frac{k_{ads}}{k_{des}+k_{rxn}}[S][Ox]\right) = -\frac{A}{Q}\frac{S_{Tot}k_{rxn}\dfrac{k_{ads}}{k_{des}+k_{rxn}}[Ox]}{1 + \dfrac{k_{ads}}{k_{des}+k_{rxn}}[Ox]} \tag{77}$$

Equation (77) is the Langmuir-Hinshelwood equation for scheme 3 as it applies to plug flow reactors. The solution to equation (77) is a fixed point solution to equations (72-74) and is asymptotically stable (i.e., solutions to equations 72-74 will approach equation 77 at large times).

In the case of abundant reaction sites, [S] can be taken as constant and equal to S_{Tot}. The steady-state solution for this case is the pseudo-first-order equation as follows

$$\frac{d[Ox]}{dx} = -\frac{A}{Q} S_{Tot} k_{rxn} \frac{k_{ads}}{k_{des} + k_{rxn}} [Ox]$$

(78)

In a batch reactor, the kinetic equations for scheme 3 are as follows

$$\frac{d[Ox]}{dt} = -k_{ads}[S][Ox] + k_{des}[Ox:S]$$

(79)

$$\frac{d[Ox:S]}{dt} = k_{ads}[S][Ox] - k_{des}[Ox:S] - k_{rxn}[Ox:S]$$

(80)

$$S_{Tot} = [S] + [Ox:S]$$

(81)

The fixed point attractor for equations (79-81) is [Ox] = [Ox:S] = 0 and, so, the kinetic equations for a batch reactor are typically simplified by setting either d[Ox:S]/dt = 0 (a pseudo-steady-state assumption) or d[Ox]/dt = 0 (a pseudo-equilibrium assumption). The pseudo-steady-state assumption gives the following

$$\frac{d[Ox]}{dt} = k_{ads}[S][Ox] - k_{des}\frac{k_{ads}}{k_{des} + k_{rxn}}[S][Ox] = -\frac{S_{Tot} k_{rxn} \frac{k_{ads}}{k_{des} + k_{rxn}}[Ox]}{1 + \frac{k_{ads}}{k_{des} + k_{rxn}}[Ox]}$$

(82)

Equation (82) is the Langmuir-Hinshelwood equation as applied to a batch reactor (note the similarities with equation 77). Solutions to Equation (82) are not, however, asymptotically stable and are not solutions to equations (79-81). Figure 2.8 shows the field of vectors (d[Ox], d[Ox:S]) in ([Ox], [Ox:S]) space. A solution to equations (79-81) passing through ([Ox]$_0$, [Ox:S]$_0$) can be visualized by starting at the initial point and following the arrows to the fixed point is reached. An asymptotically stable solution exists as those points that can not be reached from either [Ox:S]$_0$ = 0 or [Ox]$_0$ = 0. The

derivation of equation (82) involves setting d[Ox:S]/dt = 0 and, therefore, solutions to equation (82) pass through the horizontal arrows in Figure 2.8.

$$[Ox:S] = \frac{S_{Tot} \dfrac{k_{ads}}{k_{des} + k_{rxn}} [Ox]}{1 + \dfrac{k_{ads}}{k_{des} + k_{rxn}} [Ox]} \tag{83}$$

We can see from Figure 2.8 that any initial condition along equation (83) will not follow equation (83) but rather will approach the asymptotically stable solution described above.

Another form of the Langmuir-Hinshelwood equation can be obtained by assuming that the adsorption step of scheme 3 is in pseudo-equilibrium (i.e., setting d[Ox]/dt = 0) so that equation (79) and equation (81) give the following relationship between [Ox:S] and [Ox]

$$[Ox:S] = \frac{S_{Tot} \dfrac{k_{ads}}{k_{des}} [Ox]}{1 + \dfrac{k_{ads}}{k_{des}} [Ox]} \tag{84}$$

Equation (84) is the Langmuir isotherm and a kinetics expression for [Ox] is obtained by assuming that the overall rate of reaction (i.e., d[Ox]/dt) is equal to the rate of surface transformation (i.e., d[Ox:S]/dt) giving

$$\frac{d[Ox]}{dt} = -\frac{S_{Tot} k_{rxn} \dfrac{k_{ads}}{k_{des}} [Ox]}{1 + \dfrac{k_{ads}}{k_{des}} [Ox]} \tag{85}$$

As is the case for equation (82), solutions of equation (85) are neither asymptotically stable nor solutions to equations (79-81). Since equation (85) was derived by assuming d[Ox]/dt = 0, solutions to equation (85) lay along the curve in Figure 2.8 where the horizontal component of the vector field goes to zero (i.e., equation 84). Equation (84) bounds the asymptotically stable solution from above while equation (83) bounds the asymptotically stable solution from the bottom.

As [Ox] becomes small relative to S_{Tot}, equations (79-81) approach pseudo-first-order behavior which can be found by substituting [S] = S_{Tot} into equations (79-80)

$$\frac{d[Ox]}{dt} = -\hat{k}_{ads}[Ox] + k_{des}[Ox{:}S] \tag{86}$$

$$\frac{d[Ox{:}S]}{dt} = \hat{k}_{ads}[Ox] - k_{des}[Ox{:}S] - k_{rxn}[Ox{:}S] \tag{87}$$

Where $\hat{k}_{ads} = k_{ads}S_{Tot}$. Equations (86-87) comprise a linear homogeneous system of equations of second order. The solution to such a system is the sum of two exponential functions (provided that they are linearly independent) with eigenvalues

$$r_- = \frac{-\left(\hat{k}_{ads} + k_{des} + k_{rxn}\right) - \sqrt{\left(\hat{k}_{ads} + k_{des} + k_{rxn}\right)^2 - 4\hat{k}_{ads}k_{rxn}}}{2} \tag{88}$$

$$r_+ = \frac{-\left(\hat{k}_{ads} + k_{des} + k_{rxn}\right) + \sqrt{\left(\hat{k}_{ads} + k_{des} + k_{rxn}\right)^2 - 4\hat{k}_{ads}k_{rxn}}}{2} \tag{89}$$

Both eigenvalues are negative and r_-, which is larger in magnitude, corresponds to the transient portion of the kinetics (e.g., an initial drop in a bimodal kinetic profile), while r_+ corresponds to the pseudo-first-order portion of the kinetics (with $k_{obs} = r_+$).

2.6 Literature Cited

(1)   Matheson, L. J.; Tratnyek, P. G. Reductive Dehalogenation of Chlorinated Methanes by Iron Metal. *Environ. Sci. Technol.* 1994, *28*, 2045.

(2)   Burris, D. R.; Campbell, T. J.; Manoranjan, V. S. Sorption of Trichloroethylene and Tetrachloroethylene in a Batch Reactive Metallic Iron-Water System. *Environ. Sci. Technol.* 1995, *29*, 2850.

(3)   Johnson, T. L.; Scherer, M. M.; Tratnyek, P. G. Kinetics of Halogenated Organic Compound Degradation by Iron Metal. *Environ. Sci. Technol.* 1996, *30*, 2634.

(4)   Su, C.; Puls, R. W. Kinetics of Trichloroethene Reduction by Zerovalent Iron and Tin: Pretreatment Effect, Apparent Activation Energy, and Intermediate Products. *Environ. Sci. Technol.* 1999, *33*, 163.

(5)   Butler, E. C.; Hayes, K. F. Factors Influencing Rates and Products in the Transformation of Trichloroethylene by Iron Sulfide and Iron Metal. *Environ. Sci. Technol.* 2001, *35*, 3884.

(6)   Temkin, M. I. The Kinetics of Some Industrial Heterogeneous Catalytic Reactions. *Adv. Catal.* 1979, *28*, 173.

(7)   Wüst, W. F.; Köber, R.; Schlicker, O.; Dahmke, A. Combined Zero- and First-Order Kinetic Model of the Degradation of TCE and Cis-DCE with Commercial Iron. *Environ. Sci. Technol.* 1999, *33*, 4304.

(8)   Miehr, R.; Tratnyek, P. G.; Bandstra, J. Z.; Scherer, M. M.; Alowitz, M.; Bylaska, E. J. The Diversity of Contaminant Reduction Reactions by Zero-Valent Iron: Role of the Reductate. *Environ. Sci. Technol.* 2004, *38*, 139.

(9)   Arnold, W. A.; Roberts, A. L. Inter- and Intraspecies Competitive Effects in Reactions of Chlorinated Ethylenes with Zero-Valent Iron in Column Reactors. *Environ. Eng. Sci.* 2000, *17*, 291.

(10)   Arnold, W. A.; Roberts, A. L. Pathways and Kinetics of Chlorinated Ethylene and Chlorinated Acetylene Reaction with Fe(0) Particles. *Environ. Sci. Technol.* 2000, *34*, 1794.

(11)   Johnson, T. L.; Fish, W.; Gorby, Y. A.; Tratnyek, P. G. Degradation of Carbon Tetrachloride by Iron Metal: Complexation Effects on the Oxide Surface. *J. Contam. Hydrol.* 1998, *29*, 377.

(12)   Agrawal, A.; Ferguson, W. J.; Gardner, B. O.; Christ, J. A.; Bandstra, J. Z.; Tratnyek, P. G. Effects of Carbonate Species on the Kinetics of 1,1,1-Trichloroethane by Zero-Valent Iron. *Environ. Sci. Technol.* 2002, *36*, 4326.

(13)   Scherer, M. M.; Balko, B. A.; Tratnyek, P. G. The Role of Oxides in Reduction Reactions at the Metal-Water Interface. In *Mineral-Water Interfacial Reactions: Kinetics and Mechanisms* ; Sparks, D. L., Grundl, T. J., Eds.; American Chemical Society: Washington, DC, 1998; Vol. ACS Symp. Ser. 715; pp 301.

Kinetic equations	Differential equations for batch	Fitting equations
First-Order disappearance	$\dfrac{d[\text{Ox}]}{dt} = -k_{MT}^{\text{Ox}}\rho_a[\text{Ox}]$	$[\text{Ox}] = [\text{Ox}]_0 \exp\left(-k_{MT}^{\text{Ox}}\rho_a t\right)$
Langmuir-Hinshelwood disappearance without product inhibition	$\dfrac{d[\text{Ox}]}{dt} = -\dfrac{S_{Tot}k_{rxn}K_{LH}^{\text{Ox}}[\text{Ox}]}{1+K_{LH}^{\text{Ox}}[\text{Ox}]}$	$\ln([\text{Ox}]) + K_{LH}^{\text{Ox}}[\text{Ox}] = -S_{Tot}k_{rxn}K_{LH}^{\text{Ox}}t$ $\qquad\qquad + \ln([\text{Ox}]_0) + K_{LH}^{\text{Ox}}[\text{Ox}]_0$
Langmuir-Hinshelwood disappearance with product inhibition	$\dfrac{d[\text{Ox}]}{dt} = -\dfrac{k\rho_a K_{\text{Ox}}[\text{Ox}]}{1+K_{\text{Ox}}[\text{Ox}]+K_{\text{Red}}[\text{Red}]}$	Compute numerically
Bimodal disappearance	$\dfrac{d[\text{Ox}]}{dt} = -k_{MT/ads}^{\text{Ox}}[\text{Ox}]+k_{MT/des}^{\text{Ox}}[\text{Ox:S}]$ $\dfrac{d[\text{Ox:S}]}{dt} = k_{MT/ads}^{\text{Ox}}[\text{Ox}]-k_{MT/des}^{\text{Ox}}[\text{Ox:S}]$ $\qquad -k_{rxn}[\text{Ox:S}]$	$[\text{Ox}] = \alpha_+ \exp(r_+ t) + \alpha_- \exp(r_- t)$

Table 2.1. Summary of rate laws that are useful in the treatment of kinetic data.
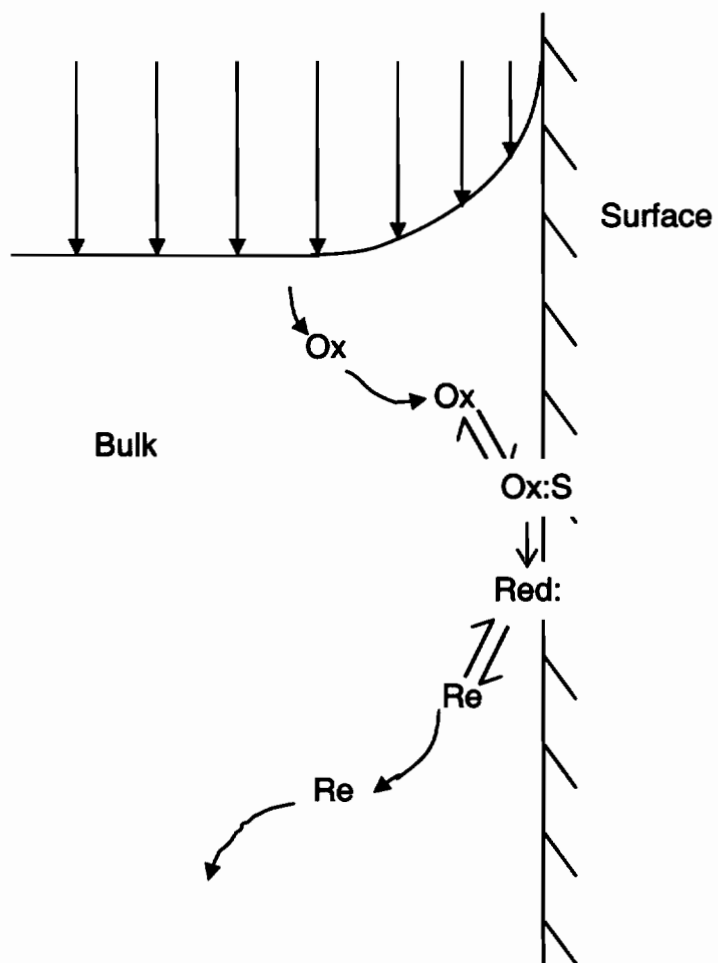
Figure 2.1.   Processes involved in an interfacial reaction.
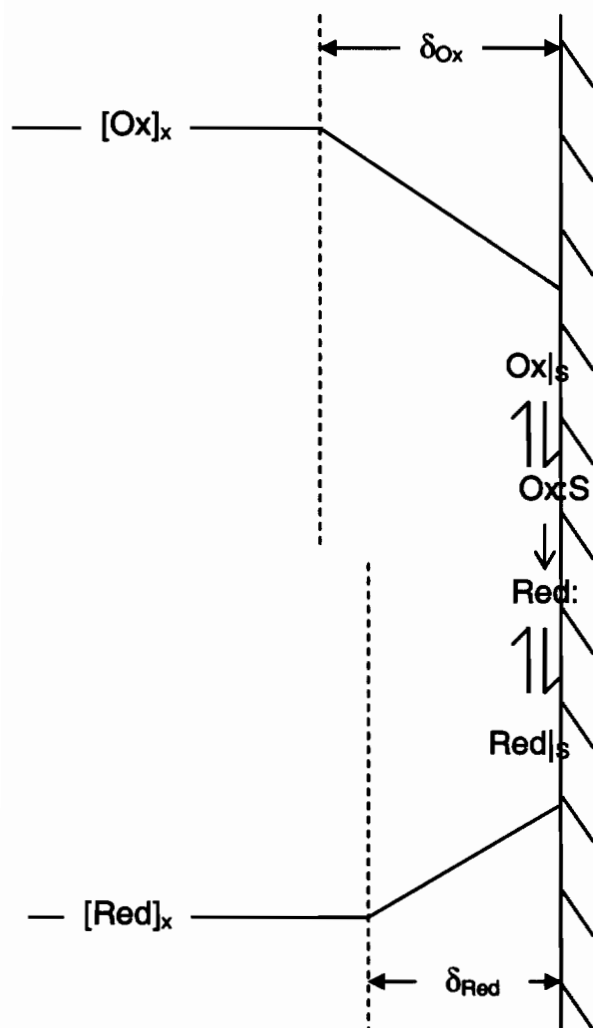
Figure 2.2.   Simplified interfacial reaction scheme with a well mixed bulk solution and a diffusive boundary layer.
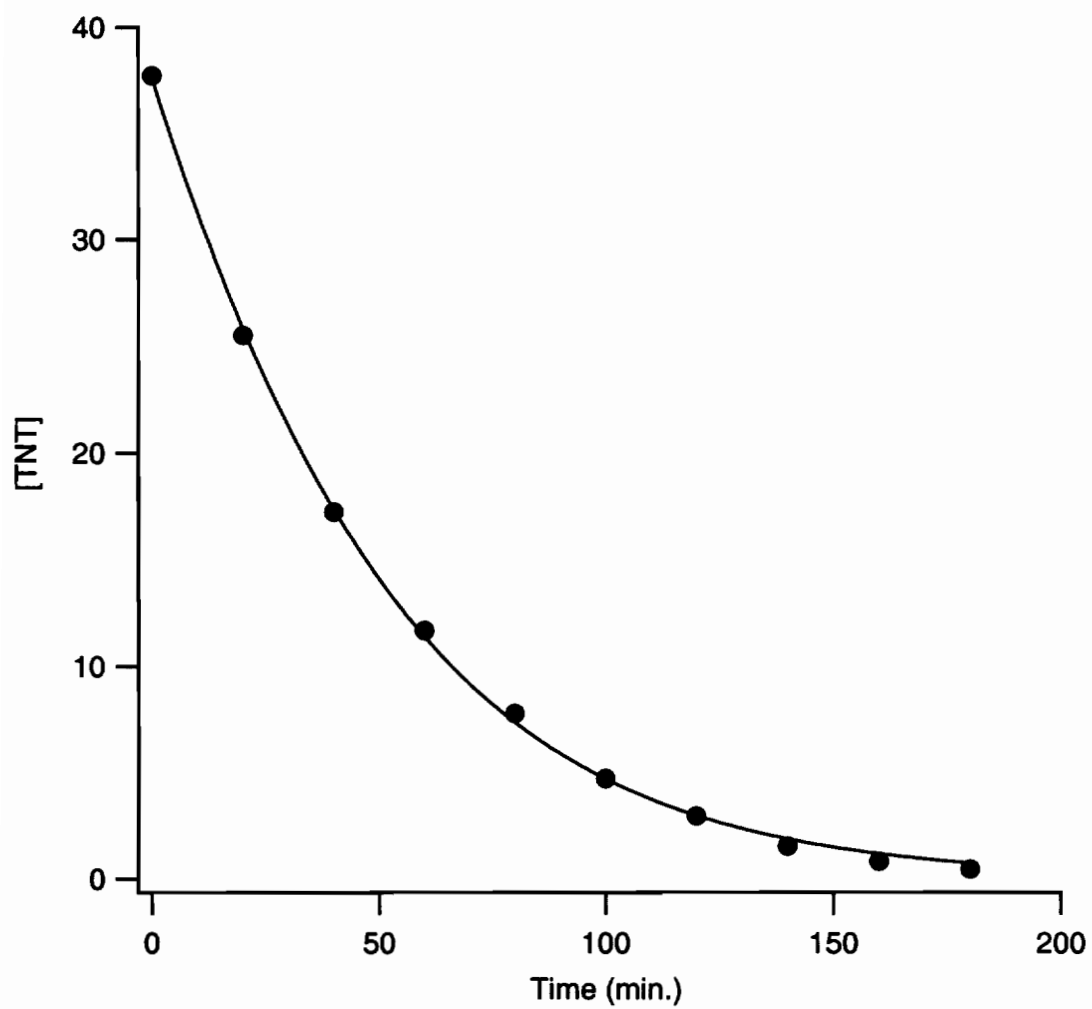
Figure 2.3.   First-order disappearance of TNT on Fisher electrolytic granular iron metal.
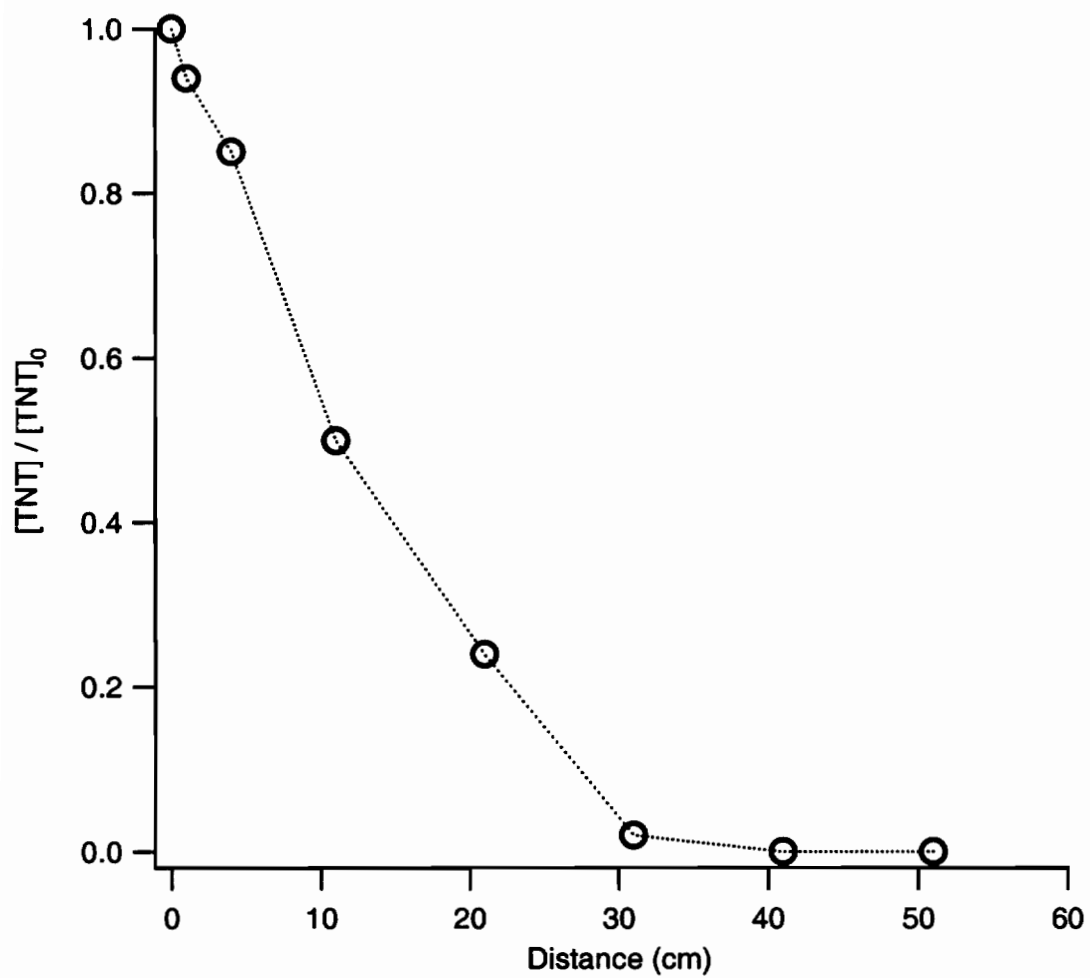
Figure 2.4.   TNT disappearance along the length of a column filled with granular iron metal.
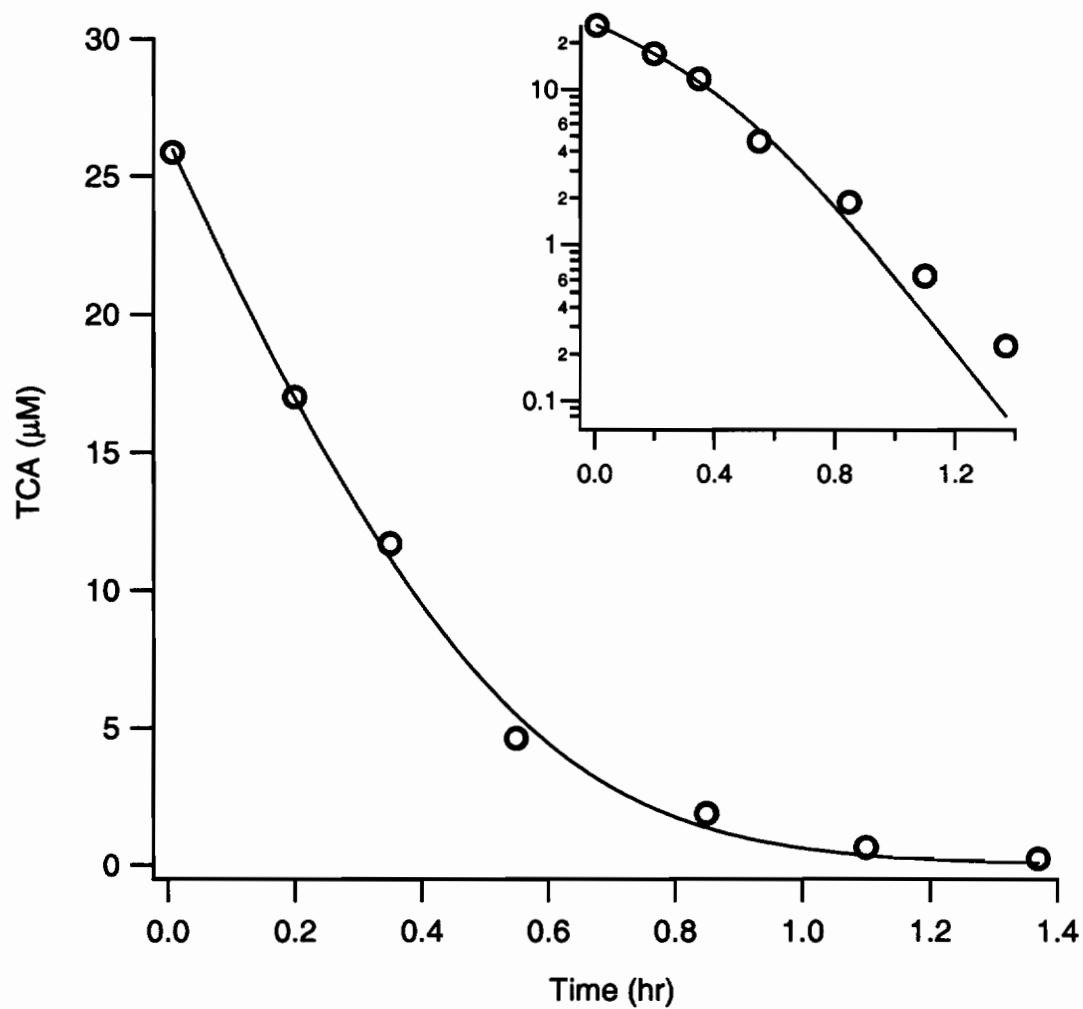
Figure 2.5. Mixed order disappearance of TCA on granular iron metal pre-exposed to a carbonate solution.
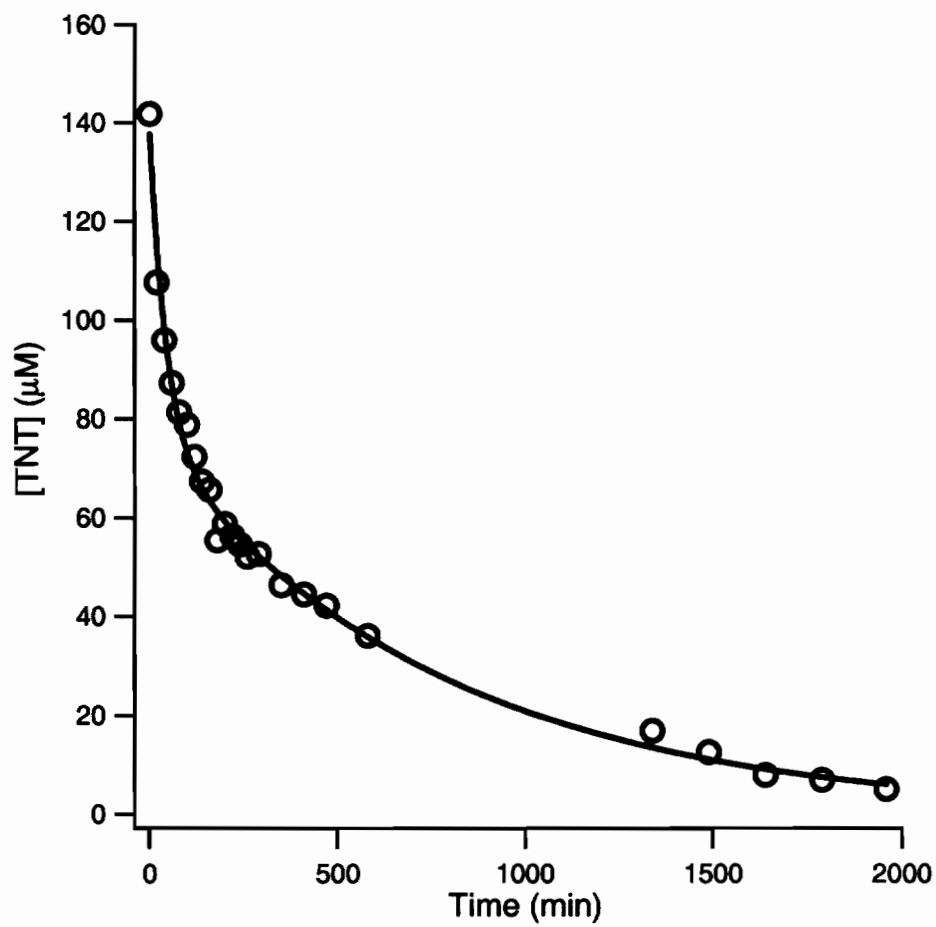
Figure 2.6.   Bimodal TNT disappearance on 0.75 g peerless iron / 60 mL.
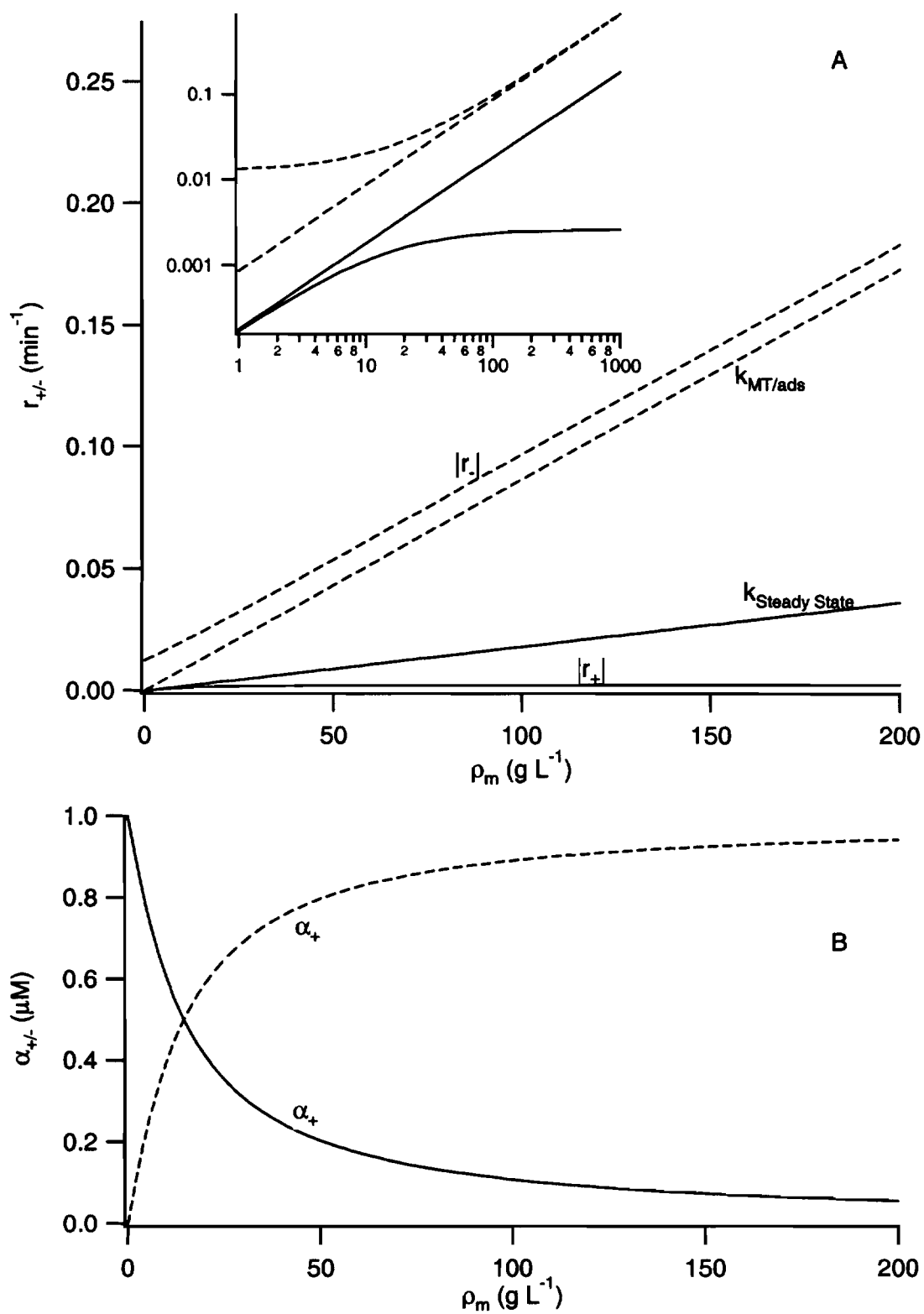
Figure 2.7.   Eigenvalues (A) and eigenvector terms (B) plotted against iron loading.
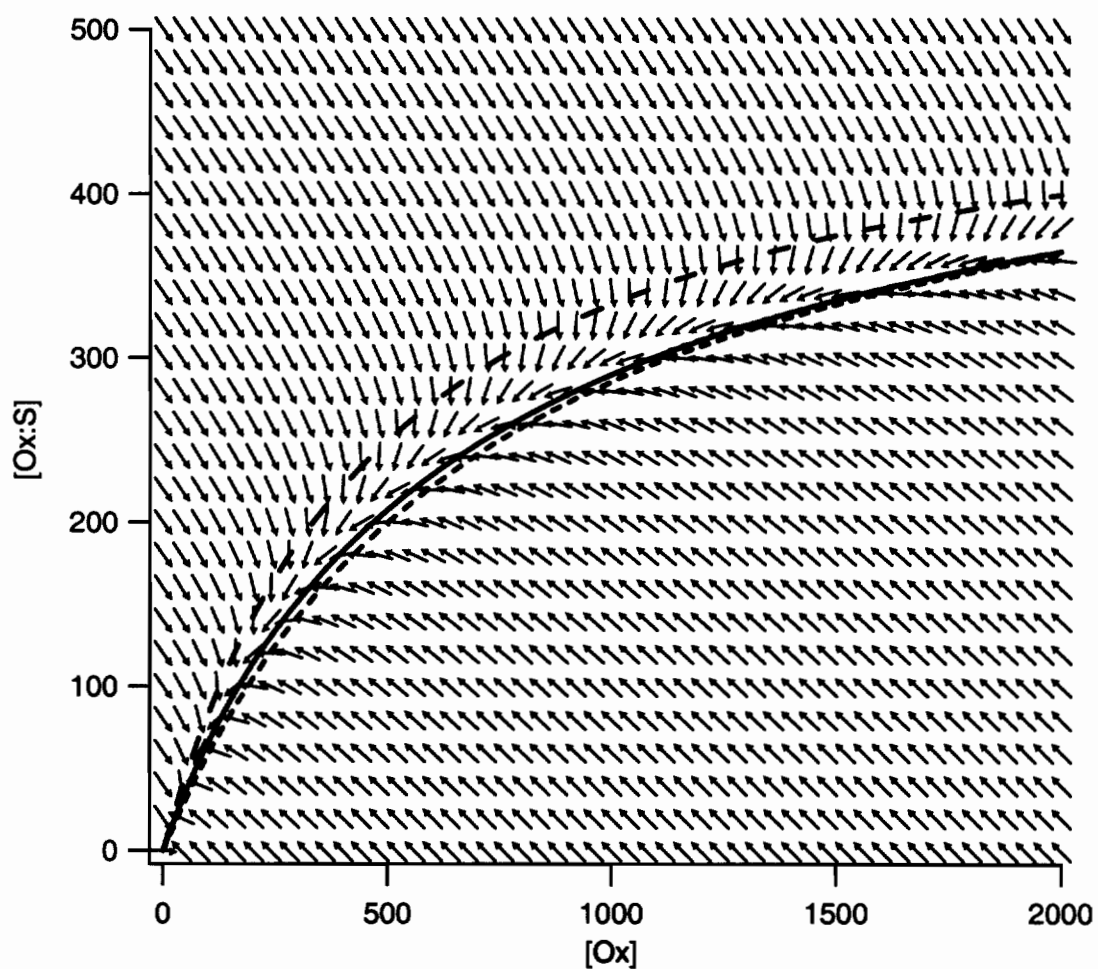
Figure 2.8.   Vector field for the non-steady-state analogue to Langmuir-Hinshelwood

kinetics. The long dashed line is the pseudo-equilibrium derived

Langmuir-Hinshelwood equation, the short dashed line is the pseudo-

steady-state derived Langmuir-Hinshelwood equation, and the solid line is

the path of the Lyapunov vector.
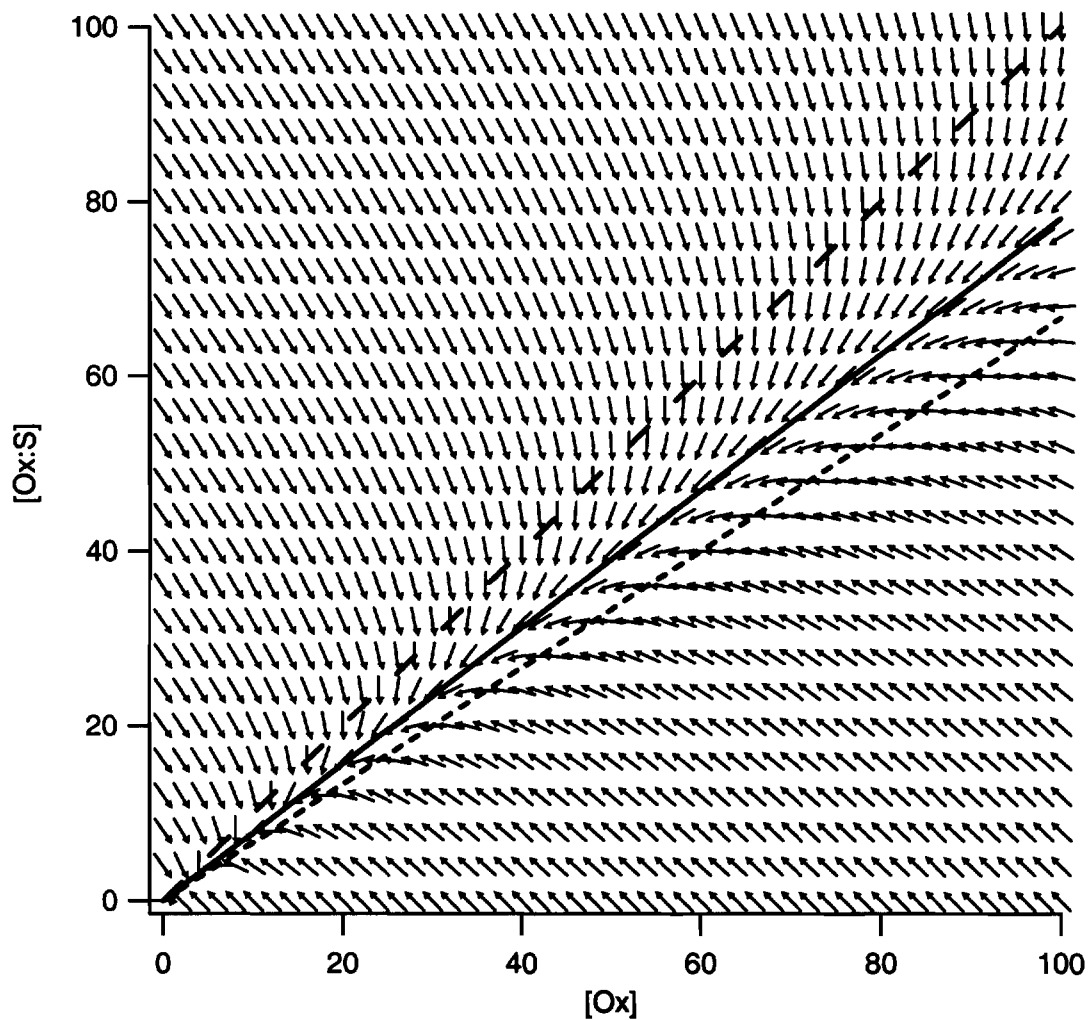
Figure 2.9.   Vector field for the non-steady-state analogue to pseudo-first-order

kinetics. The long dashed line is the pseudo-equilibrium derived first-order

equation, the short dashed line is the pseudo-steady-state derived first-

order equation, and the solid line is the path of the small eigenvector (r_+).

CHAPTER 3

Central Limit Theorem for Chemical Kinetics in Complex Systems[1]

3.1 Abstract

The prevalence of apparently first-order kinetics of reactant disappearance in complex systems with many possible reaction pathways is usually attributed to the dominance of a single rate limiting step. Here, we investigate another possible explanation: that apparently first-order kinetics might arise because the aggregate behavior of many processes, with varying order of reaction and rate constant, approaches a "central limit" that is indistinguishable from first-order behavior. This hypothesis was investigated by simulating systems of increasing complexity and deriving relationships between the apparent reaction order of such systems and various measures of their complexity. Transformation of a chemical species by parallel irreversible reactions that are zero, first, or second order is found to converge to a central limit as the number of parallel reactions becomes large. When all three reaction orders are represented, on average, in equal proportions, this central limit is experimentally indistinguishable from first-order. A measure of apparent reaction order was used to investigate the nature of the convergence both stochastically and by deriving theoretical limits. The range of systems that exhibit a central limit that is approximately first-order is found to be broad. First-order like behavior is also found to be favored when the distribution of material among the parallel processes (due to differences in rate constants for the individual reactions) is more complex. Our results show that a first-order central limit exists for the kinetics of chemical systems and that the variable controlling the convergence is the physical complexity of reaction systems.

---

[1] Bandstra J.Z. and P.G. Tratnyek. 2005. *Journal of Mathematical Chemistry*. In Press.

41

3.2 Introduction

A first-order rate equation is often used to model the chemical kinetics of reactions that involve complex pathways and multiple mechanisms. The results of such modeling are often quite satisfactory even though theoretical considerations would suggest a more complicated rate law. Common explanations of this phenomenon include: (*i*) the first order model is applied over a small extent of reaction, in which case, many rate laws will adequately describe the data, (*ii*) the data contain noise causing any fine structure to be obscured and deviation from the first-order model to be attributed to random measurement errors rather than model failure, and (*iii*) the observed kinetics reflect a rate limiting step that is first-order. It is the purpose of this work to investigate another possible explanation: that multiple processes (which are not necessarily first-order) may combine to produce kinetic behavior that is indistinguishable from first-order and that such combinations are more likely to exist when reactions occur in a complex environment.

This hypothesis may be viewed as a chemical kinetics analog to the central limit theorem of statistics. The central limit theorem states that, when scaled properly, a linear combination of random variables approaches a normal distribution as the number of random variables becomes large [1]. Some familiar implications of the central limit theorem include (*i*) the justification for assuming that most measurement errors are normally distributed and (*ii*) the result that sufficiently large stochastic systems obey a Fokker-Planck equation [2] and, in the case of chemical kinetics, a reaction rate equation [3]. Our hypothesis, then, is that there is also a central limit effect in the reaction order of chemical kinetics where the central limit is first-order behavior and the controlling variable is system complexity.

In a general sense, it seems that the notion of this central limit effect is widely held, but we have found no evidence that it has been systematically investigated. Our interest in the hypothesis arose from consideration of contaminant degradation kinetics in complex environmental media such as soils and sediments, but we expect that this investigation will have relevance in other contexts such as chemical engineering of

bioreactors, catalysis on heterogeneous surfaces, radical reactions in plasmas and flames, atmospheric chemistry, etc.

3.3 Methods

We have investigated the nature and validity of our conjecture by examining a range of specific kinetic systems for the type of behavior hypothesized. This approach involves four elements: (*i*) generation of a variety of rate laws, (*ii*) solution of the rate laws, (*iii*) assessment of the degree of complexity of the corresponding reaction system, and (*iv*) assessment of the apparent order of the resulting disappearance curve.

3.3.1 Generation of Rate Laws

We selected parallel irreversible reactions as our test case because it is the simplest possible system that contains the features employed in formulating our conjecture. Considering the simplest case allows us to clearly explain the details of the conjecture and allows us to easily develop the necessary analyses and interpret the results. We generated rate laws for an arbitrary number of parallel irreversible reactions in the form:

$$\frac{dA}{dt} = -\sum_{i=1}^{N_{rxns}} k_i \cdot A^{m_i}$$

(1)

With the initial condition:

$$A(0) = A_0$$

(2)

Where A denotes concentration (or activity) of the reacting chemical species, N_{rxns} denotes the number of parallel reactions, k_i denotes the rate constant for the ith reaction, and m_i denotes the reaction order for the ith reaction.

A variety of rate laws may be obtained from eq 1 by employing various selection criteria for N_{rxns}, the values of k_i, and the values of m_i. We expect complexity of the system to increase with N_{rxns}, so we varied N_{rxns} from 1 to 50. We would like to interpret each reaction as an elementary reaction step, so we required that the value of each m_i be 0, 1, or 2 under the presumption that third-order and higher-order reaction steps are prohibitively unlikely. We selected the values of m_i stochastically when we wished to examine an ensemble of like reaction systems and combinatorially when we wished to

examine all possible combinations of reaction orders for a given N_{rxns}. $P(m_i = x)$ denotes the probability that $m_i = x$ and n_x denotes the number of reactions with $m_i = x$. Note that $P(m_i = 0) + P(m_i = 1) + P(m_i = 2) = 1$ and $n_0 + n_1 + n_2 = N_{rxns}$.

We selected rate constants by first selecting a characteristic value, ξ_i, and then scaling ξ_i according to:

$$k_i = \begin{cases} \xi_i \cdot \dfrac{1}{N_{rxns} \cdot \langle \xi \rangle} \cdot A_0 \cdot \dfrac{7}{8 \cdot \ln(8)} & m_i = 0 \\[2ex] \xi_i \cdot \dfrac{1}{N_{rxns} \cdot \langle \xi \rangle} & m_i = 1 \\[2ex] \xi_i \cdot \dfrac{1}{N_{rxns} \cdot \langle \xi \rangle} \cdot \dfrac{1}{A_0} \cdot \dfrac{7}{\ln(8)} & m_i = 2 \end{cases} \tag{3}$$

Where $\langle \xi \rangle$ denotes the average value of the distribution from which each ξ_i is selected. Equation 3 contains three scaling factors: $1/(N_{rxns} \cdot \langle \xi \rangle)$, $A_0^{(1-m_i)}$, and a third reaction order dependent factor. The scaling factor, $1/(N_{rxns} \cdot \langle \xi \rangle)$, makes eq 1 independent of N_{rxns} and $\langle \xi \rangle$. This scaling is equivalent to scaling time by $N_{rxns} \cdot \langle \xi \rangle$. The scaling factor, $A_0^{(1-m_i)}$ (equals 1 for $m_i = 1$), causes A/A_0 to be independent of A_0.

Rate constants for processes of different reaction order are dimensionally inconsistent and, therefore, cannot be compared directly. The third scaling factor is needed to force reactions to contribute to the overall system development in proportion to their value of ξ_i, regardless of reaction order. We derived the values for this factor by requiring a zero-order only system and a second-order only system to proceed to an arbitrary concentration endpoint in the same amount of time as a first-order only system. The endpoint used was three half-lives, the selection of which is discussed later. In the case of stochastic selection of reaction orders, the ξ_i for each reaction was selected randomly from a normal distribution which was truncated at zero. In the case of combinatorial selection of reaction orders, all ξ_i's were set equal to $\langle \xi \rangle$.

The manner of rate constant generation described above gives rise to groups of reaction systems with the same value of N_{rxns}, m_i selection criteria, and ξ_i selection criteria. In the discussion that follows, we will call these groups ensembles of like

reaction systems. An ensemble member, then, is an individual reaction system and the ensemble size is the number of reaction systems belonging to a particular ensemble.

3.3.2 Solutions to the Rate Laws

Given the restrictions placed on m_i, an analytical solution to eq 1 may be obtained by direct integration. To aid integration, we re-write eq 1 as:

$$\frac{dA}{dt} = -a \cdot A^2 - b \cdot A - c \tag{4}$$

where:

$$a = \sum_{\{i|m_i=2\}} k_i \tag{5}$$

$$b = \sum_{\{i|m_i=1\}} k_i \tag{6}$$

$$c = \sum_{\{i|m_i=0\}} k_i \tag{7}$$

Integration and application of the initial condition (eq 2) yields:

$$A = \begin{cases} -\dfrac{b}{2\cdot a} + \dfrac{\sqrt{b^2-4\cdot a\cdot c}}{2\cdot a} \cdot \dfrac{\dfrac{\sqrt{b^2-4\cdot a\cdot c}+(b+2\cdot a\cdot A_0)}{\sqrt{b^2-4\cdot a\cdot c}-(b+2\cdot a\cdot A_0)}\cdot e^{\sqrt{b^2-4\cdot a\cdot c}\cdot t}-1}{\dfrac{\sqrt{b^2-4\cdot a\cdot c}+(b+2\cdot a\cdot A_0)}{\sqrt{b^2-4\cdot a\cdot c}-(b+2\cdot a\cdot A_0)}\cdot e^{\sqrt{b^2-4\cdot a\cdot c}\cdot t}+1} & t < t_{A=0} \\[4em] 0 & t \geq t_{A=0} \end{cases} \tag{8}$$

This solution, while general, contains a number of cases that result in singularities when calculating disappearance curves. In these cases the calculations were simplified by taking limits and/or employing Euler's formula. For example, if $a = c = 0$, then eq 8 takes on an indeterminate form and must be calculated by taking the limit (using L' Hospital's rule) as a and c approach zero. The resulting equation, in this case, is the solution to a first-order rate law with rate constant equal to b.

3.3.3 Quantification of Complexity

In selecting an approach to quantify complexity, we considered two generally accepted features of complex systems: (i) complex systems are comprised of many

interrelated parts, and (ii) complex systems exhibit both ordered and random behavior [4-8]. A number of complexity metrics have been proposed [7,9-13], but application of these metrics to specific systems can be nontrivial and the interpretation of these metrics is still an area of research. Our preliminary efforts using the Shiner metric [13] produced results consistent with the findings reported below. However, we found that two lower level quantities, the number of reactions, $N_{rxns,}$ and the pathway entropy (defined later), gave comparable results for the systems considered here. These surrogate complexity metrics proved to be preferable for present purposes due to ease of implementation and interpretation.

Complex systems are comprised of many interrelated parts. For the systems that we have considered, N_{rxns} is the relevant measure of the number of parts. Because we are not changing the way in which the reactions are related, it is intuitive to use N_{rxns} as a measure of complexity. This is consistent with the Shiner metric, which we found to be dominated by $\ln(N_{rxns})$ for the systems considered.

In addition to examining the effect of N_{rxns}, we also want to compare reaction systems with the same N_{rxns}. Early work in information theory by Shannon [14] led to widespread use of information or Shannon entropy as a measure of complexity:

$$S = -\sum_i P_i \cdot \ln(P_i) \tag{9}$$

where S is a measure of the degree of randomness for the probability distribution, P. Because complex systems are neither completely ordered nor completely random, it has been recognized that the relationship between Shannon entropy and complexity includes a maximum at an intermediate entropy value [6,11,15].

For the purposes of this study, a Shannon entropy pertaining to chemical transformation may be calculated from the set of probabilities describing the likelihood that a randomly selected molecule will undergo a particular transformation, or follow a particular pathway, during the course of reaction. These pathway probabilities were calculated, as shown in eqs 10-12, by dividing the limit of the concentration of the ith product as time approaches infinity by the total amount of material in the system (A_0).

$$P_i = \frac{k_i}{A_0 \cdot \sqrt{b^2 - 4 \cdot a \cdot c}} \cdot \ln\left(\frac{A_0 \cdot b + 2 \cdot c + A_0 \cdot \sqrt{b^2 - 4 \cdot a \cdot c}}{A_0 \cdot b + 2 \cdot c - A_0 \cdot \sqrt{b^2 - 4 \cdot a \cdot c}}\right) \qquad m_i = 0 \tag{10}$$

$$P_i = \frac{k_i}{A_0 \cdot 2 \cdot a} \left[\ln\left(\frac{A_0 \cdot b + c + A_0^2 \cdot a}{c} \right) - \frac{b}{\sqrt{b^2 - 4 \cdot a \cdot c}} \cdot \ln\left(\frac{A_0 \cdot b + 2 \cdot c + A_0 \cdot \sqrt{b^2 - 4 \cdot a \cdot c}}{A_0 \cdot b + 2 \cdot c - A_0 \cdot \sqrt{b^2 - 4 \cdot a \cdot c}} \right) \right] \qquad m_i = 1 \qquad (11)$$

$$P_i = \frac{k_i}{A_0 \cdot 2 \cdot a^2} \left[A_0 \cdot 2 \cdot a - b \cdot \ln\left(\frac{A_0 \cdot b + c + A_0^2 \cdot a}{c} \right) + \frac{b^2 - 2 \cdot a \cdot c}{\sqrt{b^2 - 4 \cdot a \cdot c}} \cdot \ln\left(\frac{A_0 \cdot b + 2 \cdot c + A_0 \cdot \sqrt{b^2 - 4 \cdot a \cdot c}}{A_0 \cdot b + 2 \cdot c - A_0 \cdot \sqrt{b^2 - 4 \cdot a \cdot c}} \right) \right] \qquad m_i = 2 \qquad (12)$$

Application of eq 9 to the pathway probabilities (eqs 10-12) yields a pathway entropy that we denote as S_{pthwy}. For a fixed N_{rxns}, S_{pthwy} is a measure of the uniformity in the pathway probability distribution. A perfectly uniform pathway probability distribution yields the maximum S_{pthwy}, $\ln(N_{rxns})$. A distribution in which a pathway probability, P_i, equals one (and all others equal zero) yields $S_{pthwy} = 0$. In all cases considered here, S_{pthwy} is close to the maximum value, $\ln(N_{rxns})$, causing the relationship between complexity and S_{pthwy} to be approximately linear with negative slope. Since we are concerned only with relative complexity, we may use S_{pthwy} as our measure, noting that reaction systems with larger S_{pthwy} values are less complex.

3.3.4 Metric for Apparent Order of Reaction

Many procedures have been described for determination of the apparent order of a reaction from experimental data, and their relative strengths and weaknesses are frequently discussed in textbooks of chemical kinetics. The most intuitive and widely-used approach involves plotting transformed time series data and examining the plot for linearity. In this study, we start by using this approach to provide a qualitative but direct indication of reaction order. Since we are interested in examining for behavior that appears to be first-order, we used logarithmically transformed concentration versus time plots.

It also proved useful to have a quantitative measure of apparent order. To this end, we fit the solution to eq 13 to simulated data generated by evaluating eq 8 at 1000

time points, evenly spaced between $t = 0$ and the time required to reach the three half-lives concentration.

$$\frac{dA}{dt} = -k \cdot A^M \qquad (13)$$

Fitting was performed by Chi-square minimization using the Levenberg-Marquardt method [16] with both k and M as fitting parameters. M, then, is a quantitative measure of apparent reaction order.

We used three half-lives as the endpoint for these calculations, as well as for the normalization of rate constants (see above). This value was chosen to provide enough extent of reaction to reveal deviations from first order behavior on a log concentration versus time plot [17] while preserving enough resolution of the initial rate behavior to be consistent with the way many experimental protocols are performed.

3.4 Results

3.4.1 Convergence with increasing N_{rxns}

Ensembles of 50 similar rate laws were generated for $N_{rxns} = 1, 5, 20,$ and 50 with a uniform distribution on the reaction order ($P(m_i = 0) = P(m_i = 1) = P(m_i = 2) = 1/3$) and a normal distribution ($\mu = 1, \sigma = 0.3$) on the raw rate parameter, ξ. The resulting disappearance behavior is depicted in Figure 3.1 on a semi-log concentration versus time plot. Recall that (in this type of plot) purely second-order behavior is a curve with positive concavity, purely first-order behavior is a straight line, and purely zero-order behavior is a curve with negative concavity.

The $N_{rxns} = 1$ ensemble (Figure 3.1 A) exhibits all three integer-order possibilities in approximately equal proportions. With increasing N_{rxns} (Figures 3.1 B- 3.1 D), the likelihood of integer order behavior becomes smaller and the ensemble members tend toward a limiting case (indicated by the dashed line in Figure 3.1) that is close to first-order. Behavior that appears to be first-order is possible for any N_{rxns} while behavior that appears zero-order or second-order becomes increasingly improbable as N_{rxns} increases.

The limiting case, shown as a dashed line in Figure 3.1, is described by a rate law of the form of eq 4. As N_{rxns} becomes large, eqs 5-7 become infinite series which converge to the following:

$$a_{\text{lim}} = \lim_{N_{rxns} \to \infty} a = P(m_i = 2) \cdot \frac{1}{A_0} \cdot \frac{7}{\ln(8)} \tag{14}$$

$$b_{\text{lim}} = \lim_{N_{rxns} \to \infty} b = P(m_i = 1) \tag{15}$$

$$c_{\text{lim}} = \lim_{N_{rxns} \to \infty} c = P(m_i = 0) \cdot A_0 \cdot \frac{7}{8 \cdot \ln(8)} \tag{16}$$

On a semi-log plot, the limit exhibits a slight "S" shape; concave up a high concentrations and concave down at low concentrations. The reason for this curvature and its magnitude will be examined later.

The behavior exhibited in Figure 3.1 may be further examined by plotting the apparent reaction order, M, (as defined by eq 13) against N_{rxns}. This is shown in Figure 3.2 for ensembles of reactions generated in the same manner as those shown in Figure 3.1 but with the ensemble size increased to 100. Each point represents a particular M for a member of an ensemble with the number of reactions indicated on the abscissa. As is the case for $N_{rxns} = 1$, some points may lie exactly on top of each other even if the corresponding disappearance curves do not. The average order and the average +/- one standard deviation for each N_{rxns} are plotted as solid lines. As N_{rxns} increases, the average order approaches a limiting value and the standard deviation approaches zero. Although the limiting apparent order (= 1.19) is somewhat greater than one, a first-order model may be fit to such a limiting disappearance curve. We calculated the average value of the absolute residuals for such a fit to be $0.01 \cdot A_0$ concentration units. This is smaller than the random errors in most experimental studies.

To verify the interpretation given to Figure 3.2, we can remove the distribution on ζ and examine every possible combination of reaction orders for a given N_{rxns}. A combination of reaction orders is defined by the sequence, (n_0, n_1, n_2), where n_x is the number of parallel reactions of order x. All possible combinations corresponding to a single N_{rxns} may be found by taking all permutations of (n_0, n_1, n_2) under the condition $n_0 + n_1 + n_2 = N_{rxns}$. The number of permutations is given by the combinatorial expression.

$$C^R(3, N_{Rxns}) = \frac{(1 + N_{Rxns}) \cdot (2 + N_{Rxns})}{2} \tag{17}$$

Here, all permutations are not equally probable. The weighting of (n_0, n_1, n_2) is given by

$$P(n_0, n_1, n_2) = \left[P(m_i = 0)\right]^{n_0} \cdot \left[P(m_i = 1)\right]^{n_1} \cdot \left[P(m_i = 2)\right]^{n_2} \cdot \frac{N_{rxns}!}{n_0! \cdot n_1! \cdot n_2!} \tag{18}$$

Figure 3.3 shows the results of this analysis, in the same format as Figure 3.2 (M vs. N_{rxns}). Larger points reflect greater relative weight (as defined by eq 18). As N_{rxns} increases, the number of permutations increases and the probability density becomes increasingly localized in the region of the limiting order. As N_{rxns} approaches infinity, the number of permutations approaches infinity and the sum of the weights for permutations with apparent order equal to 1.19 (the limiting order) approaches one. The average apparent order and the average +/- one standard deviation curves plotted in Figure 3.3 represent the theoretical limit (as the ensemble size approaches infinity) of the behavior that is approximated in Figure 3.2.

3.4.2 Behavior of the limiting case

Equations 14-16 and 18 indicate that the limiting apparent order (dashed line in Figures 3.2 and 3.3) is a function of the reaction order probability distribution. We have represented this functional dependence in Figure 3.4 by plotting contours of constant limiting apparent order in the space of zero-order and second-order probabilities. In this figure, the first-order probability is implied by the values of the zero-order and second-order probabilities. Each corner of the triangle represents a case where all reactions have the same order. The center of the triangle (indicated by an "x") is the case that we considered in Figures 3.1-3.3. We note that the area between the contours for $M = 0.8$ and $M = 1.2$ is much larger than either of the areas above the $M = 1.8$ contour or below the $M = 0.2$ contour. This shows that many reaction order distributions will ultimately yield apparent behavior that is near to first-order.

The fitting routine used to generate Figure 3.4 produces fits with chi-square equal to zero only for the reaction systems represented by the corners of Figure 3.4. This is due to the tendency of the log-transformed disappearance curves to exhibit an "S" shape as noted in the discussion of Figure 3.1. The contribution to the concavity of the log-transformed disappearance curve due to second-order processes is positive and increases with concentration. First-order processes do not contribute to the concavity of the log-transformed disappearance curve and zero-order contributions are negative and increases

with concentration (decreases in magnitude). As a result, the concavity of the log-transformed limiting case is initially dominated by second-order reactions and, therefore, positive, but finally dominated by zero-order reactions and, therefore, negative.

The log-transformed concavity is most pronounced when few of the processes are first-order (i.e. the $P(m_i = 0) + P(m_i = 2) = 1$ line in Figure 3.4). For the worst case along the $M = 1$ contour, the average of the absolute residuals between the limiting disappearance curve and the first-order fit is equal to $0.002 \cdot A_0$ concentration units. This value is significantly smaller that the error in a typical chemical kinetics experiment. Analysis of other cases along the $M = 1$ contour (not shown) indicates that this value decreases to zero at $P(m_i = 1) = 1$ slightly slower than linearly.

3.4.3 Convergence with decreasing S_{pthwy}

In the preceding discussion we have treated N_{rxns} as the variable controlling the tendency toward a central limit. It may also be instructive to look for centralizing tendencies within an ensemble of fixed N_{rxns}. To this end, we have calculated S_{pthwy} according to eqs 9-12 for each member of an $N_{rxns} = 5$ ensemble generated in the same manner as those depicted in Figures 3.1 and 3.2, but with the ensemble size increased to 10,000. Figure 3.5 shows the results of this calculation plotted against the apparent order, M. It is visually apparent from the distribution of the clusters of points that the average pathway entropy of ensemble members at or near the limiting order (for these conditions, 1.19) is larger than S_{pthwy} for the ensemble members on either side. This observation is reinforced by the maximum in the arithmetic mean of S_{pthwy} (represented in Figure 3.5 by the white line), which was calculated for the ranges of order indicated with vertical dashed lines in the figure.

The ensemble members with an approximately equal number of each reaction type tend to yield apparent order close to one. Such ensemble members also have, on average, smaller pathway entropy. This is because, when multiple reaction types are present, the pathways with lower reaction order tend to convert the most material over the full course of the reaction, yielding a less ordered distribution of material amongst the individual reactions. Somewhat less ordered pathway probability distributions may arise for any combination of reaction orders (due to the influence of distributed rate constants),

but this is more likely for systems with an equal number of each reaction type (due to the additional influence of distributed reaction orders). As complexity increases, therefore, the likelihood that a system will exhibit first-order behavior also increases even if the system does not have a large N_{rxns}. Convergence toward a central limit with two independent measures of complexity, N_{rxns} and S_{pthwy}, indicates that this result may apply to more complicated reaction systems that involve, for example, reversible steps and/or multiple reactants.

3.5 Acknowledgments

3.6 Literature Cited

(1) Mood, A. M.; Graybill, T. A.; Boes, D. C. *Introduction to the Theory of Statistics, 3rd Edition*; McGraw-Hill: New York, 1974.

(2) Reichl, L. E. *A Modern Course in Statistical Physics*; University of Texas Press: Austin, TX, 1980.

(3) Gillespie, D. T. The Chemical Langevin and Fokker-Planck Equations for the Reversible Isomerization Reaction. *J. Phys. Chem. A* **2002**, *106*, 5063.

(4) Simon, H. A. The Architecture of Complexity. *Proc. Am. Philos. Soc.* **1962**, *106*, 467.

(5) Poon, L.; Grebogi, C. Controlling Complexity. *Phys. Rev. Lett.* **1995**, *75*, 4023.

(6) Grassberger, P. Toward a Quantitative Theory of Self-Generated Complexity. *Int. J. Theor. Phys.* **1986**, *25*, 907.

(7) Lindgren, K.; Nordahl, M. G. Complexity Measures and Cellular Automata. *Complex Systems* **1988**, *2*, 409.

(8) Feldman, D. P.; Crutchfield, J. P. Measures of Statistical Complexity: Why? *Phys. Lett. A* **1998**, *238*, 244.

(9)   Szépfalusy, P.; Györgyi, G. Entropy Decay as a Measure of Stochasticity in Chaotic Systems. *Phys. Rev. A* **1986**, *33*, 2852.

(10)   Crutchfield, J. P.; Young, K. Inferring Statistical Complexity. *Phys. Rev. Lett.* **1989**, *63*, 105.

(11)   Crutchfield, J. P. The Calculi of Emergence: Computation, Dynamics and Induction. *Physica D* **1994**, *75*, 11.

(12)   Shalizi, C. R.; Crutchfield, J. P. Computational Mechanics: Pattern and Prediction, Structure and Simplicity. *J. Stat. Phys.* **2001**, *104*, 817.

(13)   Shiner, J. S.; Davison, M.; Landsberg, P. T. Simple Measure of Complexity. *Phys. Rev. E* **1999**, *59*, 1459.

(14)   Shannon, C. E. A Mathematical Theory of Communication. *Bell Syst. Tech. J.* **1948**, *27*, 379.

(15)   Li, W. On the Relationship between Complexity and Entropy for Markov Chains and Regular Languages. *Complex Systems* **1991**, *5*, 381.

(16)   Press, W. H.; Flannery, B. P.; Teukolsky, S. A.; Vetterling, W. T. *Numerical Recipes in C. The Art of Scientific Computing*; Cambridge University: Cambridge, England, 1988.

(17)   Urbansky, E. T. Don't Be Tricked by Your Integrated Rate Plot. *J. Chem. Educ.* **2001**, *78*, 921.
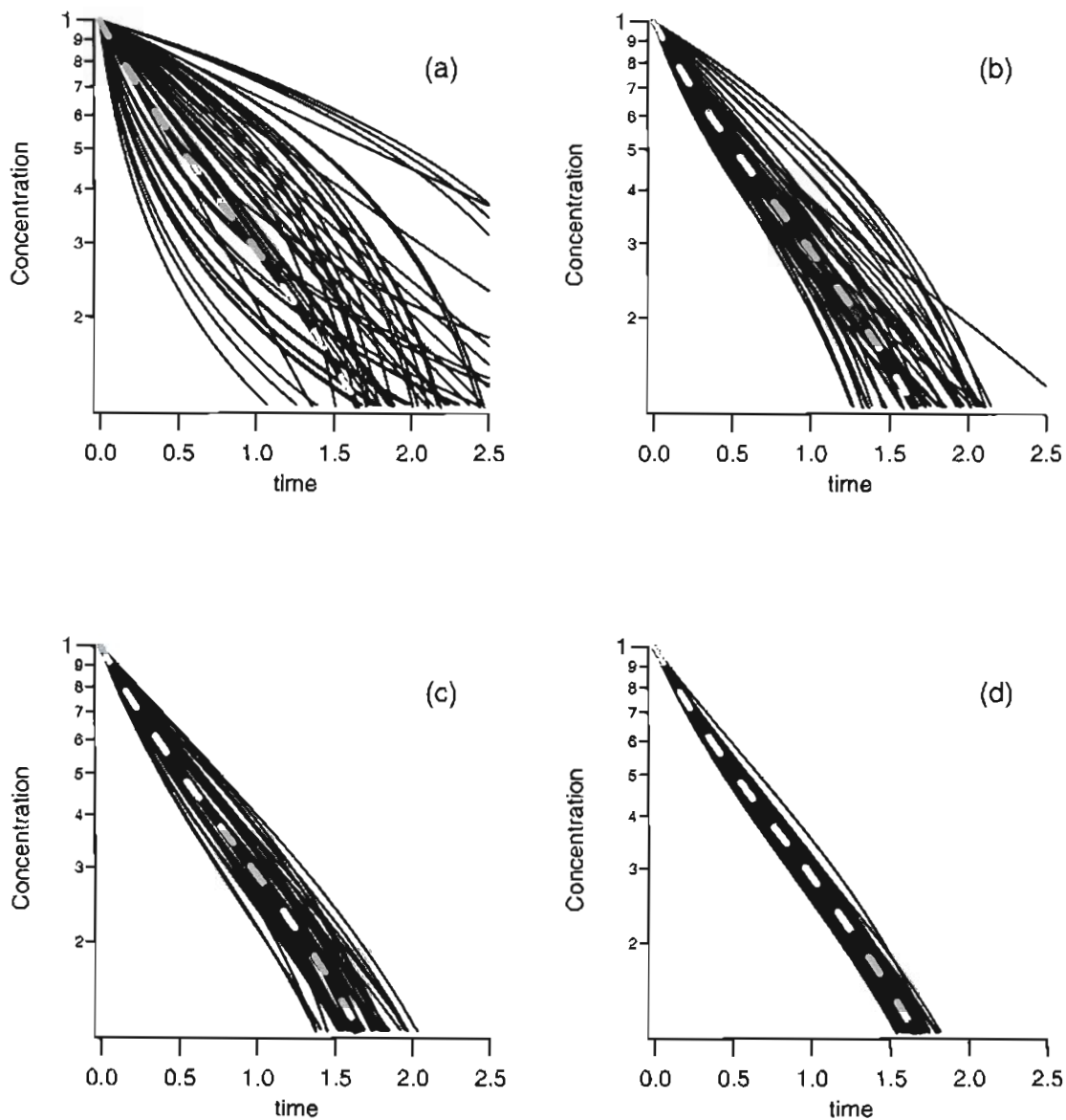
Figure 3.1.   Disappearance curves for ensembles (ensemble size = 50) with N_{rxns} = (a) 1, (b) 5, (c) 20 and, (d) 50. Rate constants and reaction orders selected stochastically. The limiting disappearance curve for $N_{rxns} \rightarrow \infty$ is marked by the dashed line in each plot.
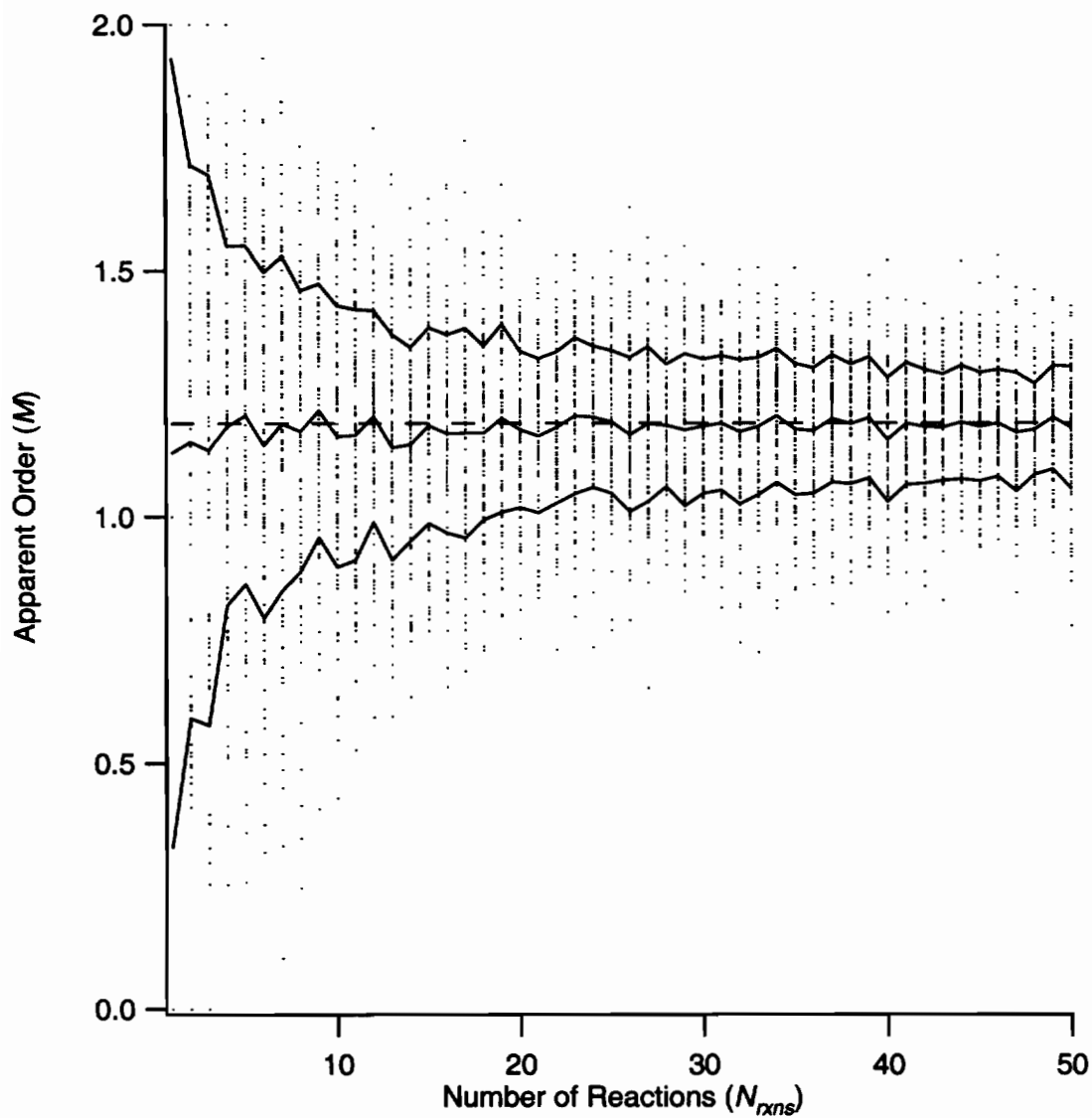
Figure 3.2.   Apparent order calculated for statistically generated ensembles (ensemble size = 100) with N_{rxns} varying from 1 to 50. Solid lines denote the average order and standard deviation about the average for each ensemble. The limiting apparent order is shown by the dashed line.
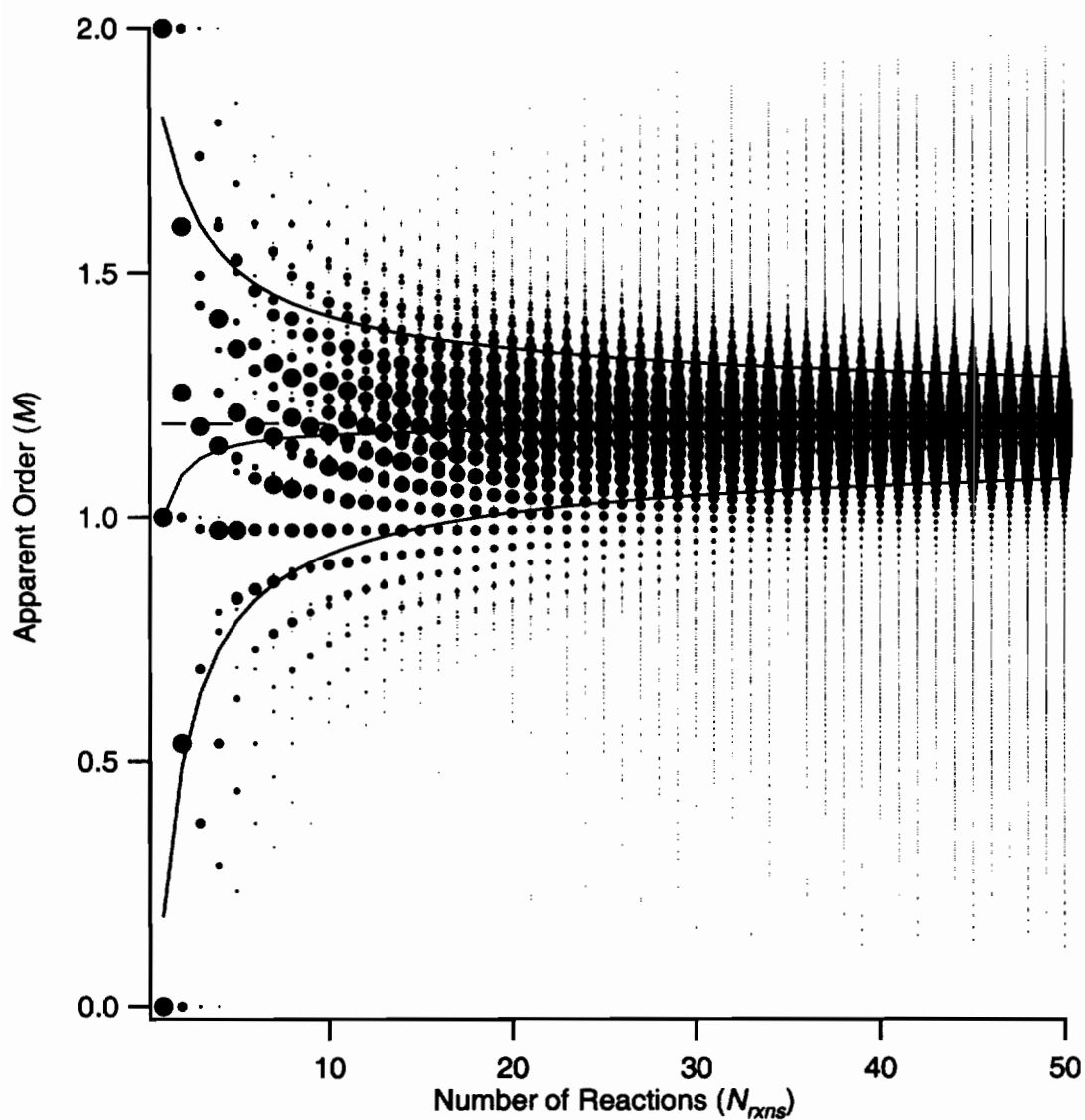
Figure 3.3.   Apparent order of all possible combinations of zero, first, and second

order reactions for N_{rxns} from 1 to 50. The point size indicates the weight

of the corresponding permutation relative to the other permutations for the

same N_{rxns}. Average and standard deviation curves are shown (as in Figure

3.2) and represent the theoretical limit of such lines for infinitely large,

statistically generated ensembles.
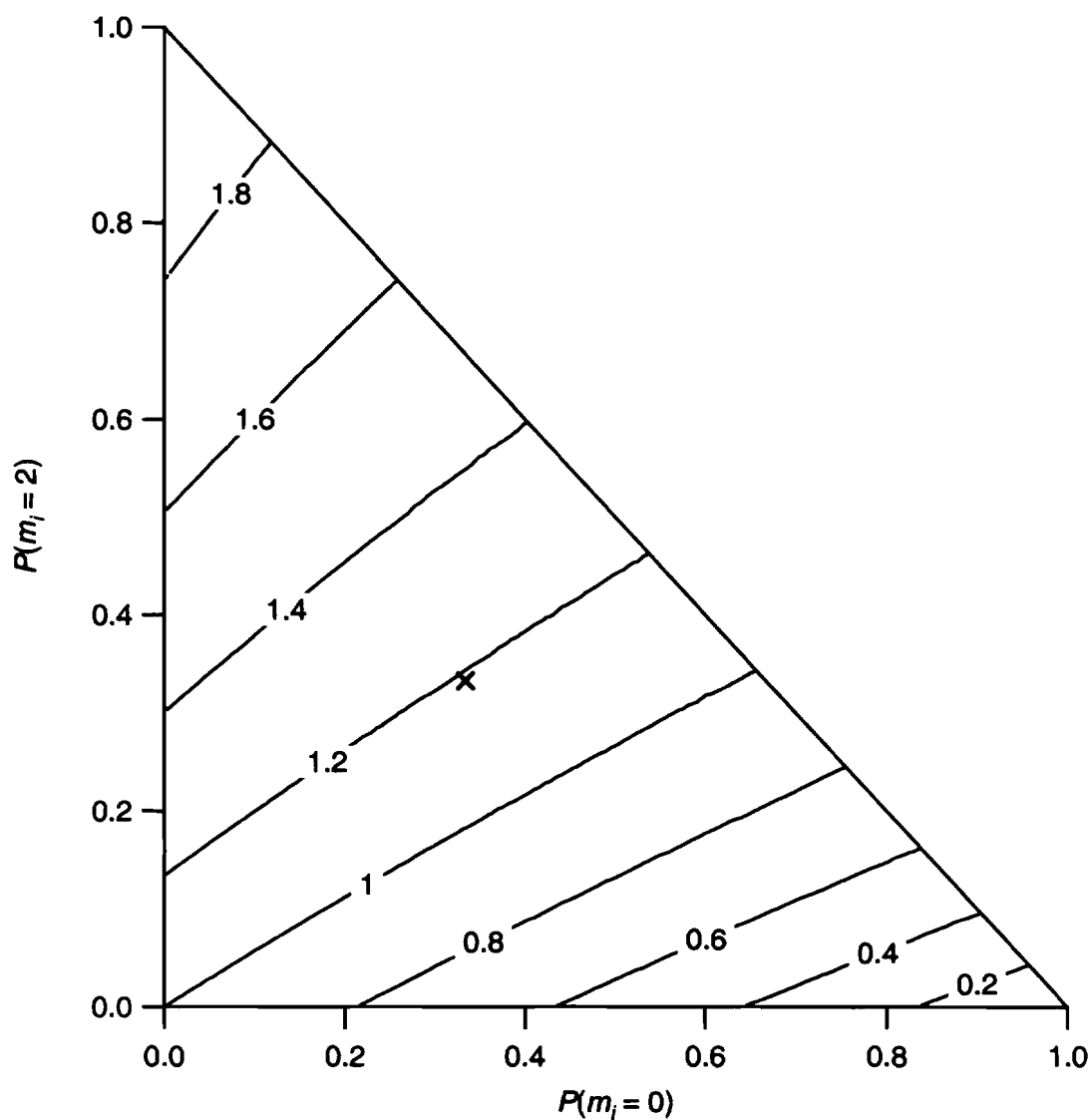
Figure 3.4. Contours of the limiting apparent order in the space of the probabilities used in selecting reaction orders. Purely second-order behavior is represented by point (0,1), purely first-order behavior by point (0,0), and purely zeroth-order behavior by point (1,0). The case considered in Figures 3.1-3.3 is marked with an "x".
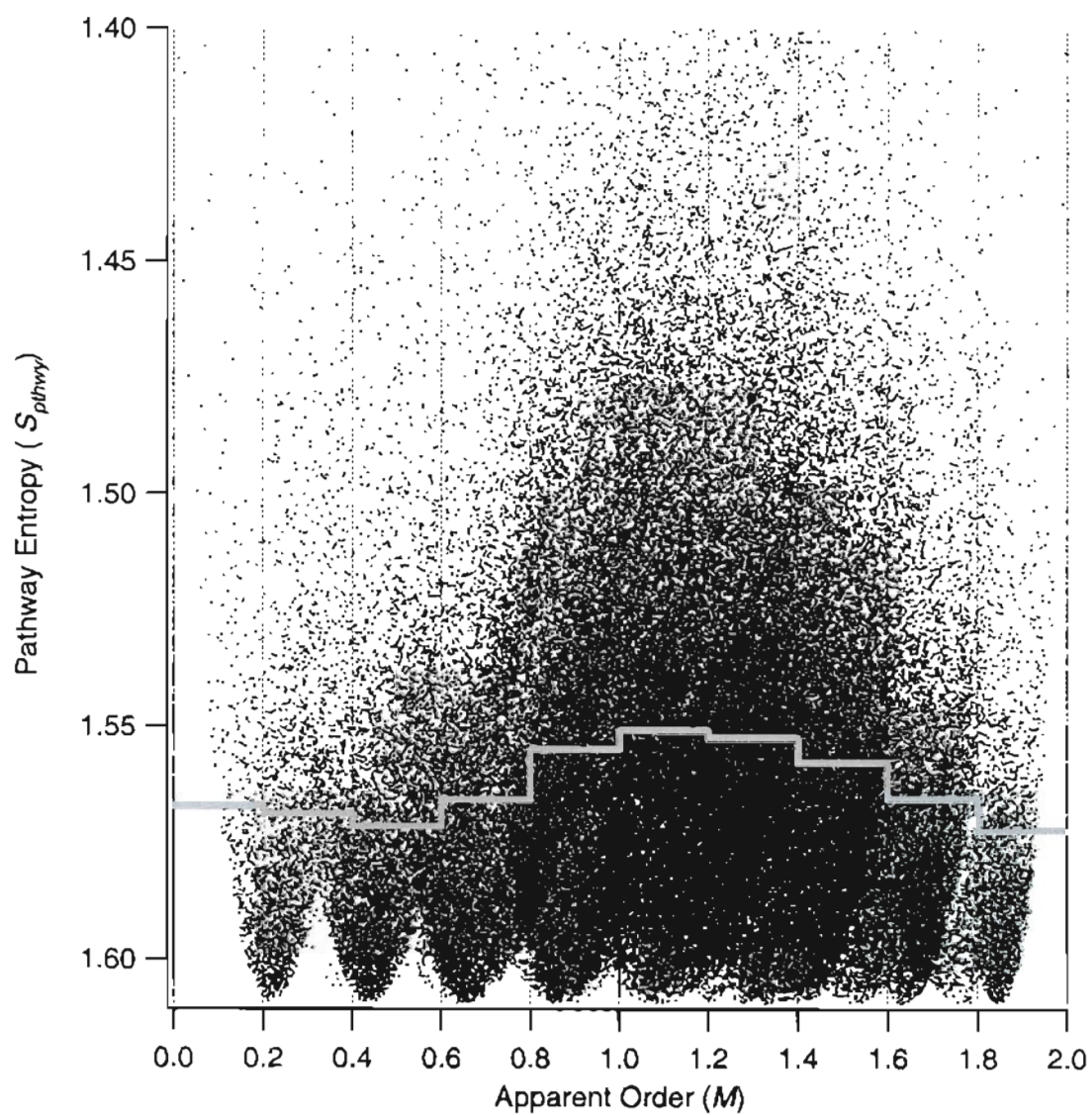
Figure 3.5. Scatter plot of pathway entropy (S_{pthwy}) vs. apparent order (M) for and ensemble of 10,000 statistically generated parallel reactions with $N_{rxns} = 5$. Smaller S_{pthwy} (smaller values towards the top) indicates larger complexity. The solid line denotes the average S_{pthwy} for all ensemble members in the noted order range.

CHAPTER 4

Applicability of Single-Site Rate Equations for Reactions on Inhomogeneous Surfaces[1]

4.1 Abstract

Single-site rate laws are broadly applicable to surface mediated chemical kinetics even though most surfaces are strongly inhomogeneous. We defined the best single-site approximation for an inhomogeneous rate law by square error minimization and, using this definition, examined the limits of the applicability of the single-site approximation and the nature of the errors that arise when inhomogeneity is ignored. We found that (*i*) correlation between kinetic inhomogeneity and sorptive inhomogeneity does not affect the success of the single-site approximation, (*ii*) many types of inhomogeneity produce similar macroscopic kinetic behavior, (*iii*) ignoring inhomogeneity in a single kinetic experiment causes rates to be overestimated at high and low concentrations and underestimated at intermediate concentrations, (*iv*) it is difficult to obtain detailed information about inhomogeneity from a single kinetic experiment, and (*v*) kinetic experiments over varying concentration ranges may be used to diagnose the existence of inhomogeneity and to parameterize an inhomogeneous rate law.

4.2 Introduction

Many chemical reactions are mediated by a reaction site that is not consumed during the reaction:

reactants + reaction site $\rightleftharpoons$ complexed reactants

  $\rightarrow$ complexed products $\rightleftharpoons$ products + reaction site   Scheme 1
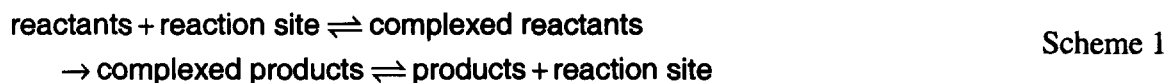
The reaction site can be an individual molecule, part of a macromolecule, or a site on a surface. Prominent examples where Scheme 1 applies include catalytic systems such as enzymatic reactions [1] and reactions employed in industrial synthesis [2], as well as a variety of heterogeneous processes such as electrode reactions [3], heterogeneous photochemical reactions [4], weathering of minerals [5], abiotic reduction of groundwater contaminants [6], and corrosion of metals [7].

Under most experimental, natural, and/or engineered conditions, concentrations of intermediate species in reactions of the type depicted in Scheme 1 rapidly approach a steady-state and appropriate rate laws can be obtained by assuming that the rates of formation of intermediate species are equal to the rates of destruction throughout the entire course of the reaction [2,8]. A particularly useful result arises from the steady-state treatment of the first-order transformation of a single reactant:

$$\equiv X + C \underset{k_{des}}{\overset{k_{ads}}{\rightleftharpoons}} \equiv XC \xrightarrow{k_{rxn}} \equiv X + P \qquad\qquad \text{Scheme 2}$$

where $\equiv X$ is the reaction site, C is the reactant, $\equiv XC$ is the precursor complex, and P is the product. In the case of surface mediated reactions, the corresponding rate law is usually written as the Langmuir-Hinshelwood equation:

$$-r = \frac{k_{rxn}K_{ss}C}{1+K_{ss}C} \qquad\qquad\qquad\qquad (1)$$

where r is the rate of disappearance of the reactant, C is the concentration of the reactant, k_{rxn} is the reaction rate constant as defined in Scheme 2, and K_{ss} is the steady-state analogue to the equilibrium partition coefficient: $K_{ss} = k_{des}/(k_{ads}+k_{rxn})$. The Langmuir-Hinshelwood equation (and its analogue for enzyme kinetics, the Michaelis-Menton equation) is readily extended to include multiple reactants, multi-stage reactions, and inter-species competition for reactive sites [9-11].

A critical assumption in the Langmuir-Hinshelwood treatment is that the surface is kinetically homogeneous [2,12], but numerous authors have noted that this assumption is

an improbable simplification for all but the most controlled systems [13,14]. Kinetic inhomogeneity can be classified as either induced or biographic [15]. Induced inhomogeneity is caused by interactions between adsorbed molecules [15]. Biographic inhomogeneity is caused by structural features of the surface such as defects, atomic scale surface roughness, and multi-crystalline composition of the bulk material [16-18].

The overall rate of a surface mediated reaction is equal to the expected value of the reaction rate calculated over all adsorbed reactant molecules [19]. Reaction rates on inhomogeneous surfaces will, therefore, exhibit a dependence on coverage that deviates from that which would be predicted on the basis of the reaction mechanism alone (e.g., the rate of a first-order surface mediated reaction on an inhomogeneous surface would be non-linear in the concentration of adsorbed molecules).

If the cause of inhomogeneity is known, it may be possible to calculate the inhomogeneous rate law directly. This approach has been taken by a number of authors in dealing with induced inhomogeneity by adding increased levels of detail to the mechanism of interaction between the adsorbate molecules [15,20]. A direct approach can also be taken if inhomogeneity can be quantified experimentally. This can be done, for example, by calculating the dependence of the kinetic parameters on an energetic parameter (usually via a linear free-energy relationship) and, then, finding the distribution of the energetic parameter experimentally [21,22].

In some systems where it is not feasible to calculate the rate law directly, it is possible to explain macroscopic observations on the basis of inhomogeneity. It has been shown, for example, that a number of empirical adsorption isotherms (such as those attributed to Freundlich, Dubinin-Radushkevich, and Temkin) and their corresponding heterogeneous rate laws can be rationalized by assuming a local Langmuir isotherm and the appropriate distribution for the free-energy of adsorption [15,20,23]. An indirect approach has also been used to explain qualitative features of heterogeneous reactions such as structure insensitivity [16-18] and the existence of maximally efficient rate controlling sites [24].

Given the amount of sophisticated study required to deal with inhomogeneity explicitly, many workers have pursued the development of heuristic rate equations that are applicable under a specific range of conditions [25]. Others have considered the effects

of various levels of approximation when evaluating inhomogeneous rate laws [13,14]. Given the broad experimental success of the Langmuir-Hinshelwood equation, it is possible that the Langmuir-Hinshelwood equation is, itself, an adequate heuristic rate law and that a single-site approximation is sufficient for most purposes when evaluating the kinetics of reactions on inhomogeneous surfaces. The goal of this investigation is to characterize (*i*) the breadth of applicability of approximate single-site kinetic models to inhomogeneous kinetic systems, (*ii*) the functional relationship between inhomogeneous kinetic models and the corresponding single-site approximation, and (*iii*) the errors that arise when surface inhomogeneity is neglected.

4.3 Approach

4.3.1 Representative Inhomogeneous Rate Law

To investigate the applicability of a single-site approximation, we needed to generate rate laws that exhibit variable degrees of inhomogeneity. For this purpose, we selected homotattic inhomogeneity (i.e., contiguous patches with homogeneous properties [26]) with the Langmuir equation taken as the local isotherm, which gives the following rate law:

$$-r = \int_0^\infty \int_0^\infty \frac{k_{rxn} K_{ss} C}{1 + K_{ss} C} \sigma(k_{rxn}, K_{ss}) \, dk_{rxn} \, dK_{ss} \tag{2}$$

where $\sigma(k_{rxn}, K_{ss})$ represents the distribution function of sites with kinetic parameters k_{rxn} and K_{ss}. In selecting the form of σ, we required a distribution function that could be varied from single-site to inhomogeneous with only the variation of a few parameters. We found that continuous unimodal distributions (e.g., Gaussian) can only produce nearly single-site behavior, and that continuous multimodal distributions require too many parameters to be investigated succinctly. Focusing on discrete distributions, we found that, for any n-site distribution, a two-site distribution can be formed that is more inhomogeneous than the n-site distribution by allowing a sufficiently large difference between the sites in the two-site distribution. Therefore, we used the two-site Langmuir-Hinshelwood equation as our inhomogeneous rate law:

$$-r = \frac{k_{rxn}^1 K_{ss}^1 C}{1 + K_{ss}^1 C} \sigma_1 + \frac{k_{rxn}^2 K_{ss}^2 C}{1 + K_{ss}^2 C}(1 - \sigma_1) \tag{3}$$

where K^j_{rxn} is the reaction rate constant, K^i_{ss} is the steady-state analogue to the equilibrium partition coefficient on site i, and σ_1 is the fraction of type 1 sites (note that the site distribution function must be non-negative and normal [27]). The numbering of site types is arbitrary, so, we require K^1_{ss} to be smaller than K^2_{ss}.

4.3.2 Degeneracy of k_{rxn} Inhomogeneity

The site distribution function, $\sigma(k_{rxn}, K_{ss})$, is degenerate in that an infinite number of site distribution functions will lead to the same inhomogeneous rate law. To see this, we rearrange the order of operations in eq 2.

$$-r = \int_0^\infty \frac{K_{ss}C}{1+K_{ss}C}\left(\int_0^\infty k_{rxn}\sigma(k_{rxn}, K_{ss})dk_{rxn}\right) dK_{ss} \tag{4}$$

Notice that integration over k_{rxn} yields a function of K_{ss} only and that many site distribution functions will yield the same result. We can, therefore, define an equivalence class as all site distribution functions that yield the same result upon evaluating the integral over k_{rxn} in eq 4. Since all members of such an equivalence class are macroscopically indistinguishable, we can perform subsequent analyses on only one site distribution function from each equivalence class.

For the analysis that follows, we select the representative site distribution function by factoring the expected value of k_{rxn}, $E[k_{rxn}]$, out of eq 4.

$$-r = E[k_{rxn}]\int_0^\infty \frac{K_{ss}C}{1+K_{ss}C}\,\bar{\sigma}(K_{ss})\,dK_{ss} \tag{5}$$

where $\bar{\sigma}$ is the equivalent uncorrelated site distribution function defined by:

$$\bar{\sigma}(K_{ss}) = \frac{\int_0^\infty k_{rxn}\sigma(k_{rxn}, K_{ss})dk_{rxn}}{\int_0^\infty\int_0^\infty k_{rxn}\sigma(k_{rxn}, K_{ss})dk_{rxn}dK_{ss}} \tag{6}$$

Comparison of eq 2 with eqs 5-6 indicates that the inhomogeneous rate law for any site distribution function (with arbitrary correlation between k_{rxn} and K_{ss}) can be replaced with the inhomogeneous rate law for an equivalent uncorrelated site distribution function, $\bar{\sigma}$. In the case of discrete inhomogeneity (e.g., eq 3), $\bar{\sigma}$ is defined as:

$$\bar{\sigma}_i = \frac{k^i_{rxn}\sigma_i}{E[k_{rxn}]} \qquad (7)$$

Based on the analysis above, one could not expect to observe macroscopic effects due to inhomogeneity in the surface reaction rate constant. Furthermore, we can focus on uncorrelated site distribution functions without any loss of generality.

4.3.3 Single-Site Approximation to Inhomogeneous Rate Law

In defining a single-site approximation to an inhomogeneous rate law, we require that the approximation reproduce the data that would be obtained from a kinetic experiment with the inhomogeneous system as accurately as possible. Kinetic data for heterogeneous systems can be collected and analyzed by either the integral method or the differential method [28]. The integral method, known in enzyme kinetics as progress curve analysis [29], involves collecting a time series of concentration data and fitting these data with the integrated form of the rate law (e.g. [30]). The differential method, known in enzyme kinetics as saturation curve analysis [1], involves collecting reaction rate measurements at several concentrations and fitting these data with the rate law (e.g. [31]).

The advantages and disadvantages of integral and differential analysis have been discussed extensively [29,32-35]. We have collected kinetic data for the reduction of solutes by iron metal in a batch reactor using the integral (progress curve) method [36,37] and, therefore, we chose to examine inhomogeneity from the integral perspective: i.e., by fitting concentration time series data. Preliminary calculations from the differential (saturation curve) perspective yielded the same general trends as those presented below.

Intuitively, one might expect that a single-site approximation can be obtained by substituting the average rate parameters ($E[k_{rxn}]$ and $E[K_{ss}]$) into the single-site rate law. We investigated this notion and found that the average parameter rate law significantly overestimates the magnitude of the of the reaction rate (results shown below). In the absence of formulae for the best single-site parameters, we defined the single-site approximation as the single-site rate law (eq 1) that best fits a given inhomogeneous rate law (eq 2). We expressed the inhomogeneous rate law in dimensionless form:

$$\frac{dC}{d(E[k_{rxn}]t)} = \frac{dC}{d\tau} = -\int_0^\infty \frac{K_{ss}C}{1+K_{ss}C} \, \bar{\sigma}(K_{ss}) \, dK_{ss} \qquad (8)$$

where τ is time scaled by $E[k_{rxn}]$. The two-site model and the single-site approximation can, then, be written as:

$$\frac{dC}{d\tau} = -\frac{K_1 C}{1 + K_1 C}\sigma_1 - \frac{K_2 C}{1 + K_2 C}(1 - \sigma_1)$$ (9)

$$\frac{dC}{d\tau} = -\frac{\kappa K^{1\text{-}S} C}{1 + K^{1\text{-}S} C}$$ (10)

where K_1, K_2, and $K^{1\text{-}S}$ are the two-site and single-site steady-state sorption constants (note that, for convenience, we have dropped the "ss" subscript) and κ is the ratio of the single-site surface reaction rate constant and the expected value of the inhomogeneous surface reaction rate constant:

$$\kappa = \frac{k_{rxn}^{1\text{-}S}}{E[k_{rxn}]}$$ (11)

We obtained implicit solutions to both the two-site inhomogeneous rate law (eq 9) and the single-site approximation (eq 10) by direct integration. Time series of concentration were obtained from the implicit solutions using Brent's method [38] and the single-site approximation was fit using Levenberg-Marquardt minimization of square error (χ^2) [38].

Our definition of a single-site approximation can be viewed as a function. The argument of the function is a site distribution function. The site distribution function is operated on by solving the corresponding inhomogeneous rate law and performing the single-site fit. The resulting outputs are the single-site parameters ($K^{1\text{-}S}$ and κ) as well as any goodness-of-fit measures generated by the fitting routine. We use the latter to examine the accuracy of the single-site approximation.

4.3.4 Inverting the Single-Site Approximation Function

The site distribution function, $\sigma(k_{rxn}, K_{ss})$, is typically unknown. A single-site model, however, can be obtained by fitting the single-site rate law to experimentally obtained kinetic data. In this sense, single-site approximations are readily available for a variety of surface mediated reactions. We would, therefore, like to take as input some apparent single-site behavior (i.e., a single value of $K^{1\text{-}S}$) and derive information about inhomogeneity that might be present within the system that generated the apparent single-

site behavior. This requires that we invert the single-site approximation function (ignoring κ and goodness-of-fit measures).

When the site distribution function is a Dirac delta function, the inhomogeneous rate law (eq 8) will be exactly equivalent to the single site rate law (eq 10) with $\kappa = 1$. Since the Dirac delta function can peak at any value of K_{ss}, we conclude that at least one site distribution function will yield any positive K^{1-S} and, therefore, that the single-site approximation function is surjective (onto).

The Dirac delta function can be perturbed by adding a second site. If the perturbation is small enough, the resulting two-site distribution function will have the same single-site approximation as the original delta function. Many site distribution functions will, therefore, yield the same K^{1-S} and the single-site approximation function is not injective (one-to-one). Formally, an inverse can be defined only for bijective (one-to-one and onto) functions. We can, however, define a partial inverse of the single-site approximation by restricting the range of allowed site distributions (e.g., to uncorrelated two-site distributions) and finding all such site distributions that are best fit by a single-site approximation with the appropriate value of K^{1-S}. We performed this calculation for the two-site distribution by fixing the values of K_1 and K_2 and then bisecting σ_1 (starting with endpoints 0 and 1) until K^{1-S} for the midpoint was within 0.01% of the target K^{1-S} and the maximum possible error in σ_1 was less than $5\text{x}10^{-13}$.

4.4 Results

4.4.1 Average Parameter Rate Laws Overestimate the Reaction Rate

One way to formulate a single-site approximation is to calculate average kinetic parameters. As we noted above, this procedure results in an unsatisfactory rate law. To see this, we begin by expanding the inhomogeneous rate law in terms of the n-th order moments of K_{ss} around the expected value of K_{ss}.

$$\frac{dC}{dt} = E[k_{rxn}]\left(-\frac{E[K_{ss}]C}{1+E[K_{ss}]C} + \sum_{n=2}^{\infty}(-1)^n \frac{C^n}{(1+E[K_{ss}]C)^{n+1}} E[(K_{ss} - E[K_{ss}])^n] \right) \qquad (12)$$

The first term in this expression is equivalent to the average parameter rate law. The summation is equal to the error induced by parameter averaging. This series converges to a finite positive value.

$$\sum_{n=2}^{\infty}(-1)^n \frac{C^n}{(1+E[K_{ss}]C)^{n+1}} E[(K_{ss}-E[K_{ss}])^n] = \left(\frac{C}{1+E[K_{ss}]C}\right)^2 E\left[\frac{(E[K_{ss}]-K_{ss})^2}{1+K_{ss}C}\right] \quad (13)$$

The average parameter rate law will, therefore, overestimate the magnitude of the reaction rate.

The magnitude of the overestimation by the average parameter rate law can be investigated by considering an example. Figure 4.1 shows a progress curve for the reduction of 2,4,6-trinitrotoluene (TNT) on granular iron metal (8.3 g/L) that we previously described using a single-site Langmuir-Hinshelwood kinetic expression [36,37]. These data contain sufficient structure to be fit by a two-site rate law (eq 3) and, subsequently, the average parameters may be calculated. Comparison of the two-site fit and the average parameter rate law—shown in Figure 4.1 as solid and dashed lines, respectively—indicates that the magnitude of the overestimation is quite large even though an accurate single-site approximation clearly exists.

4.4.2 Many Two-Site Models are Consistent with a Typical Progress Curve

Inhomogeneity can cause a progress curve to exhibit curvature that can not be fully described by a single-site fit. By examining the residual plots for single-site fits to a large number of progress curves [36], we have identified a number of progress curves with features that suggest inhomogeneity. An example of this is shown in Figure 4.1A, along with single-site (eq 1) and two-site (eq 3) fits. Both the single-site and the two-site models capture the major features of the data. The residual plots for the two fits (Figure 4.1B) indicate that the two-site model improves both the magnitude of the fitting error and the distribution of the residuals. We can not, however, conclude that the two-site rate law is a superior model for these data because the improved fit may reflect either true inhomogeneity or merely the effect of additional degrees of freedom in the model.

The nature of the two-site fit can be investigated further by examining the behavior of χ^2 in the space of the two-site fitting parameters. Figure 4.1C shows the dependence of χ^2 on the two-site sorption constants, K_1 and K_2. At each point, the initial

concentration (C_0) and site distribution (σ) have been varied to the point of minimum (local) χ^2. The right and bottom boundaries of this plot are $K_1 = K^{1-S}$ and $K_2 = K^{1-S}$ respectively. On either of these boundaries, the two-site model is identical to the best fit single-site model. Moving from either of the single-site boundaries into the interior region (where $K_1 < K^{1-S}$ and $K_2 > K^{1-S}$) initially produces a sharp decrease in square error, indicating that this degree of inhomogeneity is altering the structure of the progress curve. Further into the interior region, the χ^2 surface flattens out, so much so that, for these data, it is numerically impossible to distinguish a distinct minimum in the K_1 dimension. For practical purposes, the minimum exists where $\chi^2 = 2.38$ μM^2 and is shaped as an elongated trough at $K_2 = 0.39$ μM^{-1} extending over the range 1.4×10^{-10} $\mu M^{-1} < K_1 < 4.7 \times 10^{-8}$ μM^{-1}.

Based on the results in Figure 4.1, as well as the general success of single-site rate laws that we noted in the introduction, we can not expect to obtain reliable information about inhomogeneity from a single progress curve. In many cases, inhomogeneity will not be evident in a single kinetic experiment, but even when inhomogeneity is evident we still may not be able to uniquely parameterize an inhomogeneous rate law, as is the case with the data shown in Figure 4.1.

Only with a kinetic experiment comprised of very precise concentration measurements over a broad concentration range can we expect to obtain reliable information about inhomogeneity from a single experiment. We can, however, find a unique single-site kinetic model for most kinetic experiments and, therefore, we can examine the range of inhomogeneous models that are consistent with a single progress curve using the inversion procedure described above. Figure 4.2A shows the average square error, $\langle \chi^2 \rangle$, produced by the inversion using the fit to the TNT data shown in Figure 4.1A as the input single-site approximation. The $\langle \chi^2 \rangle = 0$ contour follows $K_2 = K^{1-S}$ in the horizontal direction and $K_1 = K^{1-S}$ in the vertical direction. Along this contour, the only two-site system that is consistent with the given single-site approximation is that in which one of the two sites has a site density of zero. The error between the two-site system and the single-site approximation increases toward the upper left where K_1 becomes much smaller, and K_2 becomes much larger, than K^{1-S}.

Each of the $\langle\chi^2\rangle$ contours appears to be approaching an asymptotic value of K_2 with decreasing K_1. Noting the log scaling of the axis, this indicates that $\langle\chi^2\rangle$ approaches some well defined function of K_2 as K_1 goes to zero. Asymptotic behavior of $\langle\chi^2\rangle$ is also apparent with increasing K_2. In the latter case we can calculate a limit analytically:

$$\lim_{K_2\to\infty}\frac{dC}{d\tau} = \lim_{K_2\to\infty}\left(-\frac{K_1C}{1+K_1C}\sigma_1 - \frac{K_2C}{1+K_2C}\sigma_2\right) = -\frac{K_1C}{1+K_1C}\sigma_1 - \sigma_2 = -\frac{\sigma_2+K_1C}{1+K_1C} \tag{14}$$

By using eq 14 as the two-site rate law we can calculate the properties of the single-site approximation when K_2 becomes infinitely large. Figure 4.2B shows the limiting behavior of $\langle\chi^2\rangle$ as a function of K_1. Once again, the curve approaches an asymptote as K_1 becomes small. We can conclude that, for the single-site approximation derived from the data in Figure 4.1A, the systematic error induced by treating the data with a homogeneous model is not larger than approximately 1.1 μM^2 per point in the time series data.

In the preceding discussion, we have utilized the sum of square errors to indicate goodness-of-fit. In general, it is good practice to use multiple methods in examining the success of a fitting exercise. This is especially true in this study where the main concern is errors due to systematic model failure rather than experimental noise. Figure 4.2C shows residuals (two-site minus single-site) plotted against $\kappa\tau$ ($= k_{rxn}t$) for two-site systems that lie along selected $\langle\chi^2\rangle$ contours (as depicted in Figure 4.2A) between $K_1 = 10^{-11}$ and $K_2 = \infty$. All residual curves corresponding to a single $\langle\chi^2\rangle$ contour were found to lie between the residual plot for the infinite K_2 case and the small K_1 case.

The maximum absolute values of the residual plots shown in Figure 4.2C are small ($< 1\%$) in comparison to C_0 for the data in Figure 4.1A. This indicates that, even for the cases in Figure 4.2A with largest $\langle\chi^2\rangle$, the systematic errors induced by treating an inhomogeneous system with a single-site model would be insignificant and difficult to detect. There is little difference in residual plots corresponding to a single $\langle\chi^2\rangle$ contour indicating that $\langle\chi^2\rangle$ is a reliable indicator of goodness-of-fit.

Both the residual plot for a single-site fit to the sample data (Figure 4.1B) and the residual plots in Figure 4.2C show a pattern of error where the single-site approximation over-estimates concentrations near the endpoints of the progress curve and under-

estimates concentrations in the middle. This is indicative of the fact that the solution to the inhomogeneous rate law contains curvature that the single-site approximation can not reproduce. More specifically, the single-site approximation must underestimate the reaction rate at high and low concentrations in order to obtain a progress curve that minimizes χ^2 over the entire concentration range. As we show below, this effect is most pronounced when a single-site approximation is used to extrapolate to concentrations outside the range of experimental data.

4.4.3 Errors that Arise when Inhomogeneity is Ignored

A characteristic of heterogeneous chemical reactions is the existence of kinetic regimes for sorption limited, desorption limited, site saturation, and pseudo-first-order kinetics. Part of the utility of the Langmuir-Hinshelwood equation stems from its ability to describe both the site saturation and pseudo-first-order kinetic regimes:

$$\lim_{C \to \infty} \frac{dC}{d\tau} = \lim_{C \to \infty} -\frac{\kappa K^{1\text{-}S}C}{1+K^{1\text{-}S}C} = -\kappa \tag{15}$$

$$\lim_{C \to 0} \frac{dC}{d\tau} = \lim_{C \to 0} -\frac{\kappa K^{1\text{-}S}C}{1+K^{1\text{-}S}C} = \lim_{C \to 0} -\kappa K^{1\text{-}S}C \tag{16}$$

The inhomogeneous version of the Langmuir-Hinshelwood equation retains this feature of zero-order behavior at high concentrations transitioning to first-order behavior at low concentrations:

$$\lim_{C \to \infty} \frac{dC}{d\tau} = \lim_{C \to \infty} -\int_0^\infty \frac{K_{ss}C}{1+K_{ss}C} \, \bar{\sigma}(K_{ss}) \, dK_{ss} = -1 \tag{17}$$

$$\lim_{C \to 0} \frac{dC}{d\tau} = \lim_{C \to 0} -\int_0^\infty \frac{K_{ss}C}{1+K_{ss}C} \, \bar{\sigma}(K_{ss}) \, dK_{ss} = \lim_{C \to 0} -E[K_{ss}]C \tag{18}$$

This limiting behavior provides another basis for comparison of an inhomogeneous model and the corresponding single-site approximation. To do this, we defined the limiting inhomogeneous rate divided by the limiting rate predicted by the single-site approximation as zero-order (Z.O.) and first-order (F.O.) ratios:

$$\text{Z.O. ratio} = \frac{E[k_{rxn}]}{k_{rxn}^{1\text{-}S}} = \frac{1}{\kappa} \tag{19}$$

$$\text{F.O. ratio} = \frac{E[k_{rxn}K_{ss}]}{k_{rxn}^{1-S}K_{ss}^{1-S}} = \frac{E[K_{ss}]}{\kappa K_{ss}^{1-S}} \tag{20}$$

Figure 4.3 depicts the limiting rate ratios for the range of two-site models that are consistent with the approximate single-site behavior for the data in Figure 4.1A. Along the single-site boundary, the single-site approximation is exact and the ratios are 1. Both ratios are everywhere greater than or equal to one and increase with decreasing K_1 and increasing K_2. Calculations (not shown) indicate that, in the limit of infinite K_2, the zero-order ratio approaches finite values for all $K_1 > 0$ and infinity for $K_1 = 0$. These calculations also reveal non-zero values of σ_1 for $0 < K_1 < K^{1-S}$ indicating that the first-order ratio approaches infinity under this condition. As was the case with χ^2 (Figure 4.2A), Figures 4.3A and 4.3B show increasing effects of inhomogeneity with decreasing K_1 and increasing K_2.

Because the Z.O. and F.O. ratios are everywhere greater than one, the effect of ignoring inhomogeneity would be an underestimation of reaction rates at both high and low concentrations. This is consistent with the pattern in the residual plot for a single-site fit in Figure 4.1B and, in a broad sense, this result is similar to the errors that can be caused by using a pseudo-first-order rate law for heterogeneous reactions [39] and those that arise when inhibition of the reaction due to reaction products is ignored [40]. The underestimation of reaction rates presents a particularly difficult problem in systems where the range of concentrations that are available experimentally are different than those that are of practical importance. When this situation arises, experiments that test specifically for inhomogeneity should be performed before extrapolation from one concentration range to another is made.

4.4.4 Site Averaging is Affected by Concentration Range

Up to this point in our analysis, we have examined the effects of inhomogeneity on individual progress curves with an associated concentration range. The single-site approximation is dependent on this fixed concentration range, and therefore, the effects of inhomogeneity will vary with experimental parameters such as initial concentration, C_0. We have investigated the effect of C_0 by selecting two-site parameters from the minima in Figure 4.1C ($K_2 = 3.9 \times 10^{-1}$ μM^{-1}, $K_1 = 3.5 \times 10^{-9}$ μM^{-1}, $\sigma_2 = 2.3 \times 10^{-8}$) and

calculating the single-site approximation for a number of concentration ranges. The results of these calculations are depicted in Figure 4.4 as contours of constant K^{1-S}, first-order ratio, and zero-order ratio in the space of C_0 and final concentration, C_{fin}. Note that C_0 must be greater than C_{fin} and, therefore, the surfaces are undefined below $C_0 = C_{fin}$.

Figure 4.4A shows that K^{1-S} decreases with increasing concentration range (i.e. increasing C_0 and/or C_{fin}). As the concentration range approaches zero, K^{1-S} approaches K_2, while K^{1-S} approaches K_1 as the concentration range becomes large. This result is consistent with the conclusion of Dzombak et al. [41] that, in multi-site adsorption, the isotherm is controlled by the strongest adsorption site at low concentration and by the weakest adsorption site at high concentration. Kinetic experiments performed at high concentrations will, therefore, emphasize the reactivity of and reaction mechanisms associated with weak adsorption sites while low concentration experiments will emphasize strong adsorptions sites.

As we note above, both the single-site and the two-site rate laws give zero-order behavior at high concentrations and first-order behavior at low concentrations. The first-order ratio (Figure 4.4B), therefore, approaches 1 as C_0 approaches zero and the zero-order ratio (Figure 4.4C) approaches 1 as C_{fin} approaches infinity. This, along with the limiting behavior of K^{1-S}, yields the following relationships between the first-order and zero-order rate constants from the single-site fit and the two-site distribution function:

$$\lim_{C_0 \to 0} k_{rxn}^{1-S} K_{ss}^{1-S} = E[k_{rxn} K_{ss}] \tag{21}$$

$$\lim_{C_0 \to 0} k_{rxn}^{1-S} = \frac{E[k_{rxn} K_{ss}]}{K_2} \tag{22}$$

$$\lim_{C_{fin} \to \infty} k_{rxn}^{1-S} K_{ss}^{1-S} = E[k_{rxn}] K_1 \tag{23}$$

$$\lim_{C_{fin} \to 0} k_{rxn}^{1-S} = E[k_{rxn}] \tag{24}$$

Low concentration progress curves (eqs 21 and 22) yield complete information about the first-order rate constant ($E[k_{rxn} K_{ss}]$) and very little information about the zero-order rate constant ($E[k_{rxn}]$), while high concentration progress curves (eqs 23 and 24) yield complete information about $E[k_{rxn}]$ and very little information about $E[k_{rxn} K_{ss}]$.

From this analysis, we conclude that inhomogeneity can be qualitatively identified by comparing the results of kinetic experiments performed over different

concentration ranges. If inhomogeneity is a significant feature of the system being studied, the following relationships should be evident from single-site fits to the data:

$$K_{ss}^{1-S}\big|_{\text{High Conc.}} < K_{ss}^{1-S}\big|_{\text{Low Conc.}} \tag{25}$$

$$k_{rxn}^{1-S}\big|_{\text{High Conc.}} > k_{rxn}^{1-S}\big|_{\text{Low Conc.}} \tag{26}$$

If inhomogeneity is detected, then an inhomogeneous kinetic model (such as eq 3) could be parameterized by global fitting where a single site distribution function is found that minimizes the total χ^2 across both the high concentration and low concentration experiments. Alternatively, the zero-order and first-order rate constants could be found independently from initial rate data, and an inhomogeneous rate law could be fit to data from additional kinetic experiments under the constraint that the fitted rate law return the correct values of $E[k_{rxn}]$ and $E[k_{rxn} K_{ss}]$.

4.5 Acknowledgements

4.6 Literature Cited

(1)   Segel, I. H. *Enzyme Kinetics*; Wiley: New York, 1975.

(2)   Hougen, O. A.; Watson, K. M. *Chemical Process Principles*; J. Wiley & Sons, inc.: New York, 1943.

(3)   Bard, A. J.; Faulkner, L. R. *Electrochemical Methods. Fundamentals and Applications*; 2nd ed.; Wiley: New York, 2001.

(4)   Grätzel, M. *Heterogeneous Photochemical Electron Transfer*; CRC: Boca Raton, Florida, 1989.

(5)   Blesa, M. A.; Morando, P. J.; Regazzoni, A. E. *Chemical Dissolution of Metal Oxides*; CRC Press: Ann Arbor, 1994.

(6)   Scherer, M. M.; Balko, B. A.; Tratnyek, P. G. The Role of Oxides in Reduction Reactions at the Metal-Water Interface. In *Mineral-Water Interfacial Reactions:*

Kinetics and Mechanisms; Sparks, D. L., Grundl, T. J., Eds.; American Chemical Society: Washington, DC, 1998; Vol. ACS Symp. Ser. 715; pp 301.

(7)   Jones, D. A. *Principles and Prevention of Corrosion*; Macmillan: New York, 1992.

(8)   Viossat, V.; Ben-Aim, R. I. A Test of the Validity of Steady State and Equilibrium Approximations in Chemical Kinetics. *J. Chem. Educ.* **1993**, *70*, 732.

(9)   Hougen, O. A.; Watson, K. M. Solid Catalysts and Reaction Rates. *Industrial and Engineering Chemistry* **1943**, *35*, 529.

(10)   Yang, K. H.; Hougen, O. A. Determination of Mechanism of Catalyzed Gaseous Reactions. *Chem. Eng. Prog.* **1950**, *46*, 146.

(11)   Temkin, M. I. Theoretical Models of the Kinetics of Heterogeneous Catalytic Reactions. *Kinet. Katal.* **1972**, *13*, 555.

(12)   Langmuir, I. The Adsorption of Gases on Plane Surfaces of Glass, Mica and Platinum. *J. Am. Chem. Soc.* **1918**, *40*, 1361.

(13)   Cardona-Martinez, N.; Dumesic, J. A. Applications of Adsorption Microcalorimetry to the Study of Heterogeneous Catalysis. *Adv. Catal.* **1992**, *38*, 149.

(14)   Boudart, M. Classical Catalytic Kinetics: A Placebo or the Real Thing? *Ind. Eng. Chem. Fund.* **1986**, *25*, 656.

(15)   Doraiswamy, L. K. Catalytic Reactions and Reactors: A Surface Science Approach. *Prog. Surf. Sci.* **1991**, *37*, 1.

(16)   Boudart, M.; Djega-Mariadassou *Kinetics of Heterogeneous Catalytic Reactions*; Princeton University Press: Princeton, NJ, 1984.

(17)   Wise, H.; Oudar, J. *Material Concepts in Surface Reactivity and Catalysis*; Academic Press: San Diego, CA, 1990.

(18)   Rudzinski, W.; Everett, D. H. *Adsorption of Gases on Heterogeneous Surfaces*; Academic Press: London, 1992.

(19)   Broadbelt, L. J.; Rekoske, J. E. Necessary Levels of Detail in Microkinetic Models of Catalytic Reactions on Nonuniform Surfaces. *Chem. Eng. Sci.* **1996**, *51*, 3337.

(20)   Cerofolini, G. F.; Rudzinski, W. Theoretical Principles of Single- and Mixed-Gas Adsorption Equilibria on Heterogeneous Solid Surfaces. In *Equilibria and*

Dynamics of Gas Adsorption on Heterogeneous Solid Surfaces; Rudzinski, W., Steele, W. A., Zgrablich, G., Eds.; Elsevier: Amsterdam, 1997; Vol. 104; pp 1.

(21)   Wedler, G. *Chemisorption: An Experimental Approach*; Butterworths: London, 1970.

(22)   Hunger, B.; Hoffman, J. Temperature-Programmed Surface Reactions (TPSR) on Heterogeneous Surfaces. *J. Therm. Anal.* **1993**, *40*, 1347.

(23)   Cerofolini, G. F. A Unified Theory for Freundlich, Dubnin-Radushkevich, and Temkin Behaviors. *J. Coll. Int. Sci.* **1982**, *86*, 204.

(24)   Halsey, G. D. Catalysis on Non-Uniform Surfaces. *J. Chem. Phys.* **1949**, *17*, 758.

(25)   Levenspiel, O. Chemical Reaction Engineering. *Ind. Eng. Chem. Res.* **1999**, *38*, 4140.

(26)   Sanford, C.; Ross, S. Homotattic Surface-a Suggested New Word. *J. Phys. Chem.* **1954**, *58*, 288.

(27)   Ross, S.; Olivier, J. P. *On Physical Adsorption*; John Wiley & Sons: New York, 1964.

(28)   Levenspiel, O. *Chemical Reaction Engineering*; Second ed.; John Wiley & Sons: New York, 1972.

(29)   Cornish-Bowden, A. *Analysis of Enzyme Kinetic Data*; Oxford: New York, 1995.

(30)   Agrawal, A.; Ferguson, W. J.; Gardner, B. O.; Christ, J. A.; Bandstra, J. Z.; Tratnyek, P. G. Effects of Carbonate Species on the Kinetics of 1,1,1-Trichloroethane by Zero-Valent Iron. *Environ. Sci. Technol.* **2002**, *36*, 4326.

(31)   Arnold, W. A.; Roberts, A. L. Pathways and Kinetics of Chlorinated Ethylene and Chlorinated Acetylene Reaction with Fe(0) Particles. *Environ. Sci. Technol.* **2000**, *34*, 1794.

(32)   Duggleby, R. G. Analysis of Enzyme Progress Curves by Nonlinear Regression. *Methods in Enzymology* **1995**, *249*, 61.

(33)   Markus, M.; Hess, B.; Ottaway, J. H.; Cornish-Bowden, A. The Analysis of Kinetic Data in Biochemistry: A Critical Review of Methods. *FEBS Letters* **1976**, *63*, 225.

(34)   Cornish-Bowden, A.; Endrenyi, L. Robust Regression of Enzyme Kinetic Data. *Biochem. J.* **1986**, *234*, 21.

(35)   Reich, J. G. On Parameter Redundancy in Curve Fitting of Kinetic Data. In *Kinetic Data Analysis: Design and Analysis of Enzyme and Pharmacokinetic Experiments*; Endrenyi, L., Ed.; Plenum Press: Toronto, 1981; pp 39.

(36)   Miehr, R.; Tratnyek, P. G.; Bandstra, J. Z.; Scherer, M. M.; Alowitz, M.; Bylaska, E. J. The Diversity of Contaminant Reduction Reactions by Zero-Valent Iron: Role of the Reductate. *Environmental Science and Technology* **2003**, in press.

(37)   Miehr, R.; Bandstra, J. Z.; Po, R.; Tratnyek, P. G. Remediation of 2,4,6-Trinitrotoluene (TNT) by Iron Metal: Kinetic Controls on Product Distributions in Batch and Column Experiments. In *225th National Meeting, 23-27 March 2003*; American Chemical Society: New Orleans, LA, 2003; Vol. 43, No. 1; pp 644.

(38)   Press, W. H.; Flannery, B. P.; Teukolsky, S. A.; Vetterling, W. T. *Numerical Recipes in C. The Art of Scientific Computing*; Cambridge University: Cambridge, England, 1988.

(39)   Arnold, W. A.; Roberts, A. L. Inter- and Intraspecies Competitive Effects in Reactions of Chlorinated Ethylenes with Zero-Valent Iron in Column Reactors. *Environ. Eng. Sci.* **2000**, *17*, 291.

(40)   Schäfer, D.; Köber, R.; Dahmke, A. Competing TCE and *cis*-DCE Degradation Kinetic by Zero-Valent Iron. *J. Contam. Hydrol.* **2003**, *65*, 183.

(41)   Dzombak, D. A.; Fish, W.; Morel, F. M. M. Metal-Humate Interactions. 1. Discrete Ligand and Continuous Distribution Models. *Environ. Sci. Technol.* **1986**, *20*, 669.
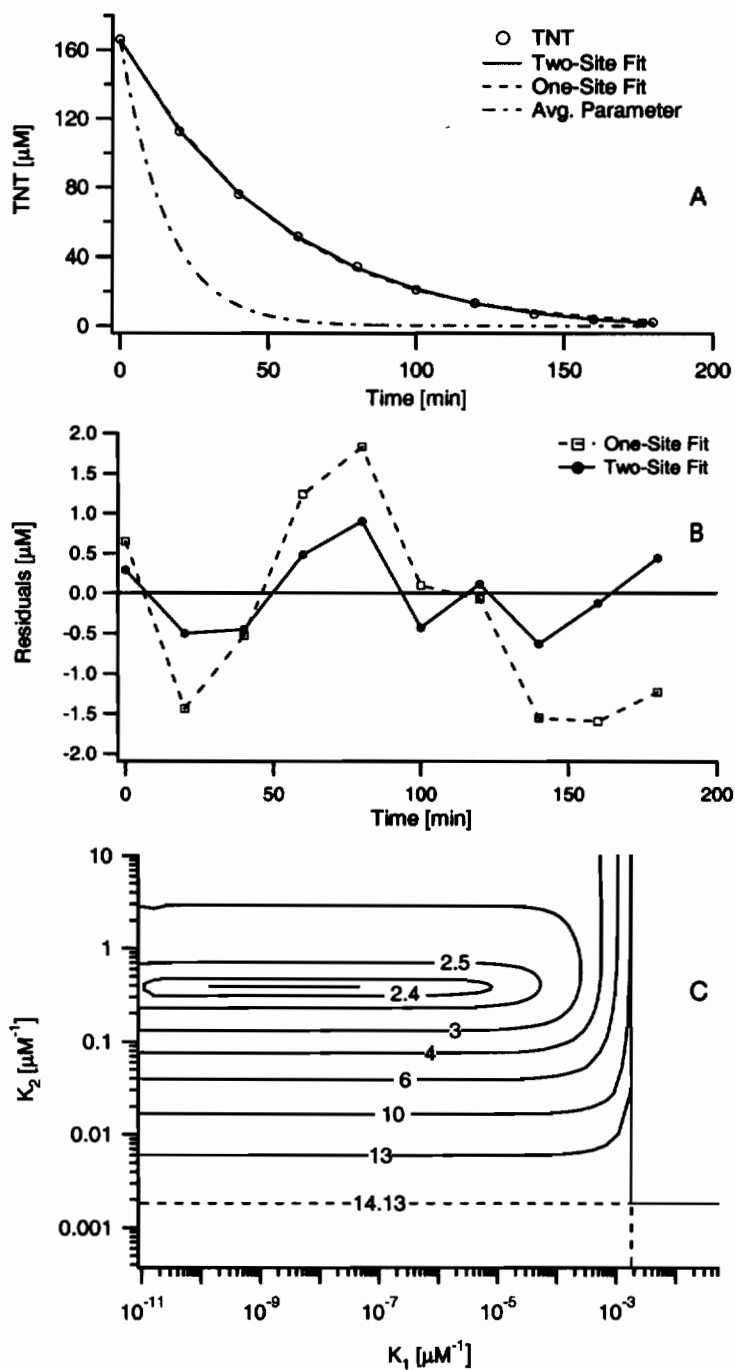
Figure 4.1. Progress curve analysis with one and two-site Langmuir-Hinshelwood models: (A) TNT reduction by iron metal, best fit one and two-site models and the average parameter single-site approximation. (B) Residual plots for the one and two-site fits in A. (C) Contours of constant χ^2 for two-site fits with K_1 and K_2 held. The single-site model is depicted along the bottom and right borders (where $\chi^2 = 14.13$).
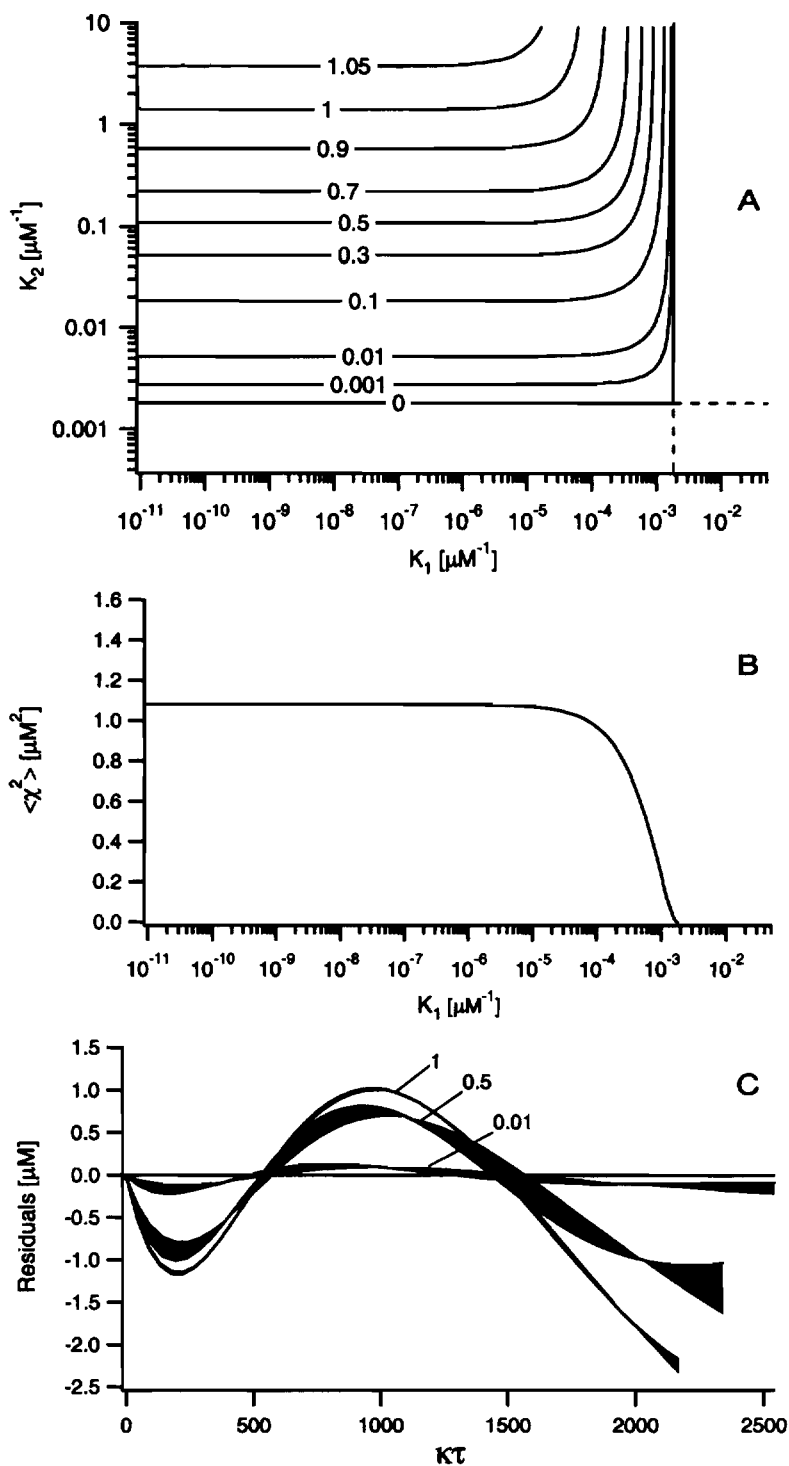
Figure 4.2.   Systematic errors induced by treating a two-site system with a single-site model: (A) χ^2 contours in (K_1, K_2) space. (B) χ^2 in the limit of infinite K_2. (C) All possible residual plots for single-site fits to the two-site models along selected χ^2 contours in A.
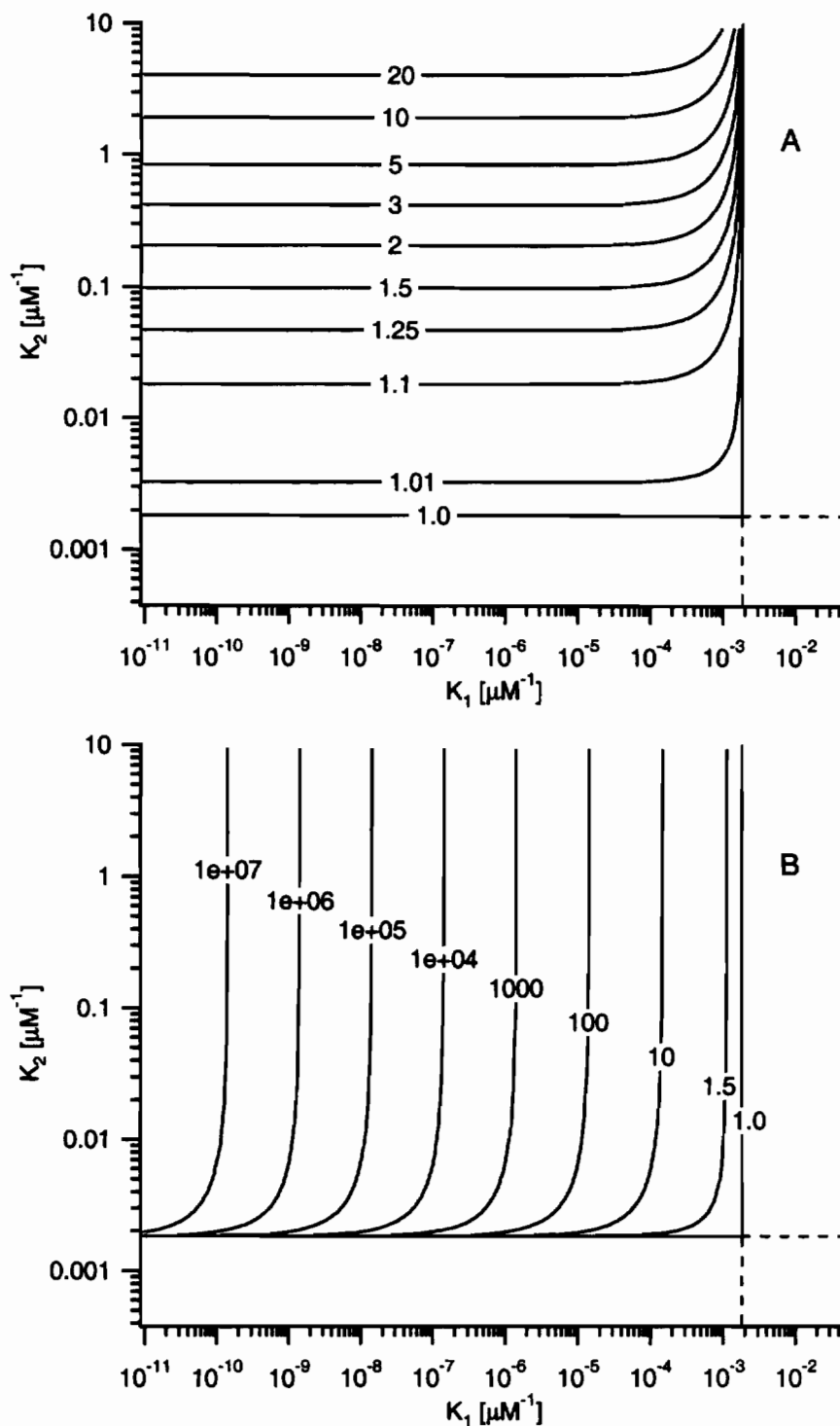
Figure 4.3.   Extrapolation errors induced by treating a two-site system with a single-site model: (A) Ratio of predicted first-order rate constants applicable at low concentrations. (B) Ratio of zero-order rate constants applicable at high concentrations.
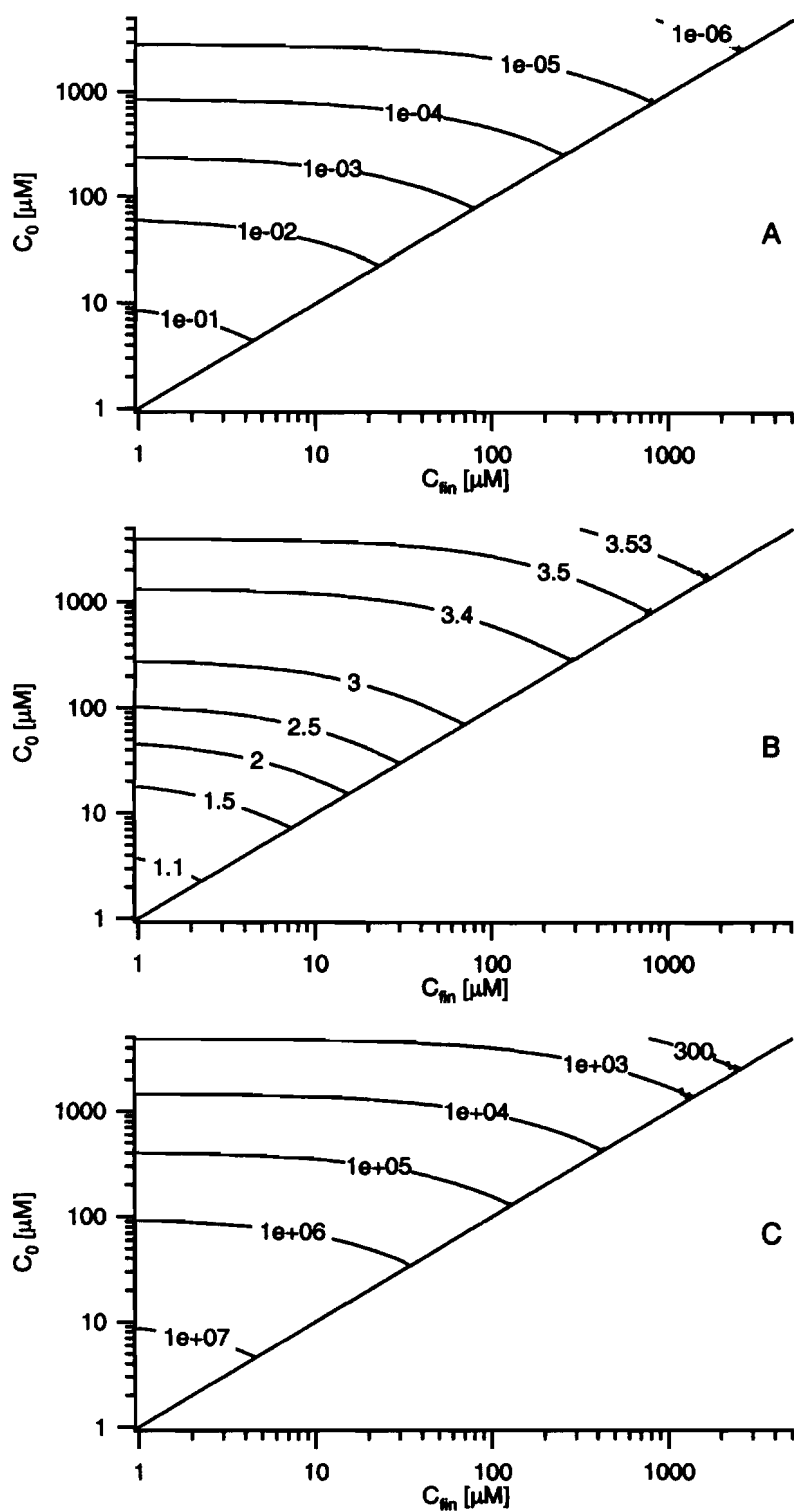
Figure 4.4. Effect of concentration range on the single-site approximation for a (given) two-site system and the systematic errors induced by the approximation: (A) Contours of K^{1-S}_{ss}. (B) Contours of F.O. ratio. (C) Contours of Z.O. ratio.

CHAPTER 5

Reduction of 2,4,6-Trinitrotoluene (TNT) by Iron Metal:
Kinetic Controls on Product Distributions in Batch Experiments[1]

Bandstra, J.Z., R. Miehr, R.L. Johnson, and P.G. Tratnyek. 2005. *Environmental Science & Technology*. 39(1): 230-238.

5.1 Abstract

The reaction kinetics and product distributions for the reduction of 2,4,6-trinitrotoluene (TNT) by granular iron metal (Fe^0) were studied in batch experiments under a variety of initial concentrations of TNT and Fe^0. Although the kinetics of TNT disappearance were found to behave in accord with the standard theory for surface mediated reactions, a complex relationship was found between the initial concentrations of TNT and Fe^0 and the appearance of the expected nitro reduction product, 2,4,6-triaminotoluene (TAT). TNT was completely converted to TAT only when the initial concentration of TNT was low and/or the initial concentration of Fe^0 was high. Mathematical analysis of a range of generic reaction schemes that produce stable end products in addition to TAT showed that (*i*) surface complexation of TAT is insufficient to describe all of our data, and (*ii*) polymerization reactions involving TAT and/or various reaction intermediates are the likely source of the incomplete conversion of TNT to TAT at high initial TNT concentration and low Fe^0 concentration. The relationship between TAT production and reaction conditions is shown to imply that passivation due to reaction products is more likely when the ratio of initial TNT concentration to Fe^0 concentration is high and, therefore, that passivation rates observed at the laboratory scale are likely to be faster than those which would be observed at the field scale.

---

[1] Bandstra, J.Z., R. Miehr, R.L. Johnson, and P.G. Tratnyek. 2005. *Environmental Science & Technology*. 39(1): 230-238.

5.2 Introduction

A decade of intensive research into the kinetics and mechanisms of contaminant reduction by zero-valent iron metal (Fe^0) has led to widespread consensus regarding the primary effects that influence this process. Many of these effects (e.g., contaminant disappearance rate constant, k_{obs}, versus concentration of Fe^0, ρ_m; or k_{obs} vs. initial concentration of contaminant, C_0) can be described with simple quantitative models. These models have been shown to apply over a wide range of contaminants, zero-valent metals, and experimental designs [1]. However, as more high-quality data sets become available, evidence is accumulating for more complex effects that involve interactions among two or more primary effects.

One of the first interactions to be well documented is between the effects of C_0 and mixing rate (e.g., *rpm*) for batch experiments done with azo dyes [2]. In this case, it was shown that site saturation effects—which generally arise as C_0 becomes large—are apparent only at high *rpm*, where mass transport effects are small. Another interaction involving mixing rate is with molecular structure, where it has been shown that mass transport effects on contaminant disappearance kinetics—which generally become more significant at low *rpm*—are apparent only with contaminants for which reaction at the metal surface is comparatively fast (and therefore not rate limiting). Such highly reactive contaminants include nitrobenzene (relative to the carbon tetrachloride) [3] and 1,1,1-trichloroethane (relative to 1,1,2-trichloroethane) [4].

In other cases, interactions arise from competition among parallel reaction pathways or mechanisms. This is likely to be the case for the chlorinated ethenes, which react with Fe^0 by competing pathways (e.g., α- vs. β-dechlorinations) and mechanisms (e.g., electron transfer vs. hydrogen atom transfer). In fact, it has been argued that the relative rates of reduction for trichloroethene (TCE) and perchloroethene (PCE) vary with pH and C_0 in a manner that reflects the combined influence of these factors on the kinetics of hydrogen atom transfer [5]. The nitro aromatics are a similar case, where competing parallel reaction pathways (e.g. nitro reduction vs. coupling) and mechanisms (again, electron transfer vs. hydrogen atom transfer) are likely to produce interactions among primary effects.

Nitro aromatic compounds in general, and TNT in particular, have several properties that make them well suited for probing process-level questions regarding the reactivity of Fe^0. Among these properties is the well-characterized array of parallel and sequential reaction pathways—resulting in mixtures of characteristic products—that occur under reducing conditions. The framework of this array involves the reduction of nitro groups, as shown in scheme 1 for TNT. In scheme 1, each set of three arrows represents the sequential reduction of a nitro group to an amino group via the corresponding nitroso and hydroxylamino intermediates (which are not shown). Some of these intermediates have been detected during reduction of TNT by Fe^0, but the yields have been small and transient [6,7]. Various combinations of the nitroso, hydroxylamino, or amino products can undergo coupling to form dimers or bound residues [8-12], but these products are difficult to extract or identify and have rarely been quantified. 2,4,6-triaminotoluene (TAT) is the most quantifiable product of TNT reduction by Fe^0, but the yield of this product varies widely and this variability has not been explained.
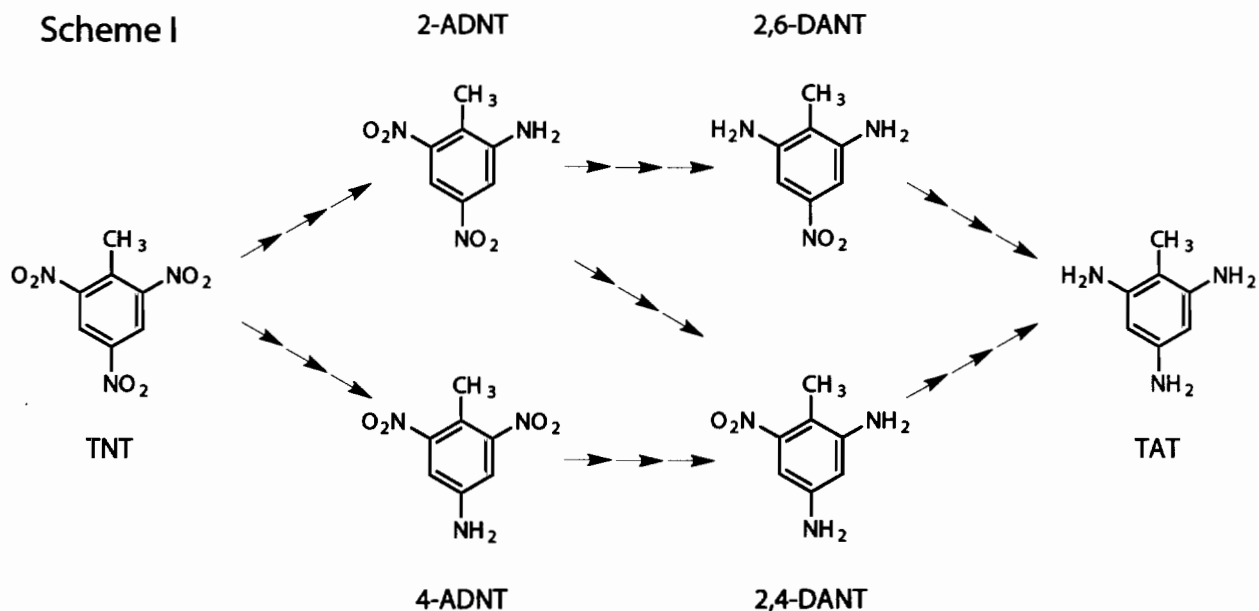
Scheme I

The kinetics of the steps shown in scheme 1 have been described for a variety of reducing systems, including some that contain Fe^0 [6-8,13-15]. For the disappearance of nitro aromatic compounds, a number of standard primary effects have been noted, such as the linear dependence of k_{obs} on ρ_m and $rpm^{1/2}$ [6,8]. The effect of rpm on the rate of nitro benzene reduction has been shown to reflect a mixture of mass transport and surface reaction control [3], which leads to the interaction between effects of rpm and molecular

structure that was noted above. Adsorption could also be rate limiting, although it is difficult to distinguish this from mass transport control with simple batch experiments [7]. Under experimental conditions that minimize the role of mass transport, however, the kinetics of nitro reduction are strongly affected by the presence of competing adsorbates [16].

In contrast to the abundance of detailed analysis on the disappearance kinetics of nitro aromatic compounds under reducing conditions, very little quantitative information is available on the processes that determine the products of this reaction. The data reported by Oh et al. [7,17] are suitable for quantitative kinetic analysis of products from nitro reduction, and their modeling of these data has provided evidence that the type of Fe^0 effects the types of surface sites that are involved in nitro reduction [18]. However, such effects may be coupled to other factors in a manner similar to the examples given above of interactions that reflect parallel and competing reaction pathways. In this study, we describe interactions between ρ_m and C_0 on the distribution of reaction products, using 2,4,6-trinitrotoluene (TNT) as a model for an environmentally-relevant nitro aromatic compound. The results show the rate of TAT appearance and limiting amount of TAT that appears in solution are dependent on ρ_m and C_0 in a manner that suggests a strong influence of polymerization reactions between reduction intermediates and/or TAT; which, in turn, are influenced by other variables such as pH of the solution or composition of the oxide film on the Fe^0. Such complex interactions have implications for interpretation of data from controlled experiments in the laboratory and for the design and performance evaluation of full-scale remediation operations in the field.

5.3 Methods

2,4,6-Trinitrotoluene (TNT) was purchased from ChemService (West Chester, PA); 2-amino-4,6-dinitrotoluene (2-ADNT) and 4-amino-2,6-dinitrotoluene (4-ADNT) were purchased from Sigma/Supelco (Bellefonte, PA); 2,4-diamino-6-nitrotoluene (2,4-DANT), 2,6-diamino-4-nitrotoluene (2,6-DANT), and 2,4,6-triaminotoluene (TAT) were purchased from AccuStandard (New Haven, CT). All chemical standards were >99% purity and used as received.

Granular Fe^0 was obtained from Peerless Powders and Abrasives (Detroit, MI, "PMP Traditional" Size 8/50, >90%). To remove fines, this material was sieved to the

18-35 mesh size fraction. When not in use, the Fe^0 was stored in a vacuum desiccator. Only one batch of Fe^0 was prepared, and all analyses were performed with subsamples from this preparation. The specific surface area, determined by BET N_2 gas adsorption, was 1.54 $m^2 g^{-1}$.

Batch experiments were conducted under anoxic conditions in 60 mL serum bottles containing 1, 2, 3, and 6 g Fe^0 which corresponds to 17, 33, 50, and 100 g L^{-1}, respectively. The bottles were filled with deoxygenated deionized water (no buffer, no headspace), sealed, and mixed by rotation at 20 rpm with the plane oriented 85 degrees from horizontal. The Fe^0 was preconditioned in this environment for 2 days to stabilize geochemical and Fe^0 surface conditions [15,19]. Then, the bottles were spiked with TNT stock solution to begin the reaction. Initial TNT concentrations were varied between 4 and 352 μM. Measurements of pH in bottles containing the same Fe^0 concentrations used in the kinetic experiments after two days pre-exposure gave a pH profile beginning at pH $\approx$ 9.4 at 17 g L^{-1} and increasing to pH $\approx$ 9.9 at 100 g L^{-1} (data not shown).

Periodically, 400 μL samples were withdrawn from the bottles, filtered through a 0.45-μm nylon filter, and analyzed by HPLC using a Platinum C-18 column (Alltech, Deerfield, IL). The mobile phase used for analysis of TNT and intermediates was 55:45 methanol/water at a flow rate of 0.9 mL min^{-1}, whereas TAT analysis was conducted with 5:95 methanol/ammonium acetate buffer (50 mM, pH 7) at a flow rate of 0.7 mL min^{-1}. In all cases, TNT and products were monitored at 254 nm.

Radio labeled experiments were performed by replacing the TNT stock solution with a solution of ^{14}C-labeled TNT (Perkin-Elmer Life Sciences, 1.48 GBq / mmol). Concentration data for ^{14}C-labeled batch experiments were collected in the same manner as the unlabeled experiments. ^{14}C-activity was determined by mixing 0.3 mL of sample with 5 mL ScintiVerse Scintillant (Fisher, Fairlawn, NJ) and measuring total decays with a liquid scintillation counter. In some of the cases where solution phase radioactivity at the end of the experiment was substantially lower than at the beginning, the supernatant was adjusted to pH 5 by adding concentrated hydrochloric acid and concentrations and radioactivity were reanalyzed as described above.

Sequential extractions were performed with ^{14}C-labeled TNT under anoxic conditions in 53 mL centrifuge vials. A centrifuge vial containing 5 g of Peerless Fe^0 was

filled with deionized water and 0.2 mL ^{14}C-TNT stock solution resulting in an initial concentration of 264 µM. After mixing for 24 hours the supernatant was removed and the Fe^0 was washed once with methanol. 5 mL of the respective solvent was then added to the Fe^0, mixed for 24 hours, and separated by centrifugation. The extraction solvents, in order of application, were acetonitrile, NaOH (pH 11), EDTA (pH 11), HCl (pH 4), and EDTA (pH 3).

5.4 Results

5.4.1 Kinetic Experiments and Data Fitting

Concentration time series collected from batch experiments (e.g., Figure 5.1) showed that TNT is reduced to TAT with some of the known intermediates in this reaction sequence appearing briefly at low concentrations. These results are consistent with previous studies that have examined the reaction mechanism of nitro-aromatic reduction [8] and the relative abundance of the intermediate species [7].

Analyses performed after 24 hours of reaction indicate that TNT and all reactive intermediates were entirely consumed and that TAT was a stable end-product. In a number of cases (Figures 5.2-5.3), the final TAT concentration was significantly less than the initial TNT concentration. Experiments with radio labeled TNT showed that the mass imbalance was not due to products in the solution phase (c.f., ^{14}C-labeled data in Figure 5.1). This is consistent with the finding that reduction products of nitro-aromatic compounds adsorb to the Fe^0 surface [16]. However, decreasing the pH to 5 by addition of HCl at the end of an experiment did not release a significant additional quantity of TAT, and serial extraction experiments yielded only a few percent of the missing radio-activity (data not shown). These results indicate that some of the reaction products were irreversibly bound to the Fe^0 surface.

We found the kinetics of TNT disappearance to be accurately described with a first-order rate law:

$$\frac{d[\text{TNT}]}{dt} = -k_{\text{TNT}}[\text{TNT}] \tag{1}$$

where k_{TNT} is the observed first-order rate constant. Preliminary experiments with low ρ_m (13 g Fe^0 L^{-1}, data not shown) exhibited a steep initial drop followed by slower first-order

disappearance of TNT. This bimodal behavior is consistent with mixed control of the kinetics by reversible formation of a reactive surface complex (i.e., by mass transport and/or adsorption) and irreversible surface transformations [7]. To minimize complications due to this bimodal behavior and to achieve appreciable yields of TAT, we chose to focus on relatively high ρ_m, which produces mass transport and/or sorption limited behavior.

The observed kinetics of TAT appearance could also be described with a first-order rate law:

$$\frac{d[TAT]}{dt} = k_{TAT}TAT_{\infty}\exp(-k_{TAT}t) \tag{2}$$

where k_{TAT} is a first-order rate constant, TAT_{∞} is the concentration of TAT at $t \to \infty$, and $TAT_{\infty}\exp(-k_{TAT}t)$ represents the disappearance of a parent compound from which TAT is produced. The TAT appearance data show only a small amount of the positive concavity that is expected during the early stages of a reaction that proceeds through intermediate compounds. This suggests that the rate limiting process for TAT appearance is the disappearance of TNT.

We fit analytical solutions for the rate laws, obtained by direct integration of eqs 1-2, to the TNT and TAT data using Levenberg-Marquardt square error minimization [20]. In all cases, the total concentration (TNT_0 or TAT_{∞}) and rate constant (k_{TNT} or k_{TAT}) where treated as fitting parameters. Since TAT_{∞} did not always complete the mass balance, we fit the TNT disappearance and TAT appearance kinetics as independent processes so that TAT_{∞} need not equal TNT_0 and k_{TAT} need not equal k_{TNT}. The results are tabulated as Supporting Information (Table A1), and some of the fitted time courses are shown in Figures 5.2-5.3.

5.4.2 Effect of Initial Conditions

By performing batch experiments with different Fe^0 concentrations, ρ_m, and initial TNT concentrations, TNT_0, we explored the effects of reaction conditions on the kinetics of TNT reduction and on the appearance of reduction products. Given the likely presence of reduction products bound to the Fe^0 surface [7,16,21] and the implications of this bound residue for long term reactivity of the Fe^0, we designed our experiments to highlight mass balance (i.e., TAT appearance).

Figure 5.2 shows the results of batch experiments at $TNT_0 = 176$ μM with $\rho_m = 17, 33, 50$, and 100 g L^{-1}. Consistent with the surface mediated nature of the reaction, the rate of TNT disappearance increases with ρ_m. TAT appearance, however, responds to ρ_m in an unexpected fashion. TAT_∞ is close to zero for $\rho_m \leq 33$ g L^{-1} (Figure 5.2A) but increases to give nearly complete mass balance at $\rho_m = 100$ g L^{-1} (Figure 5.2D). This effect is inconsistent with simple partitioning of TAT onto the Fe^0 surface, because a larger surface area would sequester more TAT, not less.

Figure 5.3 shows experiments performed at $\rho_m = 50$ g L^{-1} with $TNT_0 = 3.5, 35, 176$, and 352 μM. The data in Figure 5.3 indicate that, in contrast to our previous findings [6], TNT disappearance rates decreased only slightly with increasing TNT_0. The difference between this result and our previous result is probably due to differences in the kinetic regime under which the experiments were performed. The current work was performed under mass transport or sorption limited conditions, so we do not expect to see the influence of accumulation of adsorbed products that has been reported previously [6].

The data in Figure 5.3 indicate a non-linear relationship between TAT appearance and TNT_0. TNT is mostly converted to solution phase TAT when $TNT_0 \leq 35$ μM (Figure 5.4A-B), but a significant portion of the TNT is unaccounted for when $TNT_0 \geq 176$ μM (Figure 5.4C-D). The same trend was observed in batch data with $\rho_m = 17$ g L^{-1}, which gave $TAT_\infty \approx TNT_0$ only at $TNT_0 = 3.5$ μM and in batch data with $\rho_m = 100$ g L^{-1}, which gave $TAT_\infty \approx TNT_0$ for all cases except $TNT_0 = 352$ μM (time courses for these experiments not shown).

The trend of decreasing mass balance with increasing TNT_0 suggests that the capacity of Fe^0 to produce TAT can be overwhelmed by increasing TNT_0. One explanation for this could be passivation of the Fe^0 surface by TNT reduction products, thereby preventing further reaction and causing the accumulation of undetected intermediate species. Respike experiments, however, indicated that, while some passivation occurred, the Fe^0 was still reactive towards TNT, both in the sense of TNT disappearance and in the sense of TAT appearance (data not shown). The processes that yield incomplete mass balance must, therefore, produce stable end-products and leave the

Fe^0 at least partially reactive. Identification of processes that meet these criteria is the principal subject of the remainder of this work.

5.4.3 Quantitative Analysis

Figures 5.4-5.5 depict, in graphical form, the fitting results described above and tabulated in the supporting information. The plot of k_{TNT} against ρ_m (Figure 5.4A) shows a linear relationship, as has been reported previously for TNT [6] and many other contaminants [22,23]. The slope of this line gives the surface area normalized rate constant, $k_{SA} = 2.03 \pm 0.10 \times 10^{-3}$ min^{-1} m^{-2} L. This value reflects the range of TNT_0 that were included in the calculation, even though—as noted above—high TNT_0 experiments produce slightly lower rate constants than low TNT_0 experiments (probably due to the increased influence of surface reaction kinetics for the high TNT_0 experiments). The value of k_{SA} reported here is about twice the value that we have reported previously for Peerless Fe^0 [6,15], but is well within the range of k_{SA}'s that we reported previously for similar types of Fe^0 and the range of k_{SA}'s for TNT and Fe^0 that have been reported by others [6,15].

A plot of k_{TAT} vs. ρ_m (Figure 5.4B) shows features that cannot be explained on the basis of the standard theory for surface mediated chemical kinetics. For each value of TNT_0, $k_{TAT} \approx 0$ at low ρ_m but increases linearly above some ρ_m. The slope of the increase appears to decrease with increasing TNT_0 and the ρ_m beyond which k_{TAT} increases appears to be larger for higher values of TNT_0. A linear relationship between k_{TAT} and ρ_m could arise if the rate of TAT appearance is controlled by TNT disappearance. If this were the case, however, the linear relationship would hold even at low ρ_m and the slope would be independent of TNT_0.

Comparing k_{TAT} to our fitted values of TAT_∞ (Figure 5.4C) reveals a relationship between these parameters. This could either indicate that the processes causing TAT_∞ to be less than TNT_0 are occurring throughout the course of the reaction, or simply that the fitting parameters k_{TAT} and TAT_∞ are covariant. Of the two parameters, TAT_∞ is more robust because it is largely independent of modeling details (e.g., order of reaction); in fact, nearly identical TAT_∞ values to those found by first-order fitting could be obtained by taking the average value of the last few TAT points in the relevant time series.

Therefore, we chose to analyze the variables controlling TAT appearance (and the behavior of k_{TAT} noted above) using TAT_∞ as the dependent variable, rather than k_{TAT}.

Figure 5.5 shows TAT_∞ plotted against ρ_m and TNT_0. TAT_∞ increases with respect to each of these variables but, in most cases, TAT_∞ appears to approach a horizontal asymptote (which, if the slope is everywhere positive, is expected since $TAT_\infty \leq TNT_0$). In the case of ρ_m (Figure 5.5A), the value of the asymptote is TNT_0, while for TNT_0 (Figure 5.5B) the asymptotic value appears to be a function of ρ_m. In general, to approach a horizontal asymptote with positive slope, a function must have negative concavity. This feature is apparent in the plot of TAT_∞ vs. TNT_0 (Figure 5.5B), but is less apparent in the plot of TAT_∞ vs. ρ_m (Figure 5.5A) where the 176 µM and the 352 µM data display mostly positive concavity, especially for $\rho_m < 50$ g L^{-1}. Since we expect the TAT_∞ vs. ρ_m curve to approach TNT_0 as $\rho_m \rightarrow \infty$, the curve must have an inflection point; i.e., a ρ_{crit} below which little TAT is produced and above which nearly all TNT is converted to TAT.

Both the positive slope of TAT_∞ with respect to ρ_m and the negative concavity with respect to TNT_0 are inconsistent with significant adsorption of nitro reduction products in contrast to previous suggestions [16]. As noted above, adsorption would be expected to produce $\partial TAT_\infty / \partial \rho_m < 0$, because increasing the adsorbent concentration (i.e., ρ_m) would increase the amount of TAT that is adsorbed. At constant ρ_m, adsorption would be expected to produce $\partial TAT_\infty / \partial TNT_0 > 0$ (as is observed) because increasing TNT_0 would increase the adsorbed concentration. Adsorption would, however, produce TAT_∞ vs. TNT_0 profiles with zero concavity at both low TNT_0 where a linear isotherm would be expected and high TNT_0 where saturation of adsorption sites would occur. Since, under an adsorption mechanism, the slope of the low TNT_0 portion of the curve would be < 1 while the slope of the high TNT_0 region would be = 1, the transition from linear adsorption to site saturation behavior would display positive concavity. This is in contrast to the data in Figure 5.5B which appear to possess a slope = 1 at low TNT_0 and a concave down transition to slope ≈ 0 at high TNT_0.

5.5 Modeling

5.5.1 Scenarios leading to incomplete mass balance

In order to produce the partial mass balances that we observed, there must be reaction pathways that do not lead to TAT or reactions that involve the transformation of TAT to undetected products. These processes can be arranged into three scenarios: branching, partitioning, and coupling (scheme 2).

Branching

$$\begin{array}{c} \boxed{\begin{array}{c} \text{UNK} \\ \uparrow \end{array}} \\ \text{TNT} \rightarrow \boxed{\text{INT}} \rightarrow \text{TAT} \boxed{\rightleftharpoons \text{UNK}} \\ \boxed{\begin{array}{c} \downarrow \\ \text{UNK} \end{array}} \\ \textit{Coupling} \end{array}$$
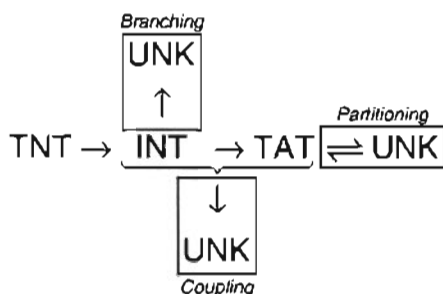
Scheme 2

Where INT denotes a generic and/or lumped intermediate (which could include the various intermediates shown in scheme 1 as well as TNT) and UNK represents undetected (unknown) products—most likely residing on the Fe^0 surface—that are responsible for the incomplete mass balance that we often observed. In the following analysis we employ the subscripts "Branch", "Couple", and "Partition" to denote the source a specific UNK species. No subscript is used when a statement applies to all three processes.

The branching scenario involves the formation of a product (or products) from the milieu of intermediates that (during the time course of our experiments) does not react further to form TAT. To produce incomplete mass balance, the branching reaction must be irreversible on the time scale of our experiments. Physically, a branching reaction might arise in this system due to coupling of nitroso- with hydroxylamino-intermediates, forming a polymeric substance that is likely to be sequestered on the Fe^0 surface [24].

In the coupling scenario, TAT reacts with INT and, once all the INT is gone, the reaction stops, leaving the remaining TAT unreacted. This scenario could arise in a polymerization reaction similar to that leading to a branching scenario but with TAT as one of the reactants [8]. The branching scenario is, formally, a subset of the coupling scenario. However, since the coupling scenario involves the added complexities associated with a feedback loop, we chose to analyze the two as separate cases.

In the partitioning scenario, TAT undergoes further reaction to form undetected species. The reaction, in this scenario, must be reversible, otherwise TAT would disappear entirely. Such a scenario could arise from the reversible sorption of TAT to the Fe^0 surface. Since we have already noted that adsorption can not explain all aspects of our data, we have included the partitioning scenario mainly for completeness. However, we note that other reversible reactions involving TAT could exist, the character of which we address later.

In order to define models for TAT appearance based on the three scenarios represented in scheme 2, we require that the models conform to the following criteria, which derive from our discussion of the trends represented in Figure 5.5.

$$\frac{\partial TAT_\infty}{\partial \rho_m} \geq 0 \tag{3}$$

$$\frac{\partial^2 TAT_\infty}{\partial \rho_m^2} \begin{cases} \geq 0 & \rho_m < \rho_{crit} \\ = 0 & \rho_m = \rho_{crit} \\ \leq 0 & \rho_m > \rho_{crit} \end{cases} \tag{4}$$

$$\frac{\partial TAT_\infty}{\partial TNT_0} \geq 0 \tag{5}$$

$$\frac{\partial^2 TAT_\infty}{\partial TNT_0^2} \leq 0 \tag{6}$$

Rate equations can be developed for each of the regimes shown in scheme 2 by assuming reaction rates that are proportional to the concentrations of the reacting species (including, where appropriate, the reactive surface area). Owing to their linearity, the rate equations produced by this procedure do not meet the criteria of eqs 3-6. The goal of modeling analysis that follows is to determine what modifications must be made to the standard rate equations in order to satisfy the above criteria and, in particular, to determine whether recourse must be made to factors that are not explicitly depicted in scheme 2 (e.g., effects of pH or $[Fe^{2+}]$ in solution).

5.5.2 Branching

A model for the branching scenario can be written by assuming that the rates of TAT and UNK_{Branch} formation obey a power law in INT concentration with rate constants that depend on ρ_m [25-29]:

$$\frac{d[INT]}{dt} = f_{TNT \to INT}(t) - k_{TAT}(\rho_m) \, [INT]^{m_{TAT}} - k_{UNK}(\rho_m) \, [INT]^{m_{UNK}} \tag{7}$$

$$\frac{d[TAT]}{dt} = k_{TAT}(\rho_m) \, [INT]^{m_{TAT}} \tag{8}$$

$$\frac{d[UNK_{Branch}]}{dt} = k_{UNK}(\rho_m) \, [INT]^{m_{UNK}} \tag{9}$$

where $f_{TNT \to INT}(t)$ is a generic function representing the production of INT, k's are rate constants, m's are the orders of reaction with respect to INT, and all concentrations are initially zero. The parameter subscripts in eqs 7-9 correspond to the product of the relevant reaction so that, for instance, m_{TAT} is the INT reaction order for the INT $\to$ TAT reaction. This notation is employed throughout the rest of the paper. If we assume that $m_{TAT} = m_{UNK}$ we can derive a formula for TAT_∞ by integrating the ratio of the rate of TAT production to the rate of UNK_{Branch} production from $t = 0$ to $t = \infty$ (details given in the Supporting Information).

$$TAT_\infty = TNT_0 \frac{\kappa(\rho_m)}{1 + \kappa(\rho_m)} \tag{10}$$

Where $\kappa = k_{TAT} / k_{UNK}$. Eq 10 satisfies eq 3 if and only if $\partial \kappa / \partial \rho_m > 0$ (proof given in Supporting Information) implying that the rates of processes leading to TAT must increase with ρ_m faster than the rates of processes leading to UNK_{Branch}. Eq 10 satisfies eq 4 if and only if $\partial^2 \kappa / \partial \rho_m^2 > 0$ for $0 < \rho_m \le \rho_{crit}$, where ρ_{crit} is the inflection point in TAT_∞ vs. ρ_m (Figure 5.5A) implying that the concavity of k_{TAT} with respect to ρ_m must be large compared to the concavity of k_{UNK} (proof given in Supporting Information).

Eq 10 is linear with respect to TNT_0 and, therefore, does not satisfy eq 6. This is a result of the assumption, used in deriving eq 10, that $m_{TAT} = m_{INT}$. To see this, we assume that $f_{TNT \to INT}(t)$ in eq 7 is a Dirac-δ style pulse (modulated by TNT_0) at t = 0 such that eq 7 becomes:

$$\frac{d[INT]}{dt} = -k_{TAT}(\rho_m) [INT]^{m_{TAT}} - k_{UNK}(\rho_m) [INT]^{m_{UNK}}$$ (11)

with the initial condition

$$[INT]_{t=0} = TNT_0$$ (12)

which is equivalent to assuming that the branching occurs at TNT rather than at INT. Integrating eq 6 from $t = 0$ to $t = \infty$ and substituting eq 11 on the right hand side yields a relationship for TAT_∞ (details given in the Supporting Information).

$$TAT_\infty = \int_0^{TNT_0} \frac{\kappa(\rho_m)}{\kappa(\rho_m) + w^{\Delta m}} dw$$ (13)

Where $\kappa = k_{TAT} / k_{UNK}$, $\Delta m = m_{UNK} - m_{TAT}$, and the dummy variable, w, has been substituted for [INT]. Eq 13 reduces to eq 10 when $m_{UNK} = m_{TAT}$ and satisfies eq 5 for all κ, m_{UNK}, and m_{TAT}. Eq 6 is satisfied if and only if $m_{UNK} > m_{TAT}$ (proof given in Supporting Information), therefore, the rates of processes leading to UNK_{Branch} must increase with INT concentration faster than the rates of processes leading to TAT.

5.5.3 Coupling

A model can be written for the coupling scenario in a fashion similar to the branching scenario with the addition of a TAT concentration dependence to the rate of UNK_{Couple} formation.

$$\frac{d[INT]}{dt} = f_{TNT \to INT}(t) - k_{TAT}(\rho_m) [INT]^{m_{TAT}} - v_{INT} k_{UNK}(\rho_m) [TAT]^{n_{TAT}} [INT]^{m_{UNK}}$$ (14)

$$\frac{d[TAT]}{dt} = k_{TAT}(\rho_m) [INT]^{m_{TAT}} - v_{TAT} k_{UNK}(\rho_m) [TAT]^{n_{TAT}} [INT]^{m_{UNK}}$$ (15)

$$\frac{d[UNK_{Couple}]}{dt} = v_{UNK} k_{UNK}(\rho_m) [TAT]^{n_{TAT}} [INT]^{m_{UNK}}$$ (16)

where v_{TAT}, v_{INT}, and v_{UNK} are stoichiometric factors such that

$$TNT_0 = [TNT] + [TAT] + [INT] + \frac{v_{INT} + v_{TAT}}{v_{UNK}} [UNK_{Couple}]$$ (17)

and n_{TAT} is the order of the coupling reaction with respect to TAT. Setting $n_{TAT} = 0$ and $v_{TAT} = 0$ gives the branching model described above. In the case where $m_{UNK} = m_{TAT}$ an

equation for TAT_∞ can be found by dividing eq 15 by eq 16 and integrating the result (details given in Supporting Information).

$$\frac{TNT_0 - TAT_\infty}{V_{INT} - V_{TAT}} = \int_0^{TAT_\infty} \frac{w^{n_{TAT}}}{\kappa(\rho_m) - V_{TAT} w^{n_{TAT}}} dw \tag{18}$$

where $\kappa = k_{TAT} / k_{UNK}$ and w has been substituted for [TAT]. Eq 18 satisfies eqs 3-4 if and only if $\partial \kappa / \partial \rho_m > 0$ and $\partial^2 \kappa / \partial \rho_m^2 > 0$ (proof given in Supporting Information). Eq 18 satisfies eqs 5-6 for any $n_{TAT} > 0$. The coupling model, therefore, has the same essential features with respect to ρ_m as the branching model but produces the observed behavior with respect to TNT_0 without need for non-linearity in the INT reaction orders. The required non-linearity is supplied by the TAT term in the UNK_{Couple} formation rate indicating that both non-linearity in the reaction order of individual species and non-linearity in the overall order of reaction can give the behavior that we observed in Figure 5.5B.

5.5.4 Partitioning

We can derive a model for the partitioning scenario by assuming equilibrium conditions between TAT and $UNK_{Partition}$ with a partitioning coefficient, κ^{-1}, that depends on ρ_m.

$$\frac{1}{\kappa(\rho_m)} = \frac{\left(\frac{m_{TAT}}{m_{UNK}}\right)^{m_{TAT}} (TNT_0 - TAT_\infty)^{m_{TAT}}}{TAT_\infty^{m_{UNK}}} \tag{19}$$

m_{TAT} and m_{UNK} are stoichiometric factors and a mass balance condition has been applied to obtain the right hand side of eq 19. In the absence of non-linearity (i.e., $m_{TAT} = m_{UNK}$), eq 19 reduces to the same form as eq 10.

$$TAT_\infty = TNT_0 \frac{\kappa(\rho_m)^{1/m}}{1 + \kappa(\rho_m)^{1/m}} \tag{20}$$

where $m = m_{TAT} = m_{UNK}$. As with the branching and coupling scenarios, κ can be interpreted as a ratio of rate constants, $\kappa = k_{UNK \to TAT} / k_{TAT \to UNK}$. Eq 19 satisfies eqs 3-4 if and only if $\partial \kappa / \partial \rho_m > 0$ and $\partial^2 \kappa / \partial \rho_m^2 > 0$ (proof given in the Supporting Information) indicating that the partitioning reaction must be shifted toward TAT with increasing ρ_m

and that the shift must be stronger (i.e. higher order) than linear. Differentiation of eq 19 with respect to TNT_0 shows that the partitioning model will satisfy eq 5 for any values of m_{TAT} and m_{UNK}, but eq 6 will be satisfied if and only if $m_{UNK} > m_{TAT}$ (proof given in Supporting Information), indicating that nonlinearity plays the same role for the partitioning scenario as it does for the branching and coupling scenarios.

5.5.5 Fitting

We parameterized the models presented above by non-linear square error minimization using both a single variable approach and a multivariate approach. In the single variable approach, the TAT_∞ vs. ρ_m data with the same TNT_0 were fitted together and, separately, the TAT_∞ vs. TNT_0 data with the same ρ_m were fit together. In the multivariate approach, TAT_∞ is treated as a function of both ρ_m and TNT_0, and all TAT_∞ data were treated together.

The TAT_∞ vs. TNT_0 data (Figure 5.5B) were fit by treating $\kappa(\rho_m)$ as an adjustable parameter. To fit the TAT_∞ vs. ρ_m data, however, the functional form of $\kappa(\rho_m)$ must be assumed. One way to interpret the dependence of the rate constants and partition coefficient on ρ_m is to treat Fe^0 surface sites as reactants and, therefore, to assume that reaction rates obey a power law with respect ρ_m [28,29].

$$\kappa(\rho_m) = \kappa \, \rho_m^{\Delta\lambda} \tag{21}$$

Where $\kappa = k_{TAT} / k_{UNK}$ (as in eq 10 but with the ρ_m dependence factored out), $\Delta\lambda = \lambda_{TAT} - \lambda_{UNK}$, and λ is the order of each reaction with respect to reactive surface area. The conditions given above imply that, for each of the three models, $\Delta\lambda > 1$.

Under the power law assumption, a fitting equation can be derived for TAT_∞ vs. ρ_m (Figure 5.5A) from eq 10 for branching.

$$TAT_\infty = TNT_0 \frac{\kappa \rho_m^{\Delta\lambda}}{1 + \kappa \rho_m^{\Delta\lambda}} \tag{22}$$

To achieve the sharp increase in TAT_∞ that we observed in the data, it was necessary to set $\Delta\lambda$ to fairly large values (6.7 for 176 μM, 3.6 for 352 μM). Since $\lambda_{UNK} \geq 0$, this result indicates that λ_{TAT} must be significantly greater than 1. It is reasonable to expect the INT $\rightarrow$ TAT reaction to depend on ρ_m, but values of $\lambda_{TAT} \gg 1$ are physically unrealistic. If

we set $\lambda_{TAT} = 1$ and $\lambda_{TAT} = 0$, the model does not reproduce the positive concavity and inflection point that are shown in Figure 5.5A. Adding non-linearity to the concentration dependence of the reaction rates (i.e., by employing eq 13 or 18) does not significantly decrease the value of $\Delta\lambda$ needed to replicate the TAT_∞ vs. ρ_m data. This is not surprising because the conditions that were derived for $\kappa(\rho_m)$ do not depend on the values of the INT or TAT reaction orders.

Although the application of a power law expression accurately reproduces the behavior of TAT_∞ vs. ρ_m, the values of the fitted parameters indicate that additional chemical factors—factors indirectly influenced by ρ_m—must be involved in determining the distribution of material between TAT and UNK_{Branch} (or UNK_{Couple}). Since $\lambda_{TAT} = 1$ is consistent with our analysis, we hypothesize that, while the rate of the INT $\rightarrow$ TAT reaction is adequately modeled with a power law expression, the rate of the INT $\rightarrow$ UNK_{Branch} (or UNK_{Couple}) reaction depends on solution chemistry. Given the acid/base catalyzed nature of many polymerization reactions [24,30], it seems likely that pH may be influencing TAT appearance, though we can not rule out other factors such as $[Fe^{2+}]$.

The character of the partitioning scenario can be investigated by deriving a fitting equation from eq 19 under a power law assumption for the partition coefficient κ^{-1}. In the case of $m_{UNK} = m_{TAT} = 1$, the fitting equation is identical to eq 22 and, therefore, the fitting results for the branching scenario also apply to the partitioning scenario. In this case, the large values obtained for $\Delta\lambda$ imply that the reaction order with respect to ρ_m for the $UNK_{Partition} \rightarrow$ TAT reaction is significantly greater than that for the TAT $\rightarrow$ $UNK_{Partition}$ reaction, which is the opposite of what would be expected if adsorption of TAT to the Fe^0 surface was controlling TAT_∞. Modifying the ρ_m dependence to involve additional chemical factors (as we suggested for the branching scenario) could also be done for the adsorption model. Such a modification, however, would have to be strong enough to overcome the tendency for more material to adsorb to more adsorbent, making the success of such a modification unlikely.

Eq 13 for branching, eq 18 for coupling, and eq 19 for partitioning can each be fit to the TAT_∞ vs. TNT_0 data by treating κ as an adjustable parameter. All three scenarios were capable of fitting the data equally well. In each case, the sharpness of the transition

from $TAT_\infty = TNT_0$ to a horizontal asymptote increased with the degree of non-linearity (i.e., $\Delta m = m_{UNK} - m_{TAT}$ in eqs 7-20 and/or n_{TAT} in eq 18). The fitting results indicate a sharp transition (e.g., Δm as large as 4.6 for eq 13), but the data are too sparse to produce definitive information about the nature of this transition. The existence of such a transition is, however, clearly indicated by these data, and non-linearity in the TAT disappearance mechanism is sufficient for its description.

Since we expect that, for the branching and coupling models, $m_{TAT} = 1$, the non-linearity in INT reaction orders indicates that the INT $\rightarrow$ UNK reactions are multi-molecular. This is consistent with the interpretation of these reactions as polymerization of the intermediates and/or TAT. At high TNT_0, the concentrations of the intermediates become large and the rate of polymerization increases relative to the rate of TAT production, leading to an overloading of the capacity of the Fe^0 to produce TAT without completely passivating the surface. In the context of the partitioning scenario, the interpretation of Figure 5.5B and the required non-linearity is less clear. As noted above, the observed behavior is not consistent with simple adsorption of TAT to the Fe^0 surface. The non-linearity could be rationalized by assuming that the forward reaction (TAT $\rightarrow$ UNK) is multi-molecular, which could arise if TAT undergoes a reversible coupling reaction with itself.

In total, these results indicate that the processes controlling TAT appearance are a combination of coupling and branching reactions with reaction rates that are sensitive to solution conditions. Lumping these processes into a single model would lead to eqs 14-17 for coupling, of which, eqs 7-9 for branching are a special case. Fitting eq 13 for branching (with eq 21 substituted for κ) to our TAT_∞ data with the multivariate approach shows that the branching scenario is sufficient to describe all of our data. The multivariate fitting results are shown in Figure 5.5. The fitted parameters from the multivariate approach are consistent with the results above that indicate significant nonlinearities in both $\Delta\lambda$ and Δm which may be due to polymerization reactions involving TAT and/or various reaction intermediates.

5.5.6 Implications for Scaling Passivation Kinetics

Aromatic amines inhibit corrosion reactions both by competition for active sites [31] and by polymer film formation [32] and, therefore, the fate of TAT can be expected to effect the longevity of Fe^0 based remediation technologies. To investigate the implications of our results for surface passivation, we can use our modeling results to show how the coverage of surface sites will vary with both TNT_0 and ρ_m. To do this, we assume that UNK precipitates onto active sites to form passive sites and that UNK precipitates onto passive sites with no effect on the reactivity of the site.

$$S_A + UNK \rightarrow S_P$$
$$S_P + UNK \rightarrow S_P$$

<div align="right">Scheme 3</div>

Where S_A and S_P represent active and passive sites, respectively. If the precipitation reactions are fast and occur with equal probability (details given in Supporting Information):

$$\frac{[S_P]}{[S_{Tot}]} = 1 - \exp\left(\alpha \frac{TNT_0 - TAT_\infty}{\rho_m} \right)$$

<div align="right">(23)</div>

Where $[S_P]$ is the concentration of S_P (e.g., moles S_P per liter of solution), $[S_{Tot}]$ is the concentration of total sites ($= [S_A] + [S_P]$), and α is a constant of proportionality between $[S_{Tot}]$ and ρ_m (set to 1 in this work). $[S_P] / [S_{Tot}]$ can be interpreted as the degree of reaction passivation, $k_{obs}|_t / k_{obs}|_{t=0}$. Figure 5.6 shows $[S_P] / [S_{Tot}]$ calculated from eq 23 with TAT_∞ taken from the multivariate fitting of eq 13 to the data in Figure 5.5. The results indicate that significant passivation is likely when TNT_0 / ρ_m is large (i.e., the flat portion of the curves on the left side of Figure 5.6) as is the case in most laboratory investigations of passivation, while systems with small TNT_0 / ρ_m would passivate more slowly. The transition (with respect to both ρ_m and TNT_0) between the two regimes is sharp, implying that the rates of surface passivation found for respike batch experiments [16] and laboratory column experiments [19,33-35] will tend to overestimate the passivation rates that apply to most field conditions.

5.6 Acknowledgments

5.7 Literature Cited

(1)   Tratnyek, P. G.; Scherer, M. M.; Johnson, T. J.; Matheson, L. J. Permeable Reactive Barriers of Iron and Other Zero-Valent Metals. In *Chemical Degradation Methods for Wastes and Pollutants: Environmental and Industrial Applications*; Tarr, M. A., Ed.; Marcel Dekker: New York, 2003; pp 371.

(2)   Nam, S.; Tratnyek, P. G. Reduction of Azo Dyes with Zero-Valent Iron. *Wat. Res.* **2000**, *34*, 1837.

(3)   Scherer, M. M.; Johnson, K.; Westall, J. C.; Tratnyek, P. G. Mass Transport Effects on the Kinetics of Nitrobenzene Reduction by Iron Metal. *Environ. Sci. Technol.* **2001**, *35*, 2804.

(4)   Arnold, W. A.; Ball, W. P.; Roberts, A. L. Polychlorinated Ethane Reaction with Zero-Valent Zinc: Pathways and Rate Control. *J. Contam. Hydrol.* **1999**, *40*, 183.

(5)   Wang, J.; Farrell, J. Investigating the Role of Atomic Hydrogen on Chloroethene Reactions with Iron Using Tafel Analysis and Electrochemical Impedance Spectroscopy. *Environ. Sci. Technol.* **2003**, *37*, 3891.

(6)   Tratnyek, P. G.; Miehr, R.; Bandstra, J. Z. Kinetics of Reduction of TNT by Iron Metal. In *Groundwater Quality 2001: Third International Conference on Groundwater Quality*; IAHS Press: Sheffield, UK, 2002; Vol. No. 275; pp 427.

(7)   Oh, S.-Y.; Cha, D. K.; Kim, B. J.; Chiu, P. C. Effect of Adsorption to Elemental Iron on the Transformation of 2,4,6-Trinitrotoluene and Hexahydro-1,3,5-Trinitro-1,3,5-Triazine in Solution. *Environ. Toxicol. Chem.* **2002**, *21*, 1384.

(8)   Agrawal, A.; Tratnyek, P. G. Reduction of Nitro Aromatic Compounds by Zero-Valent Iron Metal. *Environ. Sci. Technol.* **1996**, *30*, 153.

(9)   Lenke, H.; Achtnich, C.; Knackmuss, H.-J. Perspectives of Bioelimination of Polyaromatic Compounds. In *Biodegradation of Nitroaromatic Compounds and Explosives*; Spain, J. C., Hughes, J. B., Knackmuss, H.-J., Eds.; Lewis: Boca Raton, FL, 2000; pp 91.

(10) Wang, C. Y.; Zheng, D.; Hughes, J. B. Stability of Hydroxylamino- and Amino-Intermediates from Reduction of 2,4,6-Trinitrotoluene, 2,4-Dinitrotoluene, and 2,6-Dinitrotoluene. *Biotechnology Letters* **2000**, *22*, 15.

(11) Ahmad, F.; Hughes, J. B. Reactivity of Partially Reduced Arylhydroxylamine and Nitrosoarene Metabolites of 2,4,6-Trinitrotoluene (TNT) toward Biomass and Humic Acids. *Environ. Sci. Technol.* **2002**, *36*, 4370.

(12) Thorn, K. A.; Kennedy, K. R. 15n Nmr Investigation of the Covalent Binding of Reduced TNT Amines to Soil Humic Acid, Model Compounds, and Lignocellulose. *Environ Sci Technol* **2002**, *36*, 3787.

(13) Burris, D. R.; Hatfield, K.; Wolfe, N. L. Laboratory Experiments with Heterogeneous Reactions in Mixed Porous Media. *J. Environ. Eng.* **1996**, *122*, 685.

(14) Hung, H.-M.; Ling, F. H.; Hoffmann, M. R. Kinetics and Mechanism of the Enhanced Reductive Degradation of Nitrobenzene by Elemental Iron in the Presence of Ultrasound. *Environ. Sci. Technol.* **2000**, *34*, 1758.

(15) Miehr, R.; Tratnyek, P. G.; Bandstra, J. Z.; Scherer, M. M.; Alowitz, M.; Bylaska, E. J. The Diversity of Contaminant Reduction Reactions by Zero-Valent Iron: Role of the Reductate. *Environ. Sci. Technol.* **2004**, *38*, 139.

(16) Devlin, J. F.; Klausen, J.; Schwarzenbach, R. P. Kinetics of Nitroaromatic Reduction on Granular Iron in Recirculating Batch Experiments. *Environ. Sci. Technol.* **1998**, *32*, 1941.

(17) Oh, S.-Y.; Cha, D. K.; Chiu, P. C. Graphite-Mediated Reduction of 2,4-Dinitrotoluene with Elemental Iron. *Environ. Sci. Technol.* **2002**, *36*, 2178.

(18) Jafarpour, Y.; Imhoff, P. T.; Chiu, P. C. Mathematical Modeling of 2,4-Dinitrotoluene Reduction with Iron. In *225th National Meeting, 23-27 March 2003*; American Chemical Society: New Orleans, LA, 2003; Vol. 43, No. 1; pp 638.

(19) Miehr, R.; Bandstra, J. Z.; Po, R.; Tratnyek, P. G. Remediation of 2,4,6-Trinitrotoluene (TNT) by Iron Metal: Kinetic Controls on Product Distributions in Batch and Column Experiments. In *225th National Meeting, 23-27 March 2003*; American Chemical Society: New Orleans, LA, 2003; Vol. 43, No. 1; pp 644.

(20) Press, W. H.; Flannery, B. P.; Teukolsky, S. A.; Vetterling, W. T. *Numerical Recipes in C. The Art of Scientific Computing*; Cambridge University: Cambridge, England, 1988.

(21)   Klausen, J.; Tröber, S. P.; Haderlein, S. B.; Schwarzenbach, R. P. Reduction of Substituted Nitrobenzenes by Fe(II) in Aqueous Mineral Suspensions. *Environ. Sci. Technol.* **1995**, *29*, 2396.

(22)   Matheson, L. J.; Tratnyek, P. G. Reductive Dehalogenation of Chlorinated Methanes by Iron Metal. *Environ. Sci. Technol.* **1994**, *28*, 2045.

(23)   Johnson, T. L.; Scherer, M. M.; Tratnyek, P. G. Kinetics of Halogenated Organic Compound Degradation by Iron Metal. *Environ. Sci. Technol.* **1996**, *30*, 2634.

(24)   Zuman, P.; Shah, B. Addition, Reduction, and Oxidation Reactions of Nitrosobenzene. *Chem. Rev.* **1994**, *94*, 1621.

(25)   Moore, J. W.; Pearson, R. G. *Kinetics and Mechanism*; 3rd ed.; Wiley: New York, 1981.

(26)   Hougen, O. A.; Watson, K. M. *Chemical Process Principles*; J. Wiley & Sons, inc.: New York, 1943.

(27)   Hougen, O. A.; Watson, K. M. Solid Catalysts and Reaction Rates. *Industrial and Engineering Chemistry* **1943**, *35*, 529.

(28)   Levenspiel, O. *Chemical Reaction Engineering*; Second ed.; John Wiley & Sons: New York, 1972.

(29)   Levenspiel, O. Chemical Reaction Engineering. *Ind. Eng. Chem. Res.* **1999**, *38*, 4140.

(30)   Becker, A. R.; Sternson, L. A. General Catalyzed Condensation of Nitrosobenzene and Phenylhydroxylamine in Aqueous Solution. *J. Org. Chem.* **1980**, *45*, 1708.

(31)   Mann, C. A.; Lauer, B. E.; Hultin, C. T. Organic Inhibitors of Corrosion: Aromatic Amines. *Ind. Eng. Chem.* **1936**, *28*, 1048.

(32)   DeBerry, D. W. Modification of the Electrochemical and Corroision Behavior of Stainless Steels with an Electroactive Coating. *J. Electrochem. Soc.* **1985**, *132*, 1022.

(33)   Johnson, R. L.; Tratnyek, P. G.; Miehr, R.; Thoms, B. B.; Bandstra, J. Z. Reduction of Hydraulic Conductivity and Reactivity in Zero-Valent Iron Columns by Oxygen and TNT. *Ground Water Monitoring & Remediation* **2005**, in press.

(34)   Klausen, J.; Vikesland, P. J.; Kohn, T.; Burris, D. R.; Ball, W. P.; Roberts, A. L. Longevity of Granular Iron in Groundwater Treatment Processes: Solution

Composition Effects on Reduction of Organohalides and Nitroaromatic Compounds. *Environ. Sci. Technol.* **2003**, *37*, 1208.

(35)   Klausen, J.; Ranke, J.; Schwarzenbach, R. P. Influence of Solution Composition and Column Aging on the Reduction of Nitroaromatic Compounds by Zero-Valent Iron. *Chemosphere* **2001**, *44*, 511.
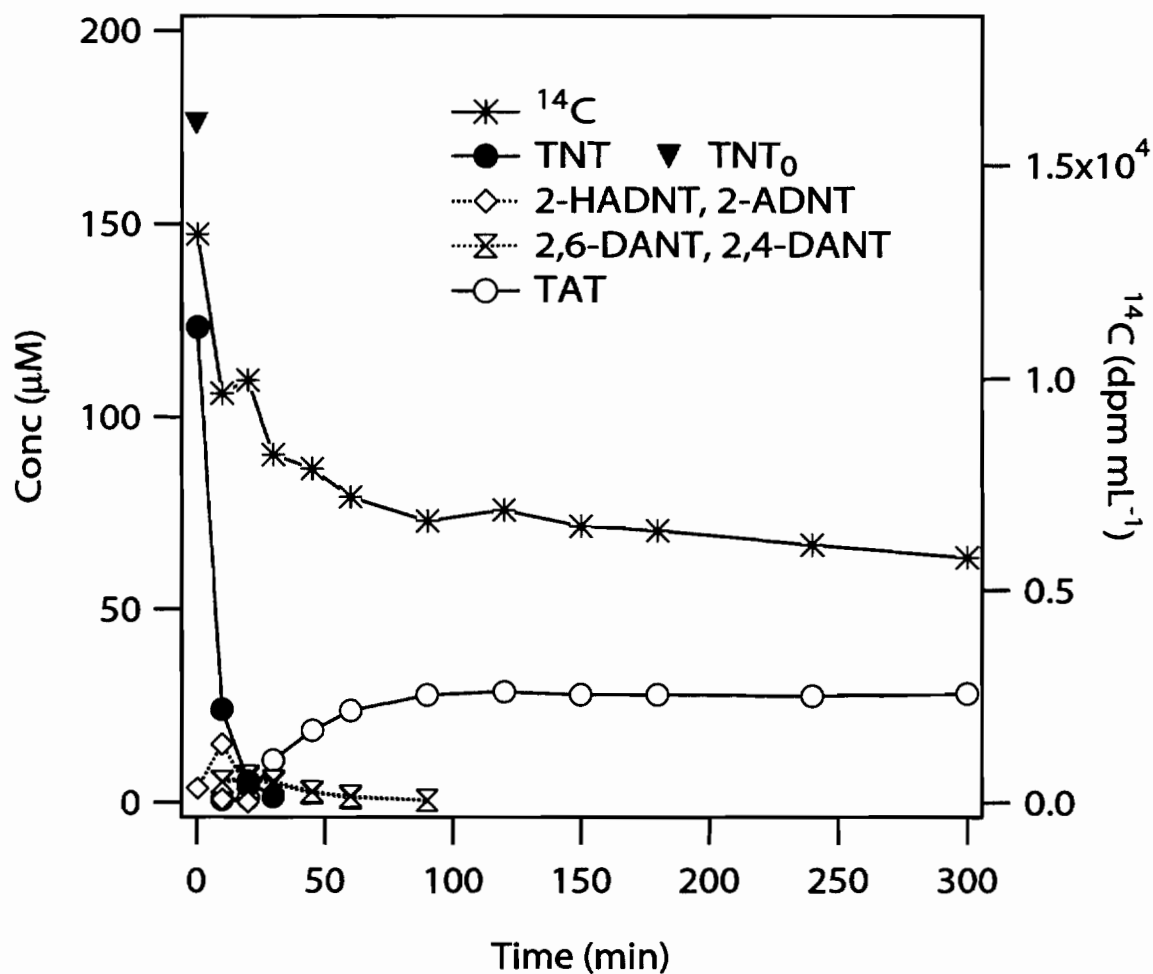
Figure 5.1.   TNT disappearance, transient 2-HADNT, 2-ADNT, 2,4-DANT, and 2,6-DANT, and TAT appearance in batch reactors with $TNT_0 = 176$ μM and $\rho_m = 50$ g L^{-1}. Data for radioactivity in solution from ^{14}C-labeled TNT are plotted on the right axis (scaled so that the calculated initial radioactivity corresponds to TNT_0.
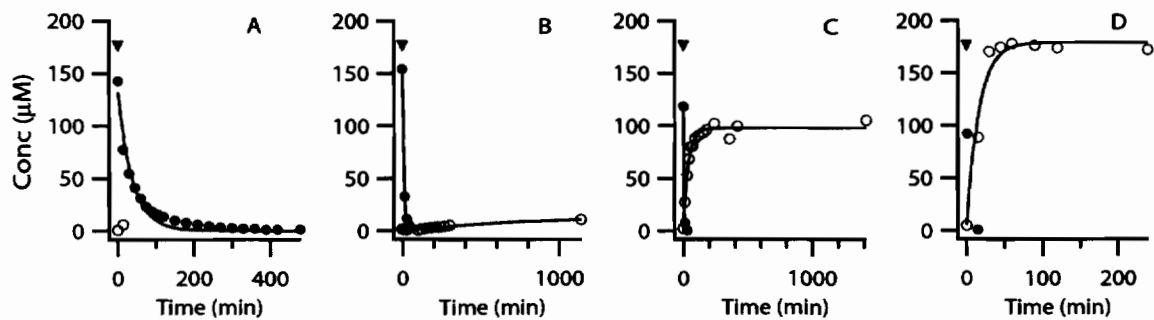
Figure 5.2.   TNT disappearance (closed circles) and TAT appearance (open circles) in batch reactors with $TNT_0 = 176 \, \mu M$ and $\rho_m =$ (A) 17 g L^{-1}, (B) 33 g L^{-1}, (C) 50 g L^{-1}, and (D) 100 g L^{-1}.
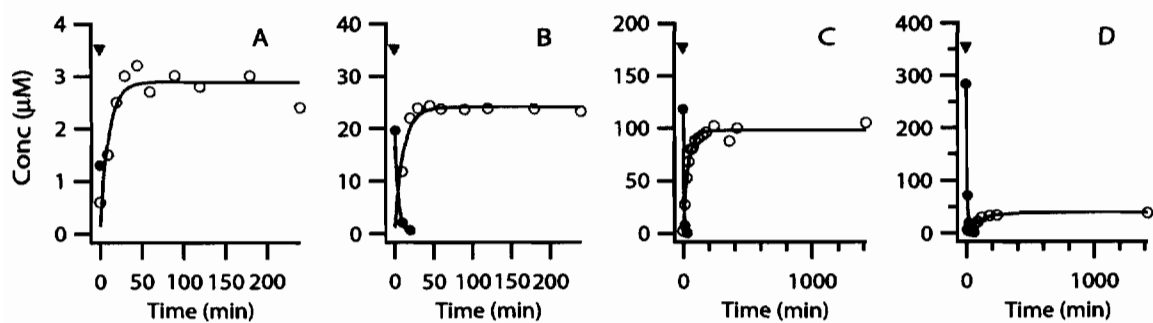
Figure 5.3. TNT disappearance (closed circles) and TAT appearance (open circles) in batch reactors with $\rho_m = 50$ g L^{-1} and (A) TNT$_0 = 3.5$ µM, (B) TNT$_0 = 35$ µM, (C) TNT$_0 = 176$ µM, and (D) TNT$_0 = 352$ µM.
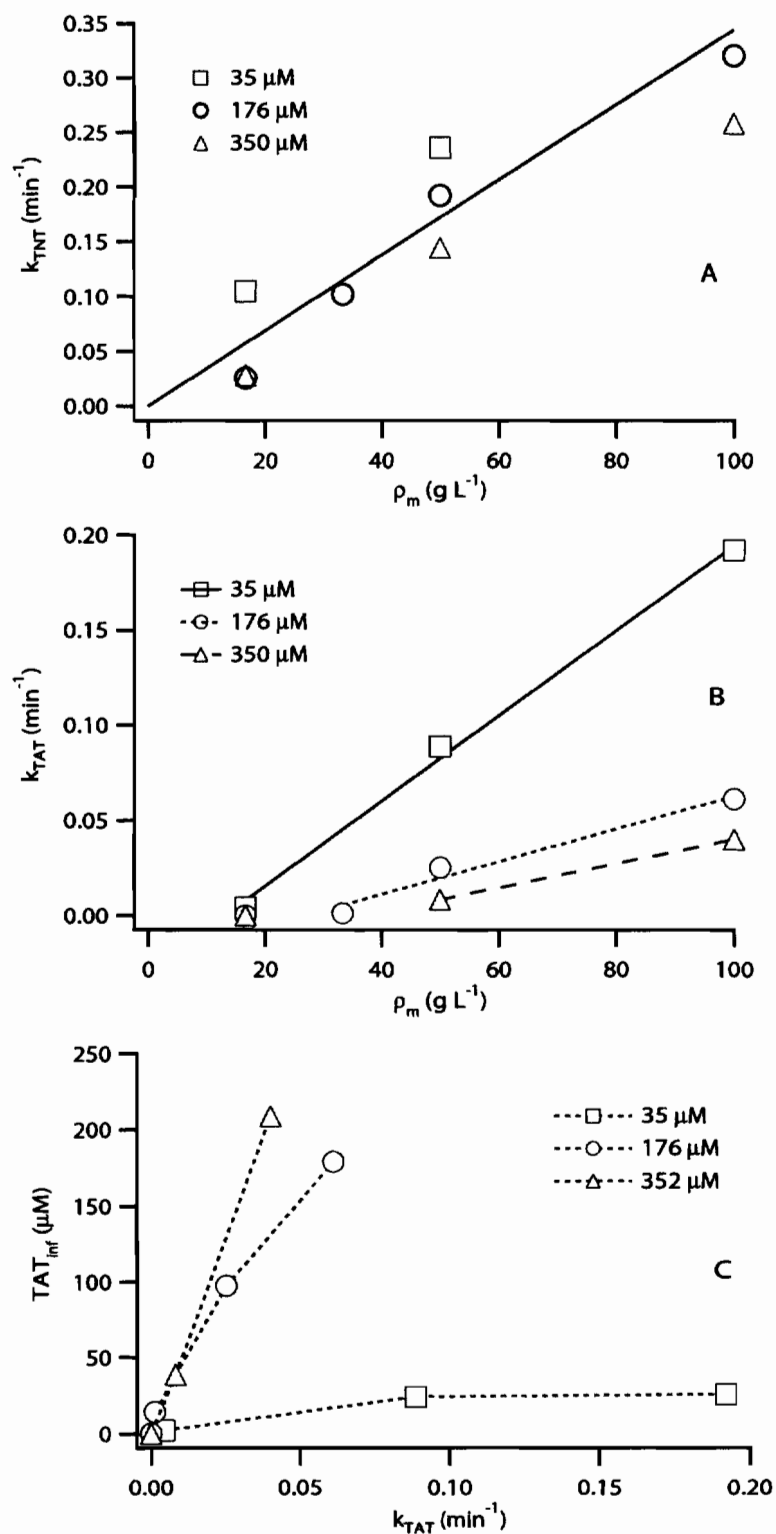
Figure 5.4.   Rate constants obtained from fitting (A) TNT disappearance curves and (B) TAT disappearance curves plotted against ρ_m. A table of the fitting results is included in Appendix A.
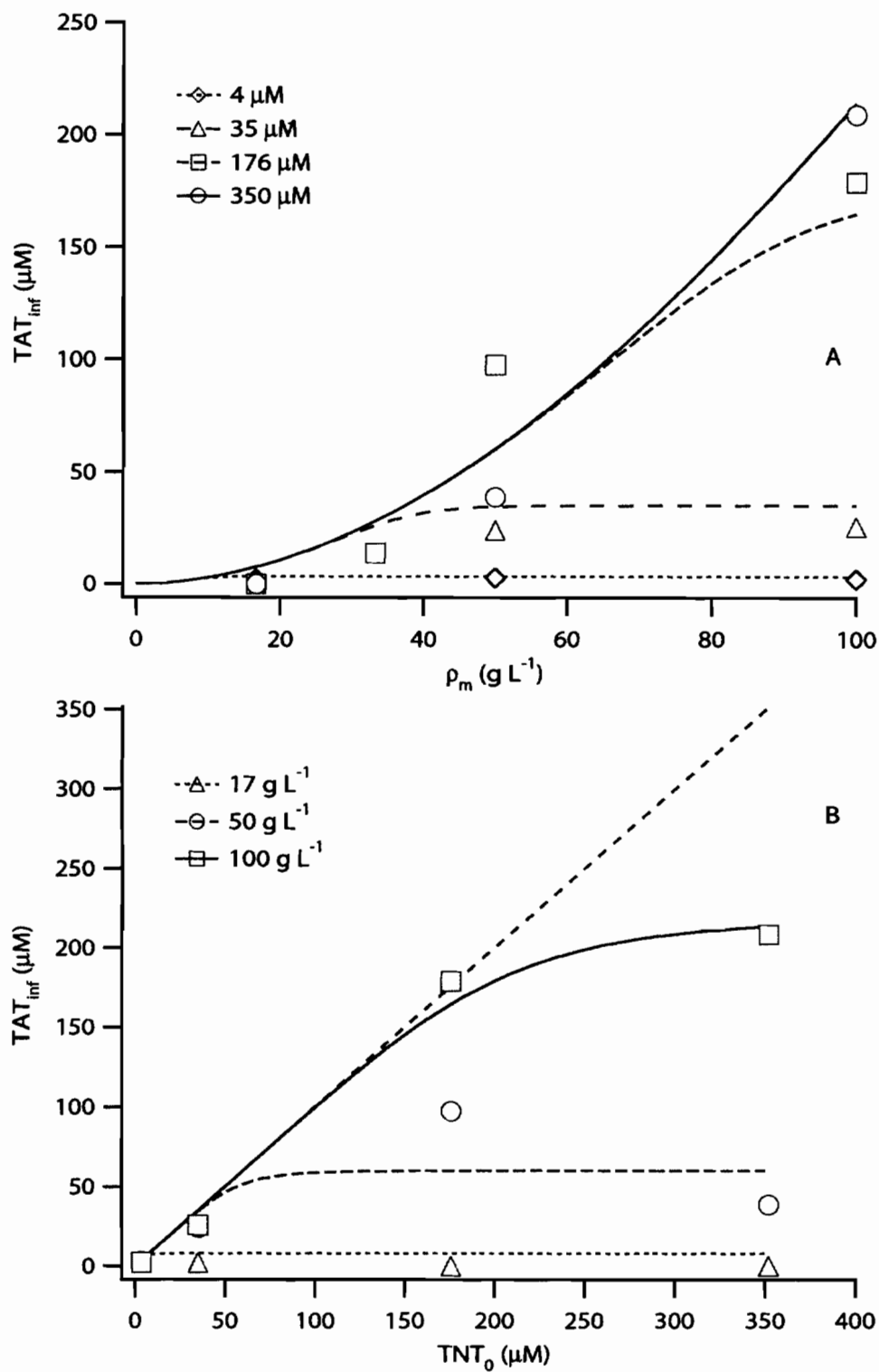
Figure 5.5. Fitted TAT_∞ plotted against (A) ρ_m and (B) TNT_0. The coarse dashed line in (B) represents complete conversion of TNT to TAT. Curves shown are the result of multi-variate fitting of equation 13 with $\kappa(\rho_m)$ given by equation 21.
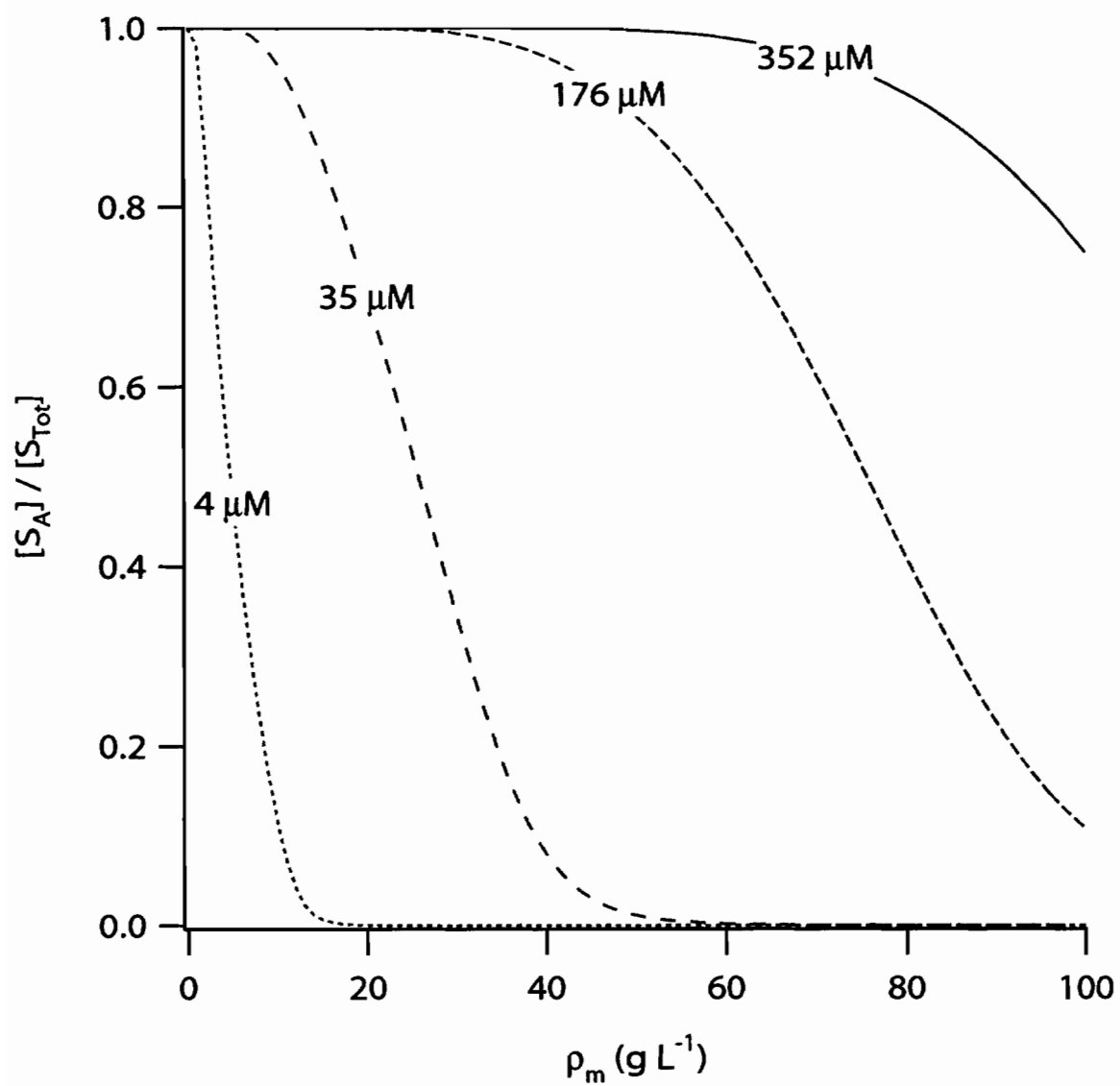
Figure 5.6.   Fraction of passivated surface based on scheme 3 plotted as a function of ρ_m for each of the values of TNT_0 used in this study.

CHAPTER 6

Conclusions

6.1 Summary

6.1.1 The Theory of Interfacial Chemical Kinetics

In Chapter 2 of this thesis rate laws that are commonly encountered in heterogeneous systems are derived from the advection-diffusion equation (for isotropic diffusion in a dilute solution) and reactive surface boundary conditions. Although this is not a new result (c.f., Rosner [1]), the derivations included in Chapter 2 are not typically found together and, too often, the isolated derivations contain conceptual errors (c.f. Venkatapathy et al. [2]). Considering the familiar rate laws together will help to eliminate these misunderstandings and the collection will serve as a useful reference for the researcher whose focus is the application of heterogeneous rate equations rather than the theory.

It is well documented that heterogeneous reactions may be rate limited by mass transfer, adsorption, or surface reaction. Equation (38) in Chapter 2 (reproduced here as equation 1) is the typical mathematical form of this statement.

$$k_{SA} = \cfrac{1}{\cfrac{k_{des}^{Ox}}{k_{ads}^{Ox}\Gamma_{Tot}k_{rxn}} + \cfrac{1}{k_{ads}^{Ox}\Gamma_{Tot}} + \cfrac{1}{k_{MT}^{Ox}}} \tag{1}$$

Equation (1), however, ignores the fact that, in a batch reactor, mass transfer and adsorption controlled reactions will not satisfy the pseudo-steady-state assumption used in deriving equation (1) until the reaction has run to completion. The analysis of bimodal kinetics in Chapter 2 (sec. 2.4.3) indicates that, for a batch reactor, mass transfer and adsorption controlled reactions will follow the large eigen-value given by equation (70)

in Chapter 2 while surface transformation controlled reactions will follow the small eigen-value. Figure 7 of Chapter 2 shows that the degree to which a reaction will follow the large or small eigen-value. It can, therefore, be expected that plotting k_{obs} vs. iron loading (ρ_m) will produce a transition from surface reaction control at low ρ_m to mass transfer/adsorption control at high ρ_m. Since such a transition would involve transition to a larger slope, this phenomenon may explain the negative intercepts sometimes found in determinations of k_{SA} by linear regression.

The Langmuir-Hinshelwood equation and the first-order rate law can be derived with either the pseudo-steady-state and the pseudo-equilibrium assumptions. The question, then, arises as to which assumption is the most general. The general consensus is that the pseudo-steady-state assumption is more general because of its rigorous application to flow through reactors (e.g., column reactors, continuously stirred tank reactors) and the fact that it can collapse to the pseudo-equilibrium assumption. The analysis in Chapter 2 (sec. 2.5), however, indicates that both of these assumptions are incorrect for batch reactors except in the case where they collapse (i.e., when rapid equilibrium is actually established). Figures 8 and 9 indicate that, even when the assumptions are incorrect, the form of the Langmuir-Hinshelwood equation and the first-order rate law are likely to be appropriate. This is consistent with the experimental success of these rate equations but also indicates that careful calculations need to be performed in order to scale between batch reactors and column reactors or FePRBs.

6.1.2 Central Limit Theorem for Chemical Kinetics in Complex Systems

In Chapter 3 it is conjectured that the preponderance of first-order kinetics—even in complicated media where the usual explanations are unlikely—can be understood as emerging from the complexity of the system in a manner that is analogous to the Central Limit Theorem. Numerical simulations of parallel reactions (that were constrained to behave as elementary steps) indicate that the combined effects of zero and second order processes yield a central tendency toward nearly first-order behavior. Roughly equal proportions of zero, first, and second-order processes are more likely with increasing number of parallel processes and, therefore, this central tendency is more likely to emerge in systems with many parts—one of the hallmarks of a complex system. In

addition to this, the central tendency is more likely when the rate constants for the parallel reactions yield a more equal distribution of material. This condition corresponds to greater pathway entropy which can be viewed as a proxy for the complexity of the reaction network.

6.1.3 Applicability of Single-Site Rate Equations for Reactions on Inhomogeneous Surfaces

The Langmuir-Hinshelwood equation is regularly applied to heterogeneous reactions [3] such as the reduction of solutes on iron metal [4]. In many cases, the implicit assumption of a homogeneous surface is unlikely to be satisfied and, so, the parameters found by fitting a Langmuir-Hinshelwood equation to experimental data likely represent an approximate average site. In Chapter 4 it is found that simple averaging of the sites on an inhomogeneous surface overestimates the rate of reaction, even in cases where some other single-site approximation is highly accurate. Application of a method for finding the best single-site approximation and the inversion of this method indicate that accurate single-site approximations are likely to exist over a broad range of inhomogeneity.

Although the best single-site approximation for an inhomogeneous surface is found to depend on the concentration range used to define the behavior of the reaction (e.g., the concentration range of a batch experiment). Equations (25-26) of Chapter 4 (reproduced here as equations 2-3) give general relationships for the relative nature of this dependence.

$$K_{ss}^{1-S}\big|_{\text{High Conc.}} < K_{ss}^{1-S}\big|_{\text{Low Conc.}} \tag{2}$$

$$k_{rxn}^{1-S}\big|_{\text{High Conc.}} > k_{rxn}^{1-S}\big|_{\text{Low Conc.}} \tag{3}$$

The inequalities of equations (2-3) indicate that ignoring inhomogeneity will cause reaction rates to be underestimated when a single-site approximation is extrapolated out of the concentration range used to parameterize the equation. This also offers the possibility of using kinetics experiments at different concentration ranges as a means of identifying inhomogeneous behavior.

6.1.4 Reduction of 2,4,6-Trinitrotoluene (TNT) by Iron Metal: Kinetic Controls on Product Distributions in Batch Experiments

In Chapter 5, a complicated relationship between TNT reduction product appearance and reaction conditions is identified in batch reactors loaded with granular iron metal. Specifically, TNT is completely converted to 2,4,6-triaminotoluene only at low initial TNT concentration, $[TNT]_0$, and/or high iron loading, ρ_m. Extraction experiments with ^{14}C-TNT indicate that the missing mass is on the surface, however, the response of TAT appearance to ρ_m is inconsistent with surface complexation of TAT. Mathematical analyses of generic reaction schemes that yield stable products in addition to TAT indicate that the observed behavior is consistent with coupling of the nitroso and hydroxylamino intermediates in the TNT reaction mechanism. These alternative products, when bound to the surface, can cause passivation of the iron surface. A numerical simulation of passivation due to the surface bound products in this system indicates that the relatively high $[TNT]_0$ and low ρ_m that are characteristic of laboratory experiments will tend to yield a greater degree of passivation than would be found in a field scale FePRB.

6.2 Synthesis

The conjecture, put forth in Chapter 3, that first-order kinetic expressions will be broadly applicable in environmental chemistry is generally supported by the rest of this thesis. Many of the kinetic regimes discussed in chapter 2 lead to first-order expressions; the first-order rate expression is employed over a wide range of conditions for the reduction of TNT by iron metal in chapter 5; and the Langmuir-Hinshelwood equation, discussed in chapters 2 and 4, reduces to a first-order expression at the low concentrations that are most environmentally relevant. This observation presents a general conclusion: that simple rate laws are likely to be sufficient for describing the data generated by most kinetics experiments. In some sense, this conclusion is encouraging because is precludes the need for complicated mathematics to commence with the study of chemical kinetics. However, this presents a problem with the practice of extrapolating reaction rates found in the laboratory to the, potentially quite different, conditions found

in the field. It also precludes the possibility of generating significant mechanistic information with a single kinetics experiment.

The latter difficulty can be overcome by performing suites of kinetic experiments with systematically varied inputs of reacting species. In chapter 5, for example, TAT_∞ observations undergo a stark bifurcation with respect to both [Fe] and $[TNT]_0$. Considering these bifurcations together yielded information about the reaction mechanism that will form a useful basis for investigations into the long-term performance of FePRBs for nitro-aromatic compounds. The results of chapter 4 indicate that, with no knowledge of the structure of the iron surface, the reactivity of multiple sites could be identified from two kinetics experiments performed at very different concentrations of oxidant. Sufficient mechanistic detail, thus determined, could alleviate the difficulty of scaling reaction rates between laboratory and field. In this light, the singular conclusion of this thesis can be stated: that kinetic modeling is among the best scientific tools for synthesizing information about chemical reactions generated across multiple scales; from molecular theory to laboratory experiment to the behavior of natural and engineered systems.

6.3 Literature Cited

(1)   Rosner, D. E. *Transport Processes in Chemically Reacting Flow Systems*; Butterworths: Boston, 1986.

(2)   Venkatapathy, R.; Bessingpas, D. G.; Canonica, S.; Perlinger, J. A. Kinetics Models for Trichloroethylene Transformation by Zero-Valent Iron. *Applied Catalysis, B: Environmental* **2002**, *37*, 139.

(3)   Hougen, O. A.; Watson, K. M. Solid Catalysts and Reaction Rates. *Industrial and Engineering Chemistry* **1943**, *35*, 529.

(4)   Wüst, W. F.; Köber, R.; Schlicker, O.; Dahmke, A. Combined Zero- and First-Order Kinetic Model of the Degradation of Tce and Cis-Dce with Commercial Iron. *Environ. Sci. Technol.* **1999**, *33*, 4304.

APPENDIX A

Summary of experimental results for "Reduction of 2,4,6-Trinitrotoluene (TNT) by Iron Metal: Kinetic Controls on Product Distributions in Batch Experiments"

Table A.1. SUMMARY OF EXPERIMENTAL RESULTS.

ρ_m (g L^{-1})	TNT$_0$ Nominal (μM)	k_{TNT} (min^{-1})	TNT$_0$ Best Fit (μM)	k_{TAT} (min^{-1})	TAT$_\infty$ Best Fit (μM)
17	3.5	--	--	0.082±0.08	2.07±0.064
50	3.5	--	--	0.095±0.02	2.9±0.1
100	3.5	--	--	0.46±1.5	2.2±0.1
17	35	0.11±0.004	27.2±0.5	0.0043±0.001	2.1±0.3
50	35	0.24±0.02	22.1±0.6	0.089±0.01	24.1±0.6
100	35	--	--	0.19±0.04	25.8±0.5
17	176	0.026±0.002	134±5.6	--	--
33	176	0.1±0.01	162±3.8	0.0012±0.0004	13.9±2.6
33	176*	0.13±0.004	160±2.3	0.0028±0.0003	13.6±0.7
50	176	0.19±0.002	130±0.3	0.025±0.002	97.5±1.8
50	176*	0.17±0.004	134±1.1	0.02±0.004	29.2±1.6
100	176*	0.32±0.02	140±1.1	0.08±0.01	142±3.0
100	176	--	--	0.061±0.01	179±6.4
17	352	0.028±0.002	279±12	--	--
50	352	0.14±0.002	308±2.0	0.0083±0.001	38.8±2.6
100	352	0.26±0.001	327±0.4	0.04±0.009	209±12

*Performed with ^{14}C-labeled TNT.

APPENDIX B

Derivations and Proofs for "Reduction of 2,4,6-Trinitrotoluene (TNT) by Iron Metal: Kinetic Controls on Product Distributions in Batch Experiments"

Derivation of eq 10 for branching model with $m_{TAT} = m_{UNK}$. Dividing eq 8 by eq 9 gives

$$\frac{d[TAT]}{dt} = \frac{k_{TAT}(\rho_m)}{k_{UNK}(\rho_m)} \frac{d[UNK]}{dt} \equiv \kappa(\rho_m) \frac{d[UNK]}{dt} \tag{S1}$$

integrating with respect to t gives

$$[TAT] - [TAT]_{t=0} = \kappa(\rho_m)([UNK] - [UNK]_{t=0}) \tag{S2}$$

The initial TAT and UNK concentrations are zero and taking the limit as $t \rightarrow \infty$ gives

$$TAT_\infty = \kappa(\rho_m) \, UNK_\infty \tag{S3}$$

Applying the mass balance equation $TNT_0 = TAT_\infty + UNK_\infty$ and rearranging gives eq 10.

$$TAT_\infty = TNT_0 \frac{\kappa(\rho_m)}{1 + \kappa(\rho_m)} \tag{10}$$

Properties of κ with respect to ρ_m for the branching scenario. Taking the derivative of eq 10 with respect to ρ_m gives

$$\frac{\partial TAT_\infty}{\partial \rho_m} = \frac{TNT_0}{(1+\kappa)^2} \frac{\partial \kappa}{\partial \rho_m} \tag{S4}$$

Since $TNT_0 / (1+\kappa)^2 > 0$, application of eq 3 gives

$$\frac{\partial \kappa}{\partial \rho_m} \geq 0 \tag{S5}$$

The second derivative of eq 10 with respect to ρ_m is

$$\frac{\partial^2 TAT_\infty}{\partial \rho_m^2} = -\frac{2 \, TNT_0}{(1+\kappa)^3} \frac{\partial \kappa}{\partial \rho_m} + \frac{TNT_0}{(1+\kappa)^2} \frac{\partial^2 \kappa}{\partial \rho_m^2} \tag{S6}$$

To give a positive slope, k must be finite for $0 < \rho_m \leq \rho_{crit}$, where ρ_{crit} is the inflection point in TAT_∞. Therefore, application of eq 4 gives

$$\frac{\partial^2 \kappa}{\partial \rho_m^2} > \frac{2}{1+\kappa} \frac{\partial \kappa}{\partial \rho_m} \tag{S7}$$

The right hand side of eq S7 is positive and, therefore, we have

$$\frac{\partial^2 \kappa}{\partial \rho_{Fe}^2} > 0 \tag{S8}$$

for $0 < \rho_m \leq \rho_{crit}$.

Derivation of eq 13 for the branching scenario. Integration of eq 8 with respect to t (with $[TAT]_0 = 0$) gives

$$\int_0^t \frac{d[TAT]}{dt} dt = [TAT] = \int_0^t k_{TAT}(\rho_m) \, [INT]^{m_{TAT}} dt \tag{S9}$$

Substitution of eq 11 gives

$$[TAT] = \int_{[INT]_0}^{[INT]_t} -\frac{k_{TAT}[INT]^{m_{TAT}}}{k_{UNK}[INT]^{m_{UNK}} + k_{TAT}[INT]^{m_{TAT}}} d[INT] \tag{S10}$$

Since $[INT]_0 = TNT_0$ and $[INT]_\infty = 0$, taking the limit of eq S10 as $t \rightarrow \infty$ and substituting $w = [INT]$, $\Delta m = m_{UNK} - m_{TAT}$ and $\kappa = k_{TAT}/k_{UNK}$ gives eq 13

$$TAT_\infty = \int_0^{TNT_0} \frac{\kappa(\rho_m)}{\kappa(\rho_m) + w^{\Delta m}} dw \tag{13}$$

Properties of κ with respect to TNT_0 for the branching scenario. The derivative of eq 13 with respect to TNT_0 is

$$\frac{\partial TAT_\infty}{\partial TNT_0} = \frac{\kappa}{\kappa + TNT_0^{\Delta m}} \tag{S11}$$

Since κ is positive, eq S11 satisfies eq 5. The second derivative of eq 13 is

$$\frac{\partial^2 TAT_\infty}{\partial TNT_0^2} = \frac{\kappa^3 (\Delta m) TNT_0^{\Delta m - 1}}{\left(\kappa + TNT_0^{\Delta m}\right)^2} \tag{S12}$$

Eq S12 satisfies eq 6 if and only if $\Delta m \geq 0$.

Derivation of eq 18 for coupling. For $m_{UNK} = m_{TAT}$, dividing eq 16 by eq 15 and rearranging terms gives

$$\frac{v_{UNK}k_{UNK}(\rho_m)\,[TAT]^{n_{TAT}}}{k_{TAT}(\rho_m)-v_{TAT}k_{UNK}(\rho_m)\,[TAT]^{n_{TAT}}}\frac{d[TAT]}{dt}=\frac{d[UNK]}{dt} \tag{S13}$$

Integrating eq S13 with respect to t and substituting $w = [TAT]$ on the left hand side gives

$$\int_{[TAT]_0}^{[TAT]_t}\frac{v_{UNK}w^{n_{TAT}}}{\kappa(\rho_m)-v_{TAT}w^{n_{TAT}}}dw=[UNK]_t-[UNK]_0 \tag{S14}$$

Applying eq 17 for mass balance, the initial conditions $[TAT]_0 = [UNK]_0 = 0$, and taking the limit as $t \to \infty$ gives eq 18

$$\frac{TNT_0-TAT_\infty}{v_{INT}+v_{TAT}}=\int_0^{TAT_\infty}\frac{w^{n_{TAT}}}{\kappa(\rho_m)-v_{TAT}w^{n_{TAT}}}dw \tag{18}$$

The left hand side of eq 18 is linear in TAT_∞ with negative slope, $-1/(v_{INT}+v_{TAT})$, and positive intercept, $TNT_0/(v_{INT}+v_{TAT})$. The right hand side goes through the origin and has a singularity at $TAT_\infty = (\kappa/v_{TAT})^{(1/n_{TAT})}$ with positive slope for $TAT_\infty < (\kappa/v_{TAT})^{(1/n_{TAT})}$ and negative slope for $TAT_\infty > (\kappa/v_{TAT})^{(1/n_{TAT})}$ such that the left hand side of eq 18 approaches $-\infty$ as TAT_∞ approaches ∞. Since $0 < TAT_\infty < TNT_0$ the only roots of eq 18 that are physically realistic are those where

$$TAT_\infty \le \left(\frac{\kappa}{v_{TAT}}\right)^{(1/n_{TAT})} \tag{S15}$$

The equality in eq S15 applies in the limit as $TNT_0 \to \infty$.

Properties of κ with respect to ρ_m for the coupling scenario. Taking the derivative of eq 18 with respect to ρ_m gives

$$-\frac{1}{v_{INT}-v_{UNK}}\frac{\partial TAT_\infty}{\partial \rho_m}=\frac{\partial}{\partial \rho_m}\int_0^{TAT_\infty}\frac{w^{n_{TAT}}}{\kappa(\rho_m)-v_{TAT}w^{n_{TAT}}}dw \tag{S16}$$

The derivative on the right hand side of eq S16 can be evaluated using Leibinitz's rule for the derivative of an integral.

$$\frac{\partial}{\partial \rho_m} \int_0^{TAT_\infty} \frac{w^{n_{TAT}}}{\kappa - v_{TAT} w^{n_{TAT}}} dw = \frac{\partial \kappa}{\partial \rho_m} \int_0^{TAT_\infty} -\frac{w^{n_{TAT}}}{\left(\kappa - v_{TAT} w^{n_{TAT}}\right)^2} dw$$

$$+ \frac{TAT_\infty^{n_{TAT}}}{\kappa - v_{TAT} TAT_\infty^{n_{TAT}}} \frac{\partial TAT_\infty}{\partial \rho_m} \qquad (S17)$$

Rearranging eq S17 gives

$$\frac{\partial TAT_\infty}{\partial \rho_m} = \frac{\dfrac{\partial \kappa}{\partial \rho_m} \displaystyle\int_0^{TAT_\infty} \dfrac{w^{n_{TAT}}}{\left(\kappa - v_{TAT} w^{n_{TAT}}\right)^2} dw}{\dfrac{1}{v_{INT} + v_{TAT}} + \dfrac{TAT_\infty^{n_{TAT}}}{\kappa - v_{TAT} TAT_\infty^{n_{TAT}}}} \qquad (S18)$$

Since, by eq S15, $\kappa > v_{TAT} TAT_\infty^{n_{TAT}}$, $\partial TAT_\infty / \partial \rho_m > 0$ if and only if $\partial \kappa / \partial \rho_m > 0$.

The integral on the right hand side of eq S18 can be evaluated by parts with $u = w$ and $dv = w^{-n_{TAT}-1} / (\kappa w^{-n_{TAT}} - v_{TAT})^2$ giving

$$\int_0^{TAT_\infty} \frac{w^{-n_{TAT}-1} w}{\left(\kappa w^{-n_{TAT}} - v_{TAT}\right)^2} dw = \frac{TAT_\infty^{n_{TAT}+1}}{n_{TAT} \kappa \left(\kappa - v_{TAT} TAT_\infty^{n_{TAT}}\right)} - \frac{1}{n_{TAT} \kappa} \int_0^{TAT_\infty} \frac{w^{n_{TAT}}}{\kappa - v_{TAT} w^{n_{TAT}}} dw \quad (S19)$$

The integral on the right hand side of eq S19 is given by eq 18 and rearrangement gives

$$\frac{\partial TAT_\infty}{\partial \rho_m} = \frac{1}{n_{TAT} \kappa} \frac{\partial \kappa}{\partial \rho_m} \left(\kappa - v_{TAT} TAT_\infty^{n_{TAT}}\right) \left(\frac{TAT_\infty}{\kappa - v_{TAT} TAT_\infty^{n_{TAT}}} - \frac{TNT_0}{\kappa + v_{INT} TAT_\infty^{n_{TAT}}}\right) \qquad (S20)$$

The second derivative of eq 18 with respect to ρ_m can be found from eq S20 giving

$$\frac{\partial^2 TAT_\infty}{\partial \rho_m^2} = \left(\frac{1 - n_{TAT}}{n_{TAT}^2 \kappa^2}(TAT_\infty - \alpha) - \frac{TNT_0^2 (v_{INT} + v_{TAT}) TAT_\infty^{n_{TAT}} \alpha}{\left(\kappa + v_{INT} TAT_\infty^{n_{TAT}}\right)^2}\right) \left(\frac{\partial \kappa}{\partial \rho_m}\right)^2$$

$$+ \frac{1}{n_{TAT} \kappa}(TAT_\infty - \alpha) \frac{\partial^2 \kappa}{\partial \rho_m^2} \qquad (S21)$$

where α is given by

$$\alpha = TNT_0 \frac{\kappa - v_{TAT} TAT_\infty^{n_{TAT}}}{\kappa + v_{INT} TAT_\infty^{n_{TAT}}} \qquad (S22)$$

By eq S15, $0 \leq \alpha \leq TNT_0$. $\alpha = TNT_0$ applies as $TNT_0 \to 0$ and $TAT_\infty \to TNT_0$ and, therefore, $\alpha \leq TAT_\infty$. For $n_{TAT} \geq 1$, eq S21 can satisfy eq 4 if and only if $\partial^2 \kappa / \partial \rho_{Fe}^2 \geq 0$ over the range $0 < \rho_m \leq \rho_{crit}$. For $n_{TAT} = 0$

$$\frac{\partial^2 TAT_\infty}{\partial \rho_m^2} = TNT_0 \left(\nu_{INT} + \nu_{TAT} \right) \left(-\frac{2}{\left(\kappa + \nu_{INT} \right)^3} \left(\frac{\partial \kappa}{\partial \rho_m} \right)^2 + \frac{1}{\left(\kappa + \nu_{INT} \right)^2} \frac{\partial^2 \kappa}{\partial \rho_m^2} \right) \tag{S23}$$

Eq S22 can satisfy eq 4 if and only if $\partial^2 \kappa / \partial \rho_m^2 \geq 0$ over the range $0 < \rho_m \leq \rho_{crit}$ and we reason (inductively) that κ should also behave in this fashion for $0 < n_{TAT} < 1$.

Properties of κ with respect to TAT_∞ for the coupling scenario. The derivative of eq 18 with respect to TNT_0 can be evaluated using Leibinitz's rule giving

$$\frac{\partial TAT_\infty}{\partial TNT_0} = \frac{\kappa - \nu_{TAT} TAT_\infty^{n_{TAT}}}{\kappa + \nu_{INT} TAT_\infty^{n_{TAT}}} \tag{S24}$$

Eq S24 is positive for all TNT_0 thus satisfying eq 5 and it approaches 0 as $TNT_0 \to \infty$. The second derivative of eq 18 is

$$\frac{\partial^2 TAT_\infty}{\partial TNT_0^2} = \frac{-\kappa n_{TAT} TAT_\infty^{n_{TAT}-1} \left(\nu_{INT} + \nu_{TAT} \right)}{\left(\kappa + \nu_{INT} TAT_\infty^{n_{TAT}} \right)^2} \frac{\partial TAT_\infty}{\partial TNT_0} \tag{S25}$$

Eq S25 is negative for all TNT_0 and, therefore, eq 18 satisfies eq 6.

Derivation of eq 18 for partitioning. Eq 19 can be derived by assuming that m_{UNK} moles of TAT react in reversible fashion to form m_{TAT} moles of UNK with equilibrium constant κ^{-1} such that

$$\frac{1}{\kappa(\rho_m)} = \frac{UNK_\infty^{m_{TAT}}}{TAT_\infty^{m_{UNK}}} \tag{S26}$$

The stoichiometry for the TNT $\to$ TAT reaction is 1:1 and, therefore, a mass balance expression can be written as

$$m_{TAT} TNT_0 = m_{TAT} TAT_\infty + m_{UNK} UNK_\infty \tag{S27}$$

Substituting eq S27 into eq S26 gives eq 19.

$$\frac{1}{\kappa(\rho_m)} = \frac{\left(\dfrac{m_{TAT}}{m_{UNK}}\right)^{m_{TAT}} (TNT_0 - TAT_\infty)^{m_{TAT}}}{TAT_\infty{}^{m_{UNK}}} \tag{19}$$

Properties of κ with respect to ρ_m for the partitioning scenario. Taking the derivative of eq 19 with respect to ρ_m gives

$$\frac{\partial TAT_\infty}{\partial \rho_m} = \left(\frac{m_{UNK}}{TAT_\infty} + \frac{m_{TAT}}{(TNT_0 - TAT_\infty)}\right)^{-1} \frac{1}{\kappa}\frac{\partial \kappa}{\partial \rho_m} \tag{S28}$$

Equation S28 satisfies eq 3 if and only if $\partial \kappa / \partial \rho_m \geq 0$. The second derivative can be found from eq S28.

$$\frac{\partial^2 TAT_\infty}{\partial \rho_m{}^2} = \left(\frac{m_{UNK}}{TAT_\infty} + \frac{m_{TAT}}{(TNT_0 - TAT_\infty)}\right)^{-1} \left(\left(\frac{\dfrac{m_{UNK}}{TAT_\infty{}^2} - \dfrac{m_{TAT}}{(TNT_0 - TAT_\infty)^2}}{\left(\dfrac{m_{UNK}}{TAT_\infty} + \dfrac{m_{TAT}}{(TNT_0 - TAT_\infty)}\right)^2} - 1\right)\left(\frac{1}{\kappa}\frac{\partial \kappa}{\partial \rho_m}\right)^2 + \frac{1}{\kappa}\frac{\partial^2 \kappa}{\partial \rho_m{}^2}\right) \tag{S29}$$

Equation S29 satisfies eq 4 if and only if $\partial^2 \kappa / \partial \rho_m{}^2 \geq 0$.

Properties of κ with respect to TAT_∞ for the partitioning scenario. Taking the derivative of eq 19 with respect to TNT_0 gives

$$\frac{\partial TAT_\infty}{\partial TNT_0} = \frac{\dfrac{m_{TAT}}{TNT_0 - TAT_\infty}}{\dfrac{m_{UNK}}{TAT_\infty} + \dfrac{m_{TAT}}{TNT_0 - TAT_\infty}} \tag{S30}$$

Equation S30 is positive for all m_{TAT} and $m_{UNK} > 0$ and, therefore, the partitioning model satisfies eq 5. The second derivative is

$$\frac{\partial^2 TAT_\infty}{\partial TNT_0{}^2} = \frac{m_{UNK}(m_{TAT} - m_{UNK})(TNT_0 - TAT_\infty)}{\left(m_{UNK}TNT_0 + (m_{TAT} - m_{UNK})TAT_\infty\right)^2} \frac{\partial TAT_\infty}{\partial TNT_0} \tag{S31}$$

Equation S31 satisfies eq 6 if and only if $m_{TAT} \leq m_{UNK}$.

Derivation of eq 23 for surface passivation. Assuming that the rates of the reactions in scheme 3 are first-order with respect to both UNK and surface site concentrations gives

$$\frac{d[S_A]}{dt} = -\frac{d[S_P]}{dt} = -k_A[S_A][UNK] \tag{S32}$$

$$\frac{d[UNK]}{dt} = -(k_A[S_A] + k_P[S_P])[UNK] \tag{S33}$$

Dividing eq S32 by eq S33 and applying $[S_{Tot}] = [S_A] + [S_P]$ gives

$$\frac{d[S_A]}{d[UNK]} = \frac{k_A[S_A]}{(k_A - k_P)[S_A] + k_P[S_{Tot}]} \tag{S34}$$

If the reactions in scheme 3 are fast, then the reaction rapidly proceeds to completion and the active site population can be found by integrating eq S34 from $[UNK]_0$ to 0.

$$[UNK] = TNT_0 - TAT_\infty = ([S_{Tot}] - [S_A])\left(1 - \frac{k_P}{k_A}\right) + \frac{k_P}{k_A}[S_{Tot}]\ln\left(\frac{[S_A]}{[S_{Tot}]}\right) \tag{S35}$$

If both reactions in scheme 3 occur with equal probability, $k_A = k_P$ and solving eq S35 with $[S_{Tot}] = \rho_m / \alpha$ gives eq 23.

$$\frac{[S_P]}{[S_{Tot}]} = 1 - \exp\left(\alpha \frac{TNT_0 - TAT_\infty}{\rho_m}\right) \tag{23}$$

BIOGRAPHICAL SKETCH

Joel was born on September 20, 1976 in Monroeville, PA. He attended Clarkson University, in Postdam, NY, where he took a Bachelor's degree from the department of Civil Engineering. He is 6'3" with blue eyes and brown hair. He enjoys new adventures, long walks on the beach, and romantic candle light dinners. He is looking for that special someone to share his life with; a free spirit who will make his heart sing. If you are the one, send him a biographical sketch. Be sure to mention any honors and awards and to include a publication list. Joel's publications include:

Bandstra, J. Z.; Tratnyek, P. G. Central Limit Theorem for Chemical Kinetics in Complex Systems. *J. Math. Chem.* In press.

Bandstra, J. Z.; Miehr, R.; Johnson, R. L.; Tratnyek, P. G. Remediation of 2,4,6-Trinitrotoluene (TNT) by Iron Metal: Kinetic Controls on Product Distributions in Batch and Column Experiments. *Environ. Sci. Technol.* **2005**, *39*, 230.

Johnson, R. L.; Tratnyek, P. G.; Miehr, R.; Thoms R. B.; and Bandstra J. Z. Reduction of Hydraulic Conductivity and Reactivity in Zero-Valent Iron Columns by Oxygen and TNT. *Ground Water Monitoring & Remediation.* In press.

Nurmi, J. T.; Bandstra, J. Z.; Tratnyek, P. G. Packed Powder Electrodes for Characterizing the Reactivity of Granular Iron in Borate Solutions. *J. Electrochem. Soc.* **2004**, *151*, B347.

Bandstra, J. Z.; Tratnyek, P. G. Applicability of Single-Site Rate Equations for Reactions on Inhomogeneous Surfaces. *Ind. Eng. Chem. Res.* **2004**, *43*, 1615.

Miehr, R.; Tratnyek, P. G.; Bandstra, J. Z.; Scherer, M. M.; Alowitz, M.; Bylaska, E. J. The Diversity of Contaminant Reduction Reactions by Zero-Valent Iron: Role of the Reductate. *Environ. Sci. Technol.* **2004**, *38*, 139.

Agrawal, A.; Ferguson, W. J.; Gardner, B. O.; Christ, J. A.; Bandstra, J. Z.; Tratnyek, P. G. Effects of Carbonate Species on the Kinetics of 1,1,1-Trichloroethane by Zero-Valent Iron. *Environ. Sci. Technol.* **2002**, *36*, 4326.